

Ionic and electronic behaviors of earth-abundant semiconductor materials and their applications toward solar energy harvesting

Author: Matthew T. Mayer

Persistent link: <http://hdl.handle.net/2345/3034>

This work is posted on [eScholarship@BC](#),
Boston College University Libraries.

Boston College Electronic Thesis or Dissertation, 2013

Copyright is held by the author, with all rights reserved, unless otherwise noted.

Boston College

The Graduate School of Arts and Sciences

Department of Chemistry

IONIC AND ELECTRONIC BEHAVIORS OF EARTH-ABUNDANT
SEMICONDUCTOR MATERIALS AND THEIR APPLICATIONS
TOWARD SOLAR ENERGY HARVESTING

a dissertation

by

MATTHEW T. MAYER

submitted in partial fulfillment of the requirements

for the degree of

Doctor of Philosophy

May 2013

© copyright by MATTHEW THOMAS MAYER

2013

Title:

Ionic and electronic behaviors of earth-abundant semiconductor materials and their applications toward solar energy harvesting

Author: Matthew T. Mayer

Advisor: Prof. Dunwei Wang

Abstract

Semiconductor devices offer promise for efficient conversion of sunlight into other useful forms of energy, in either photovoltaic or photoelectrochemical cell configurations to produce electrical power or chemical energy, respectively. This dissertation examines ionic and electronic phenomena in some candidate semiconductors and seeks to understand their implications toward solar energy conversion applications. First, copper sulfide (Cu_2S) was examined as a candidate photovoltaic material. It was discovered that its unique property of cation diffusion allows the room-temperature synthesis of vertically-aligned nanowire arrays, a morphology which facilitates study of the diffusion processes. This diffusivity was found to induce hysteresis in the electronic behavior, leading to the phenomena of resistive switching and negative differential resistance. The Cu_2S were then demonstrated as morphological templates for solid-state conversion into different types of heterostructures, including segmented and rod-in-tube morphologies. Near-complete conversion to ZnS , enabled by the out-diffusion of Cu back into the substrate, was also achieved. While the ion diffusion property likely hinders the reliability of Cu_2S in photovoltaic applications, it was shown to enable useful electronic and ionic behaviors.

Secondly, iron oxide (Fe_2O_3 , hematite) was examined as a photoanode for photoelectrochemical water splitting. Its energetic limitations toward the water electrolysis reactions were addressed using two approaches aimed at achieving greater photovoltages and

thereby improved water splitting efficiencies. In the first, a built-in n-p junction produced an internal field to drive charge separation and generate photovoltage. In the second, Fe₂O₃ was deposited onto a smaller band gap material, silicon, to form a device capable of producing enhanced total photovoltage by a dual-absorber Z-scheme mechanism. Both approaches resulted in a cathodic shift of the photocurrent onset potential, signifying enhanced power output and progress toward the unassisted photoelectrolysis of water.

Table of Contents

| | | |
|-----------|--|----|
| Chapter 1 | Introduction: solar energy harvesting by semiconductors | 1 |
| 1.1 | Solar energy and natural photosynthesis | 2 |
| 1.2 | Semiconductors | 6 |
| 1.3 | Photovoltaic vs. photoelectrochemical solar energy harvesting | 9 |
| 1.4 | Our approach: synthetic and morphological control | 10 |
| 1.5 | References | 11 |
| Chapter 2 | Cu ₂ S: ionic behavior of a potential photovoltaic material | 12 |
| 2.1 | Cu ₂ S nanowire arrays: new morphology for an old material..... | 12 |
| 2.2 | References | 25 |
| Chapter 3 | Ionic behavior revealed by electronic phenomena on Cu ₂ S/ZnO..... | 27 |
| 3.1 | References | 34 |
| Chapter 4 | Ionic diffusion driven solid-state conversions of Cu ₂ S nanowires..... | 36 |
| 4.1 | Fe–Cu ₂ S System | 38 |
| 4.2 | Zn–Cu ₂ S System..... | 48 |
| 4.3 | Materials Considerations | 55 |
| 4.4 | Outlook for Cu ₂ S-based photovoltaics | 56 |
| 4.5 | References | 56 |
| Chapter 5 | Photoelectrochemical water splitting..... | 60 |
| 5.1 | Hematite Fe ₂ O ₃ as a promising candidate material | 68 |

| | | |
|-----------|---|----|
| 5.2 | Atomic layer deposition of Fe ₂ O ₃ thin films | 70 |
| 5.3 | Improved photocurrents from Fe ₂ O ₃ on nanostructure scaffolds | 71 |
| 5.4 | References | 72 |
| Chapter 6 | Creating n–p homojunction Fe ₂ O ₃ for additional photovoltage | 75 |
| 6.1 | References | 82 |
| Chapter 7 | The Si/Fe ₂ O ₃ dual-absorber photoanode | 84 |
| 7.1 | References | 96 |
| Chapter 8 | Outlook for PEC water splitting | 98 |

Abbreviations

| | |
|-------|---|
| ALD | atomic layer deposition |
| AM | air mass |
| CB | conduction band |
| CVD | chemical vapor deposition |
| ED | electron diffraction |
| EDS | energy-dispersive X-ray spectroscopy |
| E_F | Fermi level |
| EIS | electrochemical impedance spectroscopy |
| eV | electron volt |
| FTO | F-doped SnO_2 |
| IPCE | incident photon-to-electron conversion efficiency |
| IR | infrared |
| I-V | current-voltage |
| J-V | current density-voltage |
| NDR | negative differential resistance |
| NHE | normal hydrogen electrode (fixed potential) |
| NW | nanowire |
| PEC | photoelectrochemical |
| PV | photovoltaic |
| RHE | reversible hydrogen electrode (pH-adjusted potential) |
| RIT | rod-in-tube |
| RS | resistive switching |
| SEM | scanning electron microscopy |
| TEM | transmission electron microscopy |
| UV | ultraviolet |
| VB | valence band |
| XRD | X-ray diffraction |

Acknowledgements

Any success I have had in graduate school is due largely because of the guidance received from my advisor Prof. Dunwei Wang. I entered the program at BC with no clear idea what type of research I wanted to do. Dunwei invited me to work in his lab during the summer, and I never looked back. Over the last five years, he has shown me by example how to be a great scientist and leader. While always being full of unique and forward-thinking ideas, Dunwei nevertheless emphasized the importance of keeping in mind the big picture of what we were working on. We were never satisfied to publish incremental works, but rather took the extra effort to make sure the research we reported was impactful. I was lucky to find him as an advisor, and I truly thank him for his guidance.

Thanks to my dissertation readers and defense committee for your efforts. I've had the pleasure to work with all of you whether in teaching or research, and I admire your contagious passion for science.

Thanks to all my Wang Lab colleagues over the years, with special thanks to those with whom I've worked directly. To Xiaohua, Zach, Yongjing, Sa, Yang, Chun, Henry, Pengcheng, and Xiaogang, it was an honor and a pleasure to work with you. To all past and present members, I'm happy to have had been a part of such a hard-working yet enjoyable group.

To Dezhi Wang, Steve Shepard, and Greg McMahon, I thank you for your support in the various facilities. My work would not have been possible without the microscopes and clean room, including the experts who run them.

Thanks to Ian, Donna, John, and Jen for keeping Merkert running and keeping us safe from ourselves. Special thanks to the Merkert staff, including Terri, Dale, Ginny, Steve, and Lori.

Best regards to all my BC chemistry colleagues, especially my dear friends Chris, Zach, and Grace. Thanks for being there to commiserate and laugh with me.

Thanks to my family, who never once questioned my somewhat random decision to move from Idaho to Boston for grad school, and for their persistent support as I continue further eastward to Switzerland. Please come visit, and I promise someday I will move back to the west!

I owe my deepest thanks to my dear love Heather. You suffered through this adventure with me, almost certainly working harder than me as a teacher and nanny. I love you and look forward to our continued adventures!

Chapter 1

Introduction: solar energy harvesting by semiconductors

“The photochemical processes, that hitherto have been the guarded secret of the plants, will have been mastered by human industry, which will know how to make them bear even more abundant fruit than nature, for nature is not in a hurry but mankind is.”

Giacomo Ciamician, “The Photochemistry of the Future”¹

Mankind is indeed in a hurry to develop sources of alternative energy, for despite periods of extreme growth in the global energy demand, most of that energy still derives from exhaustible, non-renewable resources. Aside from the important questions about how fossil fuel usage contributes to harmful climate change and other negative environmental impacts,² we do know for certain that its supply is finite. In fact, it is widely believed that we are nearing, or have already reached, the tipping point for oil production.³ Whether for environmental, political, or economic purposes, increased efforts need to be made to develop clean and renewable sources of energy.

As Ciamician recognized,¹ fossil energy is indeed a form of solar energy, for its biomass precursors all drew their energy from the sun. The problem, however, is the fact that while Earth’s coal and oil reserves took millions of years to accumulate and store energy, releasing that energy rapidly over the course of just a few hundred years can be expected to have severe consequences on the atmospheric temperature around Earth. From a kinetic perspective, it would make more sense to utilize an energy source in which the heat input more closely matches the heat output, so as to avoid disrupting the terrestrial climate humans have come to adapt to. The obvious choice of energy source is light from the Sun, inspired by Nature itself.

Essentially all of life on Earth is supported, directly or indirectly, by light-to-energy conversion reactions, largely through the process of photosynthesis. A simplified description of the process is as follows: light energy from the sun is used to drive reactions involving water and carbon dioxide, generating molecular oxygen as well as energetic carbon-containing molecules (carbohydrates). These molecules drive the processes of life and support the food chain from the bottom to the top. However, despite the ubiquitous nature of natural photosynthesis, and despite the fact that the process has evolved over billions of years, overall efficiencies of less than 1% are common under typical conditions.⁴ This efficiency is defined as the total chemical energy gained by the molecular photosynthetic products divided by the total energy of solar photons incident on a photosynthetic surface. To make solar energy harvesting a viable approach toward supporting our energy demands, we should learn from photosynthesis but also seek to improve the light-to-energy efficiencies of the process.

The following sections will briefly outline the characteristics of the terrestrial solar spectrum, introduce promising semiconductor-based methods of converting sunlight into useable energy, and describe the characteristics of semiconducting materials which make them suitable for those applications.

1.1 Solar energy and natural photosynthesis

The sun behaves like a blackbody emitter of a characteristic temperature of 5800 K, meaning it produces a broad spectrum from high- (X-ray) to low- (infrared) energy photons. The strongest emission falls in the spectral range visible to the human eye, with wavelengths ranging between 380–780 nm. The spectrum of light reaching Earth's surface, as shown in Figure 1.1, features absorption bands caused by atmospheric CO₂, H₂O, O₂, O₃, and other vapors and aerosols. The air mass 1.5 global standard (AM 1.5G) as defined by ASTM represents an average incident irradiation at temperate latitudes and is used as a standard spectrum for testing and comparison of

solar harvesting devices. The integrated overall power density of this spectral standard is defined as 100 mW/cm^2 .

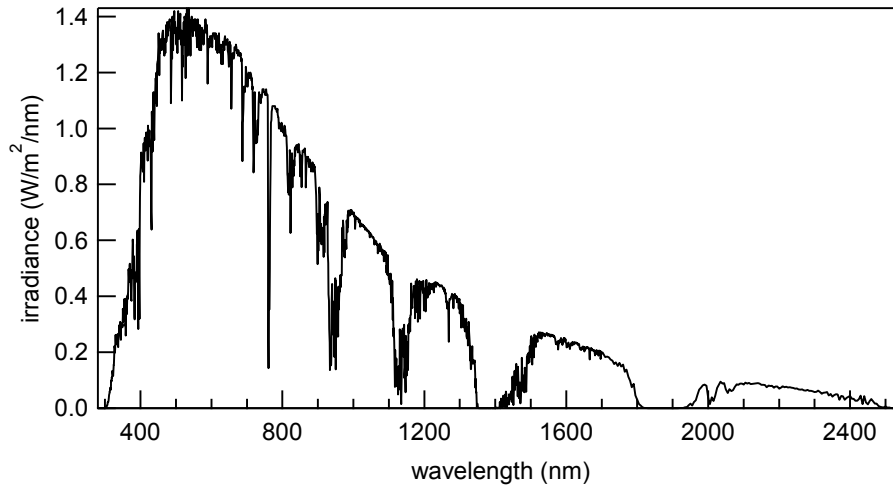


Figure 1.1 ASTM Reference AM 1.5G Solar Spectrum G173-03, National Renewable Energy Laboratory.

In a broader scope, it has been estimated that the average power of sunlight striking the sun-facing surface of Earth is around 100,000 TW, whereas global human energy consumption is approaching 14 TW.⁴ Numerically, this means that sun provides Earth enough power in one hour to meet humankind's energy demands for one year. Furthermore, the sun can be considered a renewable and inexhaustible energy source (at least, on the time scale of human existence), and the utilization of its energy can ideally take place without climate-changing emissions.

Of course, the utilization of sunlight has several limitations, foremost being the diurnal and diffuse nature of the energy supply. Combining these factors with seasonal effects, varying weather patterns (cloud coverage), and regional differences in solar irradiance, we see that there are many challenges to satisfying our constant and global energy demands using sunlight alone. These challenges can be tackled by improvements in solar-to-energy conversion efficiencies, but we must also consider that for solar energy to make a significant impact, the scale of solar

harvesting will have to be massive. This presents a further challenge since existing commercial photovoltaic solar cells (solar to electric energy), despite achieving respectable conversion efficiencies of around 18%, are made from high grade single- or poly-crystalline silicon by energetically demanding and expensive processes. Higher-performance cells (approaching the theoretical limits of 32% at 1-sun, single absorber, or 66% for multiple-junction cells)⁵ require sophisticated synthetic processes and typically rely on rare and/or toxic materials. To achieve widespread use of solar energy harvesting on a global scale, the materials and processes will need to be cost-effective enough to compete with other energy sources, and abundant enough to be scaled up massively. Our goal is therefore to achieve higher energy-conversion efficiencies using cheap, abundant, and nontoxic materials.

Conversion of solar energy into different energetic forms including electronic and chemical energy (but excluding solar thermal, which relies on different principles) relies on a collection of simultaneous processes to be carried out with minimal losses. In a simplified form, these processes are i) light absorption to generate charge carriers, ii) charge separation to force charges in the desired directions to generate electronic current, and iii) charge transport/transfer to the energy output form (either electronic current or chemical reactions, see Section 1.3). Natural photosynthesis carries out these processes by using a combination of many different components in series. As depicted in Figure 1.2, light absorption takes place in the pigment molecules within photosystems I and II, generating excited complexes capable of delivering electrons to the electron transport chains. These chains of redox reactions separate the excited electrons from the ground states of the photosystems, thereby decreasing the probability of recombination (loss of excited energy) and ensuring high quantum efficiencies of charge collection. In the case of natural photosynthesis the charges are transported to catalytic sites where redox reactions

generate the desired energetic molecules NADPH and ATP (not shown), along with the oxidation of water to molecular oxygen.

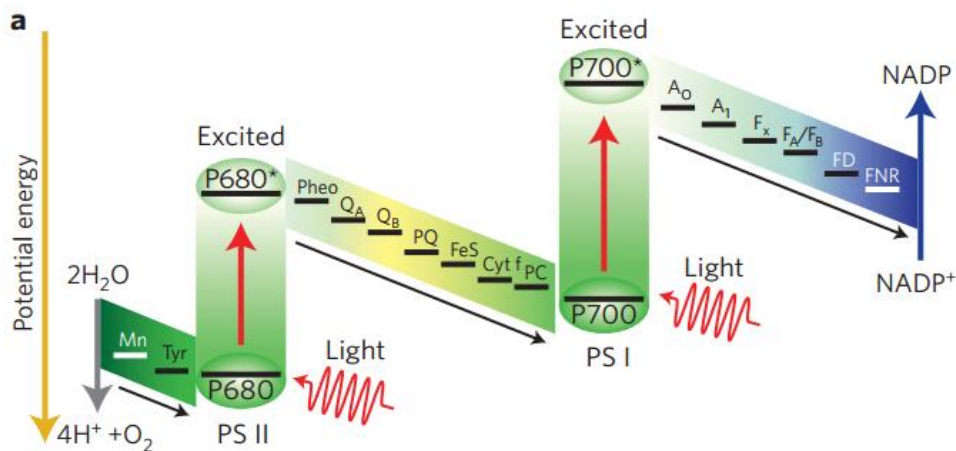


Figure 1.2 Energy scheme of natural photosynthesis. Adapted with permission from ref. 6

As we can see from this complex (but still hugely over-simplified) schematic, natural photosynthesis is actually the combination of many sequential processes occurring on numerous distinct components. This is the general method which nature has evolved for the conversion of sunlight energy into usable forms, but it is by no means optimal, especially when high power output is desired. As stated previously, the typical efficiencies of natural photosynthesis are too low to satisfy our demands.⁴ Nevertheless, examination of its mechanism allows us to identify the key processes which we aim to reproduce and improve in our efforts to capture energy from sunlight.

A wide variety of approaches have been pursued towards creating artificial systems to harvest solar energy.^{4,6-9} In our work, our efforts have been focused on a promising class of solid inorganic materials, semiconductors.

1.2 Semiconductors

A collection of simultaneous processes must occur for sunlight energy to be converted into other useful forms, namely electronic or chemical energy. Semiconductors offer promise as materials for sunlight harvesting because, when properly designed, they are capable of carrying out most (or all) of the key processes introduced in the previous section (light absorption, charge separation, and charge transport/transfer). The essential feature of semiconductors which gives rise to these charge behaviors, as implied by the name semiconductor, is the property of “selective conductivity”. Depending on the conditions, a semiconductor can exhibit charge conducting behaviors ranging from insulator to conductor, and this property is directly related to the ability to absorb light energy and to support internal electric fields necessary for charge collection. The details of these processes as they relate to photoactive semiconductors will be introduced in this chapter and continued in the discussion of photoelectrochemical water splitting in Chapter 5. A greater depth of discussion can be found in the literature.^{5,7,10}

These unique charge conduction behaviors arise from the fact that semiconductors exhibit energy bands in their electronic structure. Differing from metallic conductors, wherein a continuum of states ensure a conductive path for charges, and from insulators, where no states are accessible to provide charge mobility, semiconductors have a valence band of filled electronic states at lower potential energy and a conduction band of empty (at absolute zero temperature) states at higher energies, separated by a gap devoid of states. This energy difference between the band edges, called the semiconductor “band gap”, is a key parameter that determines a material’s suitability for sunlight harvesting. Materials with finite band gaps up to about 4.0 eV (eV = electron volt = 1.602×10^{-19} J) are considered semiconductors; materials with very small or nonexistent band gaps are conductors and those with larger band gaps are insulators. The mechanism by which semiconductors exhibit photoactivity in response to sunlight illumination is

called the photovoltaic effect, wherein a photon with the wavelength λ carrying the energy E can transfer its energy to an electron to raise the electron potential energy by that same amount, following the relationship for photon energy,

$$E = hc/\lambda$$

where E is energy, h is the Planck constant, c is the speed of light, and λ is the photon wavelength. The process of photon absorption is defined as this transfer of energy from a photon to an electron, causing the promotion of an electron from the semiconductor valence band to the conduction band. It is the band gap energy which defines which photons can be absorbed by a semiconductor. Since the gap between energy bands is devoid of states, an electron excitation can only take place in response to a photon with an energy equal to or greater than that of the band gap. The band gap therefore represents a minimum energy needed for photon absorption.

Using this concept to relate photon energies to wavelengths, we solve the above relation for an expression relating wavelength and energy in units of nanometers and electron volts, respectively, finding

$$E \text{ (eV)} = 1240 / \lambda \text{ (nm)}$$

Therefore, a relatively high-energy green photon at $\lambda = 550 \text{ nm}$ (near the peak flux of solar photons, see Figure 1.1) can be absorbed by semiconductors with band gaps of 2.25 eV or smaller, whereas a lower-energy red photon at $\lambda = 1000 \text{ nm}$ can only be absorbed by narrow band gaps of 1.24 eV or smaller. This consideration becomes important when choosing a material (or combination of materials) to achieve the best utilization of the solar spectrum to yield the desired power output.

To illustrate how the semiconductor band gap affects its solar conversion efficiency, it is important to understand what defines the power output of a light-absorbing semiconductor. By definition, electric power is the product of current and voltage. The electronic current induced by light absorption is directly related to the rate of electron photoexcitation and thus is a function of the photon flux. The voltage, on the other hand, arises from the electronic potential difference induced by the photovoltaic effect and is limited by the material's band gap. In a device comprising a single semiconductor light absorber, the choice of optimal band gap therefore depends on a balance between photocurrent and photovoltage. A large band gap material such as TiO_2 (~ 3.1 eV) can produce a sizeable photovoltage, but with an absorption edge at ~ 400 nm it can only absorb a small fraction of the solar flux ($\lambda < 400$ nm) and will therefore produce only small photocurrents under solar illumination. On the other hand, a smaller band gap material like Si (~ 1.1 eV) can absorb across much more of the spectrum (up to ~ 1130 nm) to yield larger currents, but its photovoltage is limited by the smallness of the band gap. In both cases, the overall power produced (the product of photocurrent and photovoltage) will be limited. This perspective allows us to recognize the guiding principle in how the band gap affects the power output of a sunlight-absorbing semiconductor.

When combining the important factors, including the sunlight spectral distribution and the photovoltage dependence on band gap, the theoretical limits of efficiency can be determined. Shockley and Queisser calculated the detailed balance limit for a single p-n junction solar cell, which identified a maximum solar conversion efficiency of around 33% achievable on a 1.4 eV band gap material.⁵ The efficiency is defined as the ratio between the maximum electric power output and the power input (here determined for the AM 1.5 spectrum at 100 mW/cm^2). This theoretical work identifies the band gap range of 1.0–1.6 eV as near optimal when seeking the maximum power output. This discussion has been largely simplified here, but it is of fundamental

importance when selecting suitable candidate materials for photovoltaic materials. This will be further discussed regarding our choice of Cu_2S in the following chapter. However, the Shockley–Queisser limit is not the only criterion for selecting a material. In some cases, such as photoelectrochemical reactions, the photovoltage requirement is more demanding and thus larger band gap materials may be needed (see Chapter 5). Furthermore, multiple-absorber tandem devices can offer larger theoretical efficiencies (see Chapter 6 for a related approach). The general differences between two light-harvesting methods are discussed in the following section.

1.3 Photovoltaic vs. photoelectrochemical solar energy harvesting

Two of the general approaches to sunlight harvesting are the use of photovoltaic and photoelectrochemical systems. Traditional solar cells, including most of what is presently commercially utilized, fall into the photovoltaic (PV) category. PV cells in their most basic and typical form comprise a junction of two semiconductor materials of different conductivity types to form a solid p–n junction.⁵ Simply put, the junction produces an internal electric field which drives the separation of charges and creates an output of electrical power. Solar cells operating in this manner can therefore supply electronic power to an electric grid for distribution, can be used to directly drive machines, or can be transferred to storage systems (e.g. batteries). A shortcoming of PV systems is the difficulty of efficiently storing and transporting the harvested energy. Public electricity grid-connected systems suffer from power losses at long ranges and do not directly offer an energy storage solution for nighttime use. Batteries also suffer from inefficiencies and have insufficient energy densities (i.e. they are too heavy) to solve the need for long distance transport of stored energy.

An alternative to the output of direct electric power is to instead use the photogenerated charges to synthesize desirable chemical fuels, thereby storing the harvested photon energies in chemical bonds. In these photoelectrochemical (PEC) systems, a semiconductor electrode is put

into direct contact with a liquid electrolyte and charges are transferred across the semiconductor/liquid junction to drive the reduction–oxidation (redox) reactions of interest. Advantages of PEC approaches include the fact that the chemical fuels produced are typically in liquid or gaseous forms which can be stored and transported with little energy loss, by methods resembling our present handling of fossil fuels like gasoline and natural gas, and thus may prove more reliable and adoptable than PV-derived electricity. Other advantages include the ability to make fuels that are cleaner to utilize than conventional combustion of fossil fuels, namely molecular H_2 that can be obtained by electrolysis of H_2O , which will be discussed in more depth in Chapter 5. Limitations of PEC include the difficulty of finding materials that are stable under the reducing or oxidizing conditions present during operation, the energetically demanding nature and complexity of the desired chemical reactions, the avoidance of side-reactions, and the challenge of engineering a standalone fuel-producing device, among others.

Both PV and PEC approaches undoubtedly have important roles in meeting our future energy needs, and deserve ongoing research. Our studies of synthesizing and examining Cu_2S as a PV material are discussed in Chapter 2, followed by our efforts to use Fe_2O_3 as an electrode for semiconductor PEC water splitting in Chapter 5. In both cases, our work was driven by our ideas and capabilities of controlling the composition and morphology of semiconductor materials at the nanometer scale with the goal of improving their performance.

1.4 Our approach: synthetic and morphological control

To tackle some of the fundamental limitations inherent in the materials of interest, we have sought to develop new approaches of semiconductor synthesis and to design rational combinations of materials. The enabling factor has been our ability to synthesize materials with great control of their morphologies (e.g. thin films, nanowires) and compositions (e.g. controlled doping, high-quality material interfaces). In each case, the theme of our research has been to use

these principles to improve behaviors of materials as compared to their bulk counterparts. For instance, it has been theorized and demonstrated that vertically-aligned nanowire array morphologies can result in enhanced light absorption and charge separation toward improved efficiencies over bulk material.¹¹⁻¹² While this was the goal of the synthetic approach introduced in Chapter 2, we also found the morphology to be a useful tool for detailed study of ion-diffusion processes in the electronic behavior of Cu₂S (Chapter 3) and in solid-state conversion reactions (Chapter 4). A second example is the controlled growth of high-quality thin films, which we demonstrate using the atomic layer deposition technique. This was shown to allow precise control over semiconductor doping (Chapter 6) while also providing the capability of conformal deposition on high surface area nanostructures (Chapter 7). These approaches are detailed in the chapters that follow.

1.5 References

- 1 Ciamician, G. The Photochemistry of the Future. *Science* **1912**, *36*, 385-394.
- 2 Vitousek, P. M. Beyond Global Warming: Ecology and Global Change. *Ecology* **1994**, *75*, 1862-1876.
- 3 Murray, J.; King, D. Climate policy: Oil's tipping point has passed. *Nature* **2012**, *481*, 433-435.
- 4 Barber, J. Photosynthetic energy conversion: natural and artificial. *Chem. Soc. Rev.* **2009**, *38*, 185-196.
- 5 Shockley, W.; Queisser, H. J. Detailed Balance Limit of Efficiency of P-N Junction Solar Cells. *J. Appl. Phys.* **1961**, *32*, 510-520.
- 6 Tachibana, Y.; Vayssieres, L.; Durrant, J. R. Artificial photosynthesis for solar water-splitting. *Nat. Photon.* **2012**, *6*, 511-518.
- 7 Walter, M. G.; Warren, E. L.; McKone, J. R.; Boettcher, S. W.; Mi, Q.; Santori, E. A.; Lewis, N. S. Solar water splitting cells. *Chem. Rev.* **2010**, *110*, 6446-6473.
- 8 Grätzel, M. Dye-sensitized solar cells. *J. Photoch. Photobio. C* **2003**, *4*, 145-153.
- 9 Shah, A.; Torres, P.; Tscharnner, R.; Wyrsh, N.; Keppner, H. Photovoltaic technology: The case for thin-film solar cells. *Science* **1999**, *285*, 692-698.
- 10 Rothwarf, A.; Böer, K. W. Direct conversion of solar energy through photovoltaic cells. *Prog. Sol. St. Chem.* **1975**, *10*, Part 2, 71-102.
- 11 Law, M.; Greene, L. E.; Johnson, J. C.; Saykally, R.; Yang, P. D. Nanowire dye-sensitized solar cells. *Nat. Mater.* **2005**, *4*, 455-459.
- 12 Law, M.; Goldberger, J.; Yang, P. D. Semiconductor nanowires and nanotubes. *Ann. Rev. Mat. Res.* **2004**, *34*, 83-122.

Chapter 2

Cu₂S: ionic behavior of a potential photovoltaic material

Chapters 2–4 detail our findings upon pursuing Cu₂S nanowires as a photovoltaic material. We chose to study Cu₂S because of its promising properties as a light-absorbing semiconductor and we were inspired by recent works which showed possible advantages of using nanoscale morphologies to improve solar cell materials. Our studies led us to a variety of interesting discoveries about the material. Although we did not succeed in producing a high-efficiency solar cell device, several important phenomena relating to the ionic behaviors of Cu₂S were revealed. Section 2.1 details the study of the unique mechanism of vertically-aligned nanowire array growth.¹ In Chapter 3 we examine the anomalous electronic behaviors of heterojunction devices attributable to ion diffusion.² Lastly, Chapter 4 presents our findings regarding solid-state conversion reactions of Cu₂S nanowires into unique new materials.³

2.1 Cu₂S nanowire arrays: new morphology for an old material

This section is adapted from: Liu, X.; Mayer, M. T.; Wang, D. Understanding ionic vacancy diffusion growth of cuprous sulfide nanowires. *Angew. Chem. Int. Ed.* **2010**, *49*, 3165-3168.

In the 1970's and 1980's there was much interest in copper (II) sulfide (Cu₂S) as an absorber material for photovoltaic applications. It was determined to have an indirect band gap of approximately 1.2 eV, making it within the range desired for optimal solar-to-electric power efficiencies. Theoretical studies have predicted a practical power conversion efficiency of 17.8 % on Cu₂S/ZnO-based solar cells,⁴ and efficiencies exceeding 9 % have been experimentally demonstrated on devices formed from Cu₂S and CdS thin films.⁵⁻⁶ However, the unusually high copper mobility within the close-packed sulfur sublattice seemed to contribute to stability problems, as mobile copper was found to diffuse across the p–n junction formed by interfacing

Cu₂S with CdS, causing rapid performance degradation.⁶⁻⁷ As a result, research on Cu₂S-based devices slowed for several decades.⁸

In recent years, with the development of various Cu₂S nanostructure syntheses, a renewed interest in this material for solar energy conversion has developed.⁹⁻¹³ Among the reported morphologies, nanowires (NWs) are of particular interest because the anisotropic nature of NWs offers an optimal combination of light absorption and charge separation, beyond that achievable with planar bulk materials.¹⁴⁻¹⁷ In particular, the synthesis of Cu₂S NW arrays on a copper substrate developed by Yang et al. has attracted considerable attention.¹⁰ An oxide-assisted nucleation and growth model was originally proposed to account for the unique growth of Cu₂S. Although Yang et al. did allude to an alternative mechanism that would involve ionic vacancy diffusion,¹⁸ a detailed understanding remained lacking.

We were attracted to the possibility of using such Cu₂S NW arrays in PV devices, given the possibility that such morphologies could yield enhanced efficiencies for solar energy conversion. We believed that the demonstration of significant performance enhancement could renew interest in the material one thought to be unsuitable for solar cells. The big question was what effect, if any, the nanostructure morphology would have on the known diffusivity of Cu in the material.

We first sought to replicate the synthesis of Cu₂S NW arrays. It quickly became apparent that the growth mechanism itself was highly intriguing and worth detailed study. Importantly, despite the fact that O₂ acts as a necessary reactant, no copper oxide was observed in the product, which suggests that O₂ plays a different role from what had been reported previously. By focusing on how ionic vacancies are annihilated in the supporting substrate that also serves as the copper supply source, we uncovered the ionic diffusion nature of the Cu₂S growth. The results highlight the importance of controlling ionic behaviors in the synthesis. Because the success of

Cu₂S-based solar cells relies on the ability to understand and control copper diffusion in Cu₂S, this work could also shed light on how to achieve high practical energy conversion efficiencies using Cu₂S.

Nanowire arrays of Cu₂S were grown by a vapor-solid reaction between Cu metal and H₂S gas. The general procedure included anodic electropolishing of the Cu to yield a clean and mirror-smooth surface, followed by subjecting the Cu to a constant flow of H₂S, O₂, and H₂O vapor.¹ The critical role of H₂O had not been previously recognized. Furthermore, although we sought to vary the gaseous precursor parameters, such as flow rate ratios, our study focused on how these variations influence the ionic vacancy generation, diffusion, and annihilation. This approach contrasted the existing reports in which attention was concentrated on how the various parameters influence the gas-phase feeding whilst the role of copper supply remained unexplored.

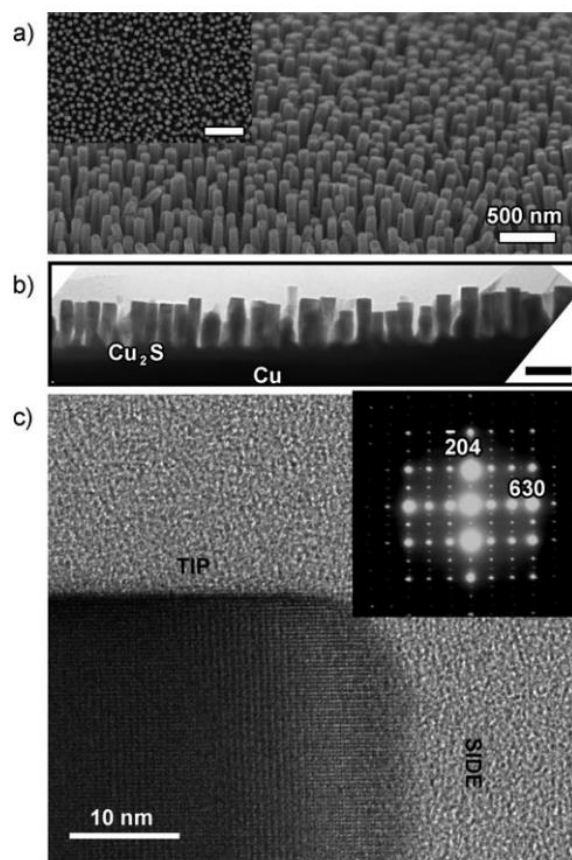


Figure 2.1 Electron micrographs of Cu_2S NWs. a) The uniformity of the vertically-aligned nanowire arrays can be seen by perspective and top-view (inset) SEM images. b) Cross-sectional TEM. c) High-resolution TEM shows the atomically smooth surfaces of a single NW (inset: electron diffraction pattern corresponding to the chalcocite Cu_2S phase). Reprinted with permission from ref. 1, © 2010 Wiley-VCH.

Typical scanning electron micrographs (SEM) of the as-grown Cu_2S NWs are shown in Figure 2.1. Uniform Cu_2S NWs with diameters of about 100 nm and lengths about 500 nm were produced by a 3 h exposure to the gas mixture flow. Cross-sectional transmission electron microscopy (TEM) examinations revealed that the NW tips and sides are free of impurity particles (such as seeds or catalysts) and are nearly atomically smooth, thus ruling out the possibility of a seeded-catalyzed growth.¹⁰ The NW array is separated from the copper substrate by an underlying Cu_2S layer of approximately 250 nm thickness, the importance of which in understanding the detailed growth mechanism will be discussed below. Both electron diffraction

(Figure 2.1c, inset) and X-ray diffraction (Figure 2.2) patterns confirmed that the as-grown Cu_2S is of the low chalcocite structure. Optical characterizations showed that the product has an indirect band gap of 1.20 eV (Figure 2.3), which is in good agreement with the literature.^{12,19}

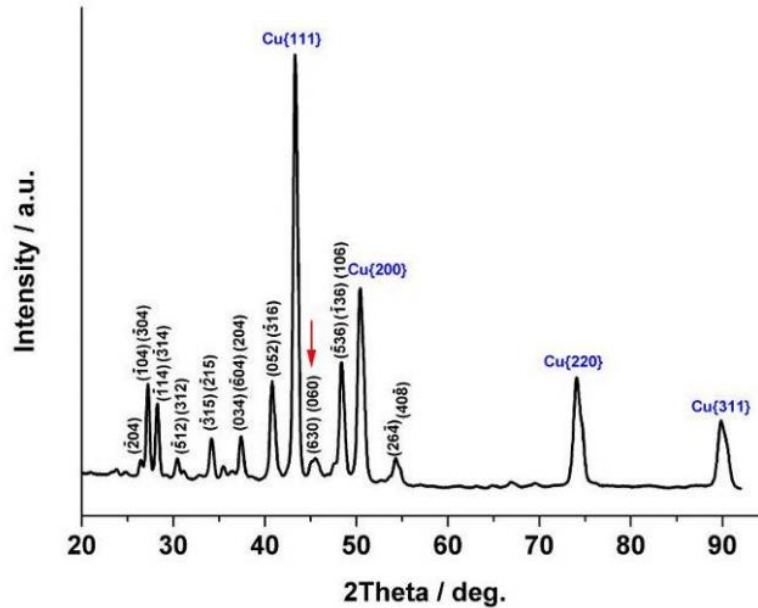


Figure 2.2 XRD pattern of a Cu_2S NW array grown on Cu foil. Black labels indicate diffraction peaks indexed to the low chalcocite structure of Cu_2S . The blue indices are those attributable to the Cu substrate. Reprinted with permission from ref. 1, © 2010 Wiley-VCH.

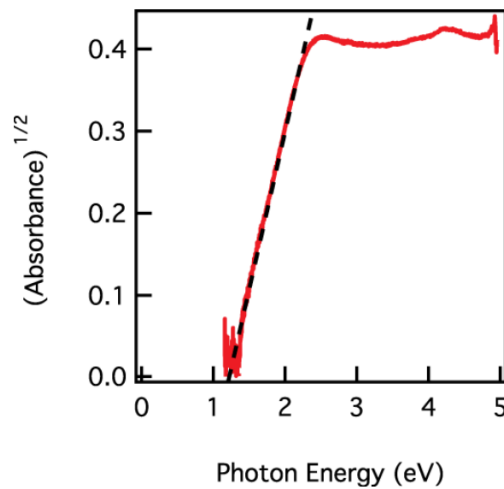


Figure 2.3 Corrected optical absorption spectrum of Cu_2S NWs dispersed in ethanol. Extrapolation of the linear fit of absorbance^{1/2} versus photon energy allowed the determination of the indirect

band gap of 1.20 eV. Reprinted with permission from ref. 1, © 2010 Wiley-VCH.

The uniqueness of this growth result is found in how sulfur and copper are fed to the propagating NWs. Existing reports of NW growth can be generally described by either base-feeding or tip-feeding mechanisms. When fed from the base, the new addition of species “pushes” up the NWs and leads to axial elongation.²⁰ Conversely, tip addition, as in a vapor–liquid–solid or solution-liquid-solid growth, is a common explanation for the elongation of NWs.^{21–22} The present synthesis, however, requires the addition of one component (sulfur) from the tip and the other component (copper) from the base. A surface diffusion model was proposed by Yang et al. to explain this phenomenon.^{10,23} Our observation of the existence of the Cu₂S buffer layer between the copper substrate and Cu₂S NWs seems to rule out the possibility of surface diffusion, and instead supports an internal diffusion model that we next identify as ionic vacancy diffusion.

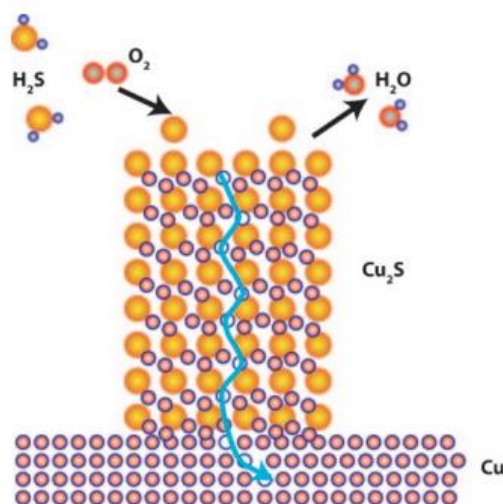


Figure 2.4 Schematic of the ionic vacancy diffusion growth model. Reprinted with permission from ref. 1, © 2010 Wiley-VCH.

Figure 2.4 illustrates the proposed growth mechanism. H₂S and O₂ react to produce H₂O and S²⁻. S²⁻ forms a close-packed sublattice, the polyhedral sites of which are to be occupied by Cu⁺. In the absence of Cu⁺, ionic vacancies (V_{Cu}') form, which subsequently diffuse in Cu₂S to reach

the copper substrate, where they are annihilated by defects in the copper. Initially this process yields a layer of Cu_2S that is continuous. As the reaction continues, the volumetric expansion, and also the annihilation of V_{Cu} by the defects in the Cu_2S film, leads to cracks in the Cu_2S film, creating NWs (Figure 2.5). Although the vacancy diffusion has been utilized to explain metal scale growth,²⁴ and it has been alluded to contribute to the Cu_2S NW growth,¹⁰ a detailed study to unambiguously validate this mechanism in governing NW growth had previously been absent.

We propose the following Cu_2S nanowire growth mechanism. H_2O , O_2 and H_2S molecules are adsorbed on the surface of the Cu substrate. (b) The presence of H_2O facilitates electron transfer to O_2 , leading to the disassociation of H_2S and producing H_2O , S^{2-} and electron holes. (c) S^{2-} and the holes are incorporated into the Cu_2S lattice, with S^{2-} packing to extend the existing lattice and the holes occupying Cu^+ sites. In effect, the holes can be regarded as Cu^+ vacancies (V_{Cu}). (d) V_{Cu} is highly mobile in the lattice of Cu_2S . The concentration difference of V_{Cu} near the interface of $\text{Cu}_2\text{S}/\text{Cu}$ (low) and that of $\text{Cu}_2\text{S}/\text{gas}$ (high) drives V_{Cu} to diffuse toward the $\text{Cu}_2\text{S}/\text{Cu}$ interface. Once reaching the Cu substrate, V_{Cu} is annihilated by structural defects in the crystal of Cu, in a way similar to the metal scale growth.²⁴ The total reaction can be expressed as:



As discussed above, H_2O facilitates electron transfer hence the reduction of O_2 . Adding H_2O in the beginning of the reaction significantly speeds up the reaction, permitting the growth of uniform Cu_2S nanowires. Because H_2O is also a product of Reaction (1), the overall growth of Cu_2S nanowires would in principle still occur even without the initial introduction of H_2O albeit slower. When H_2O was not intentionally added, we observed no appreciable formation of Cu_2S or Cu_2O in the first five hours of reactions. Prolonged reactions, e.g., 24 h, did yield detectable Cu_2S

nanostructures. However, the quality of the product was significantly lower than when H₂O was added. We suggest that the balance of the reaction kinetics of Reactions (1) and (2) is key to this observation, but will need further evidence to unravel the details. Other polar solvents such as ethanol were also used to replace H₂O. These solvents also facilitate charge transfer and hence O₂ reduction. While the formation of Cu₂S was observed after 5 h reactions, no distinguishable nanoscale features were seen. This phenomenon highlights the critical role of H₂O to the growth of aligned Cu₂S nanowires.

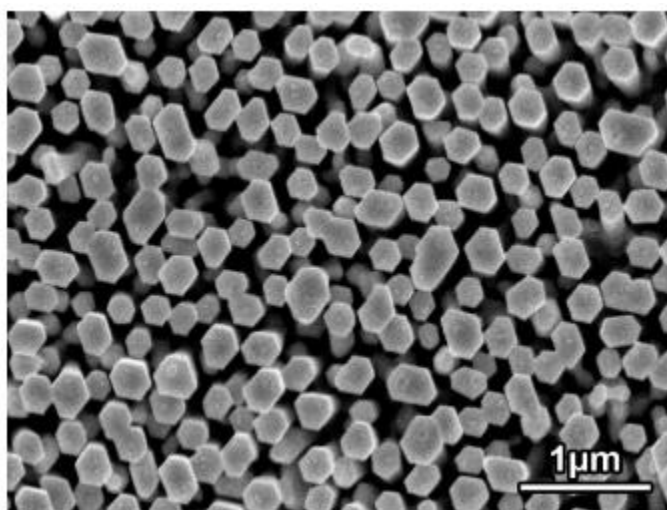


Figure 2.5 SEM top-view of the emerging Cu₂S NWs. Reprinted with permission from ref. 1, © 2010 Wiley-VCH.

From a perspective that concerns how ionic vacancies are annihilated in copper, we describe the following experimental observations to support our hypothesis. 1) The growth is highly sensitive to the quality of the substrate. Cu₂S nanostructures with random morphologies were obtained on copper substrates with high density of defects. The high density of defects facilitates rapid V_{Cu}' annihilation, which is equivalent to fast copper feeding. As a result, fast nanostructure growth occurs and produces random morphologies. For example, we frequently observed Cu₂S NWs as long as 100 μm on defective copper substrates (Figure 2.6). To further verify this hypothesis, we also fabricated micrometer-sized copper crystals by electrochemical deposition.

On small ($<10\ \mu\text{m}$) copper crystals, uniform epitaxial growth was obtained (Figure 2.7a). In contrast, a mixture of long and short NWs were grown on large crystals (Figure 2.7b), because more defects are present in these large crystals. Previous studies of the influence of the supporting substrate concerned how the crystallography changes the orientation of the as-grown NWs. To the best of our knowledge, this is the first report on how the nature of vacancy annihilation in the substrate determines the growth of NWs.



Figure 2.6 SEM image showing the binary growth of both long and short NWs on defect-rich deformed areas of the Cu foil. Reprinted with permission from ref. 1, © 2010 Wiley-VCH.

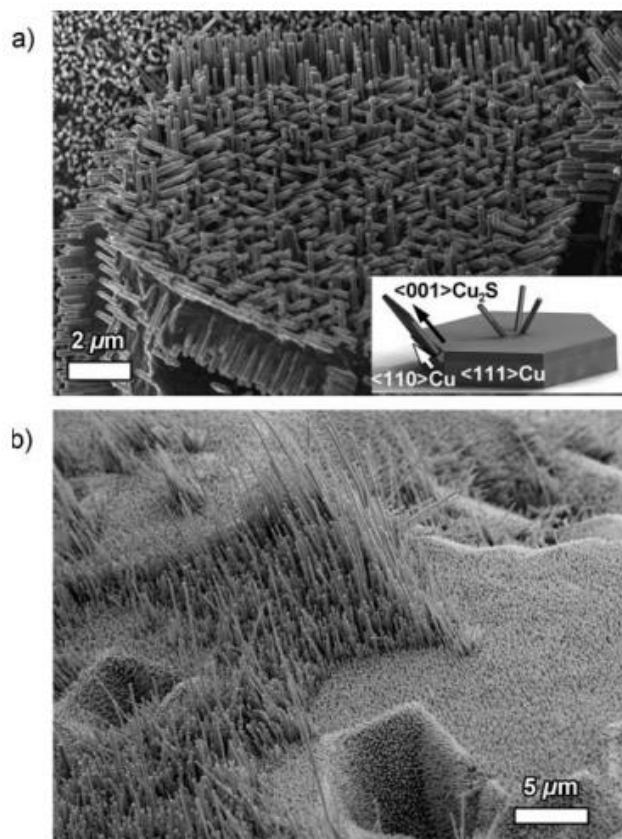


Figure 2.7 Various morphologies of Cu_2S NWs. a) Cu_2S grown on Cu microcrystals. b) Binary growth, which occurs when the Cu substrate is highly defective. Reprinted with permission from ref. 1, © 2010 Wiley-VCH.

2) H_2O plays a critical role in the growth. Control experiments in which H_2O was absent failed to produce detectable Cu_2S during the first 8 h of reactions. Random and short NWs were observed only after 24 h. Note that H_2O is also the product of the reaction between O_2 , H_2S , and Cu, which explains the eventual production of NWs in the absence of intentional H_2O supply. Humidity is known to facilitate electron transfer and ion formation in the growth of Cu_2S thin films.²⁵ The role of H_2O suggests that the growth depends on ionic behavior, and the dependence of the growth results on the relative humidity is quantitatively plotted in Figure 2.8. Despite the similarities of our system with what has been reported,²⁵ the role of H_2O has not been identified before.

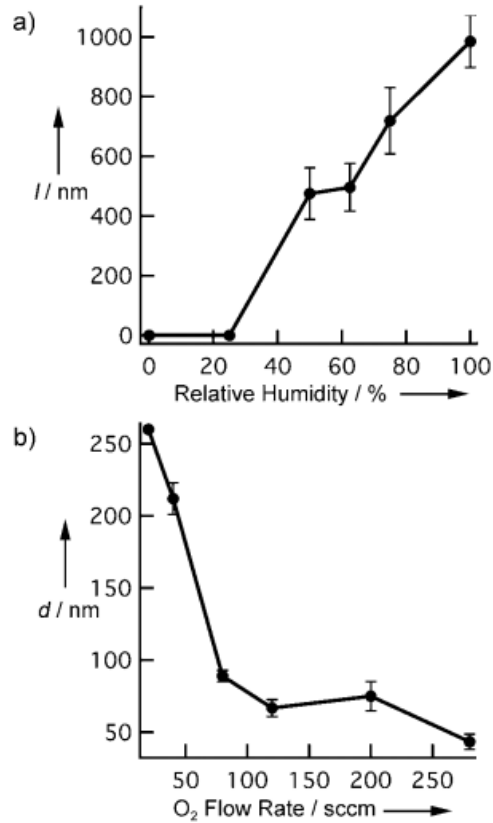


Figure 2.8 Influence of a) relative humidity and b) O₂ flow rate on the Cu₂S NW morphology (l : length, d : diameter) for a series of 3 h growths. Reprinted with permission from ref. 1, © 2010 Wiley-VCH.

3) In principle, $V_{\text{Cu}'}$ can be generated either on the tip or on the side walls of an existing Cu₂S nanowire. Nevertheless, $V_{\text{Cu}'}$ diffuses significantly faster along the [001] direction of Cu₂S, leading to the anisotropic growth and producing the NW morphology. The increase of the precursor concentrations will promote $V_{\text{Cu}'}$ generation, both on the tip and on the sidewalls. When the rate of $V_{\text{Cu}'}$ generation exceeds the rate of its diffusion, the growth cannot be sustained. As a result, thinner and shorter nanowires will be produced. This prediction was validated by our observations (Figure 2.8b), in which higher O₂ flow rate results in a higher O₂ concentration in the reactor, and thus faster $V_{\text{Cu}'}$ generation. Similarly, more H₂S is also predicted to produce smaller Cu₂S nanowires (Figure 2.9).

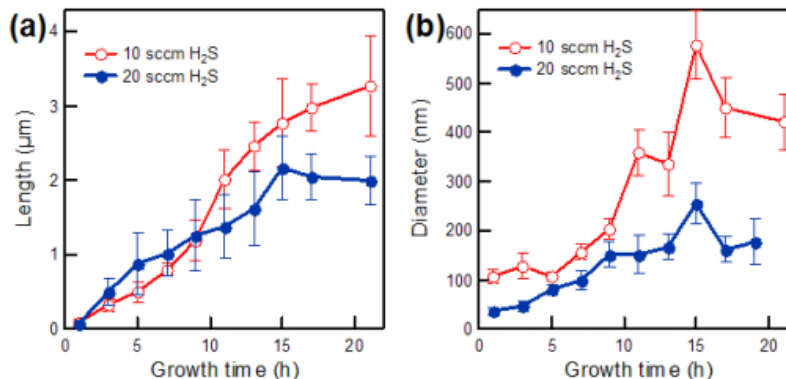


Figure 2.9 Cu₂S NW size dependence on H₂S gas flow rates. Reprinted with permission from ref. 1, © 2010 Wiley-VCH.

Although O₂ was a critical reagent, oxide formation was not observed in our experiments. We propose that the key role of O₂ is to oxidize copper and to subsequently react with H₂S, which produces H₂O. Cu_xO is not a necessary product of this reaction. We acknowledge that the oxide has been proposed previously to assist the nucleation, which governs the NW growth.¹⁰ However, we contend that the formation of NWs results from the vacancy in the thin film of Cu₂S, and no nucleation is involved in this process. Furthermore, Cu₂S nanostructures with varying degrees of complexity, ranging from double-comb to helical structures, that we obtained at room temperature (Figure 2.10) stemmed from the fast annihilation of V_{Cu}⁺ owing to the defective nature of the substrate. The effect of the fast annihilation is equivalent to fast feeding of Cu⁺; that is, the growth of Cu₂S NWs is governed by the diffusion of Cu⁺ vacancies in Cu₂S. Capabilities to balance the diffusion yield uniform NWs; failure to do so produces defective structures.

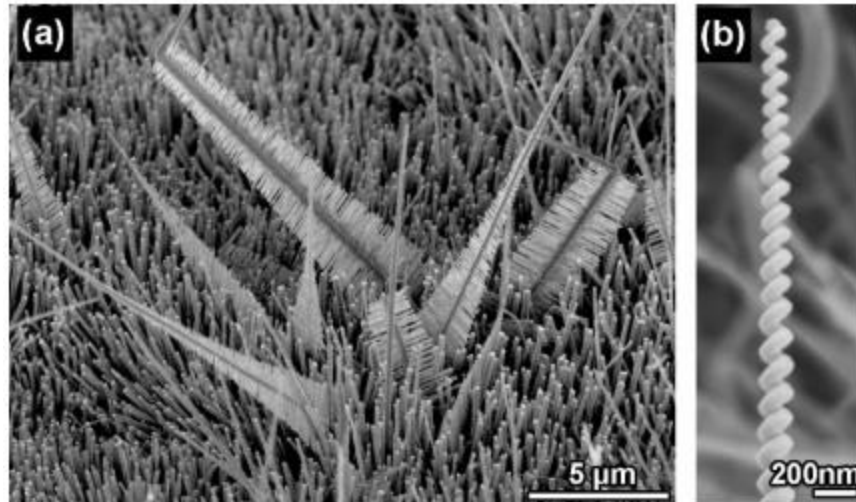


Figure 2.10 Unique Cu₂S nanostructures, including a) double-comb and b) helix. Reprinted with permission from ref. 1, © 2010 Wiley-VCH.

Cu⁺ diffusion in Cu₂S is a known issue that has plagued research of Cu₂S as a photovoltaic material. Indeed, the main reason of the structural complexity of Cu₂S comes from the high mobility of copper in the sulfur sublattice,²⁶ which is also responsible for the high conductivity of Cu₂S.²⁷ A growth that is facilitated by the ionic vacancy diffusion should therefore be reasonable. Similar ion-diffusion driven growth has been observed in Ag NW growth.²⁸ An ionic exchange reaction has also been used to create other chalcogenide nanostructures.²⁹ The model studied herein sheds light on the recent reports of low temperature growths of oxide nanostructures as well.³⁰⁻³¹

Understanding the ionic vacancy diffusion-governed growth leads to a significant implication: To minimize copper diffusion in Cu₂S nanostructures, the key will be to minimize the vacancy formation on the surface by minimizing excess sulfur surface sites. Minimizing the copper vacancy density leads to significantly reduced copper diffusion, which will enable the study of the true potential of using Cu₂S as a photovoltaic material.

In summary, we have discovered a unique growth model that produces uniform and aligned Cu₂S NWs at room temperature. Cu⁺ vacancy diffusion in Cu₂S was found as the driving force of this growth. H₂O acts as an indispensable reagent to facilitate charge transfer and ionic vacancy formation. The NW formation is governed by the difference of Cu⁺ vacancy diffusion in various crystal directions. We utilized the growth model to produce uniform NW arrays that can be potentially used to construct solar energy harvesting devices.

2.2 References

- 1 Liu, X.; Mayer, M. T.; Wang, D. Understanding Ionic Vacancy Diffusion Growth of Cuprous Sulfide Nanowires. *Angew. Chem. Int. Ed.* **2010**, *49*, 3165-3168.
- 2 Liu, X. H.; Mayer, M. T.; Wang, D. W. Negative differential resistance and resistive switching behaviors in Cu₂S nanowire devices. *Appl. Phys. Lett.* **2010**, *96*, 223103-223105.
- 3 Mayer, M. T.; Simpson, Z. I.; Zhou, S.; Wang, D. Ionic-Diffusion-Driven, Low-Temperature, Solid-State Reactions Observed on Copper Sulfide Nanowires. *Chem. Mater.* **2011**, *23*, 5045-5051.
- 4 Burgelman, M.; Pauwels, H. J. Theoretical advantages of p-n+-type Cu₂S-ZnO solar-cell. *Electron. Lett.* **1981**, *17*, 224-226.
- 5 Bragagnolo, J. A.; Barnett, A. M.; Phillips, J. E.; Hall, R. B.; Rothwarf, A.; Meakin, J. D. The design and fabrication of thin-film CdS-Cu₂S cells of 9.15-percent conversion efficiency. *IEEE Trans. Electron Dev.* **1980**, *27*, 645-651.
- 6 Martinuzzi, S. Trends and problems in CdS/Cu_xS thin film solar cells: A review. *Solar Cells* **1982**, *5*, 243-268.
- 7 Rothwarf, A. The CdS/Cu₂S solar cell: Basic operation and anomalous effects. *Solar Cells* **1980**, *2*, 115-140.
- 8 Pfisterer, F. The wet-topotaxial process of junction formation and surface treatments of Cu₂S-CdS thin-film solar cells. *Thin Solid Films* **2003**, *431*, 470-476.
- 9 Zhang, F.; Wong, S. S. Controlled Synthesis of Semiconducting Metal Sulfide Nanowires. *Chem. Mater.* **2009**, *21*, 4541-4554.
- 10 Zhang, W.; Yang, S. In Situ Fabrication of Inorganic Nanowire Arrays Grown from and Aligned on Metal Substrates. *Acc. Chem. Res.* **2009**, *42*, 1617-1617.
- 11 Wang, N.; Fung, K. K.; Wang, S.; Yang, S. Oxide-assisted nucleation and growth of copper sulphide nanowire arrays. *J. Cryst. Growth* **2001**, *233*, 226-232.
- 12 Wu, Y.; Wadia, C.; Ma, W.; Sadtler, B.; Alivisatos, A. P. Synthesis and photovoltaic application of copper(I) sulfide nanocrystals. *Nano Lett.* **2008**, *8*, 2551-2555.
- 13 Sigman, M. B.; Ghezelbash, A.; Hanrath, T.; Saunders, A. E.; Lee, F.; Korgel, B. A. Solventless synthesis of monodisperse Cu₂S nanorods, nanodisks, and nanoplatelets. *J. Am. Chem. Soc.* **2003**, *125*, 16050-16057.
- 14 Yuan, G.; Zhao, H.; Liu, X.; Hasanali, Z. S.; Zou, Y.; Levine, A.; Wang, D. Synthesis and Photoelectrochemical Study of Vertically Aligned Silicon Nanowire Arrays. *Angew. Chem. Int. Ed.* **2009**, *48*, 9680-9684.

- 15 Goodey, A. P.; Eichfeld, S. M.; Lew, K.-K.; Redwing, J. M.; Mallouk, T. E. Silicon nanowire array photoelectrochemical cells. *J. Am. Chem. Soc.* **2007**, *129*, 12344-+.
- 16 Kayes, B. M.; Atwater, H. A.; Lewis, N. S. Comparison of the device physics principles of planar and radial p-n junction nanorod solar cells. *J. Appl. Phys.* **2005**, *97*, 114302-114311.
- 17 Maiolo, J. R., III; Kayes, B. M.; Filler, M. A.; Putnam, M. C.; Kelzenberg, M. D.; Atwater, H. A.; Lewis, N. S. High aspect ratio silicon wire array photoelectrochemical cells. *J. Am. Chem. Soc.* **2007**, *129*, 12346-+.
- 18 Xiao, Y.; Chen, J.; Deng, S. Z.; Xu, N. S.; Yang, S. Preparation of Cu₂S dendritic, double-comb-like nanostructures by gas-solid reaction method. *J. Nanosci. Nanotech.* **2008**, *8*, 237-243.
- 19 Partain, L. D.; McLeod, P. S.; Duisman, J. A.; Peterson, T. M.; Sawyer, D. E.; Dean, C. S. Degradation of a Cu₂S/CdS solar-cell in hot, moist air and recovery in hydrogen and air. *J. Appl. Phys.* **1983**, *54*, 6708-6720.
- 20 Xia, Y. N.; Yang, P. D.; Sun, Y. G.; Wu, Y. Y.; Mayers, B.; Gates, B.; Yin, Y. D.; Kim, F.; Yan, Y. Q. One-dimensional nanostructures: Synthesis, characterization, and applications. *Adv. Mater.* **2003**, *15*, 353-389.
- 21 Holmes, J. D.; Johnston, K. P.; Doty, R. C.; Korgel, B. A. Control of thickness and orientation of solution-grown silicon nanowires. *Science* **2000**, *287*, 1471-1473.
- 22 Wagner, R. S.; Ellis, W. C. Vapor-liquid-solid mechanism of single crystal growth. *Appl. Phys. Lett.* **1964**, *4*, 89-&.
- 23 Wang, S. H.; Yang, S. H. Growth of crystalline Cu₂S nanowire arrays on copper surface: Effect of copper surface structure, reagent gas composition, and reaction temperature. *Chem. Mater.* **2001**, *13*, 4794-4799.
- 24 Pieraggi, B.; Rapp, R. A. Stress generation and vacancy annihilation during scale growth limited by cation vacancy diffusion. *Acta Metall.* **1988**, *36*, 1281-1289.
- 25 Sullivan, J. P.; Barbour, J. C.; Missert, N. A.; Copeland, R. G.; Mayer, M.; Campin, M. "The effects of varying humidity on copper sulfide film formation," Sandia National Laboratories, 2004.
- 26 Lukashev, P.; Lambrecht, W. R. L.; Kotani, T.; van Schilfgaarde, M. Electronic and crystal structure of Cu_(2-x)S: Full-potential electronic structure calculations. *Phys Rev B* **2007**, *76*, 195202.
- 27 Hirahara, E. The Electrical Conductivity and Isothermal Hall Effect in Cuprous Sulfide, Semi-Conductor. *J. Phys. Soc. Jap.* **1951**, *6*, 428-437.
- 28 Cao, Y.; Liu, W.; Sun, J. L.; Han, Y. P.; Zhang, J. H.; Liu, S.; Sun, H. S.; Guo, J. H. A technique for controlling the alignment of silver nanowires with an electric field. *Nanotechnology* **2006**, *17*, 2378-2380.
- 29 Son, D. H.; Hughes, S. M.; Yin, Y. D.; Alivisatos, A. P. Cation exchange reactions in ionic nanocrystals. *Science* **2004**, *306*, 1009-1012.
- 30 Wen, X. G.; Fang, Y. P.; Pang, Q.; Yang, C. L.; Wang, J. N.; Ge, W. K.; Wong, K. S.; Yang, S. H. ZnO nanobelt arrays grown directly from and on zinc substrates: Synthesis, characterization, and applications. *Journal of Physical Chemistry B* **2005**, *109*, 15303-15308.
- 31 Wen, X.; Wang, S.; Ding, Y.; Wang, Z. L.; Yang, S. Controlled Growth of Large-Area, Uniform, Vertically Aligned Arrays of α -Fe₂O₃ Nanobelts and Nanowires. *J. Phys. Chem. B* **2004**, *109*, 215-220.

Chapter 3

Ionic behavior revealed by electronic phenomena on Cu₂S/ZnO

This chapter is adapted from: Liu, X. H.; Mayer, M. T.; Wang, D. W. Negative differential resistance and resistive switching behaviors in Cu₂S nanowire devices. *Appl. Phys. Lett.* **2010**, *96*, 223103-223105

Cu₂S, as a cation-deficient p-type semiconductor with a band gap of 1.2 eV, can potentially be used to interface with n-type semiconductors such as CdS or ZnO to make p-n junction photovoltaic devices.¹⁻² The high mobility of ionic Cu, however, has been identified as a culprit of degradation of the junction and therefore instability of solar cell performance. Research on photovoltaic Cu₂S seemed to be widely abandoned around two decades ago,³ but recent advancements in the synthesis and characterization of nanostructured morphologies has renewed the interest in the material.⁴⁻⁷ In the previous chapter it was shown that the high mobility of Cu⁺ vacancies in Cu₂S is the driving force in the unique growth of vertically-aligned Cu₂S nanowires,⁴ a promising morphology that could rejuvenate research on Cu₂S for solar energy harvesting.

Nevertheless, to reach this goal it is essential to understand the properties of Cu⁺ in Cu₂S and particularly at the interface of the p-n junction. This section reports our discovery of electronic and ionic phenomena observed on Cu₂S NW-based devices.⁸ We found that when interfaced with ZnO, Cu₂S exhibits obvious negative differential resistance (NDR) along with a resistive switching (RS). We propose that these observations can be accounted for by the high mobility of Cu⁺ in response to an electric field. Our results shed light on the nature of the p-n junctions using Cu₂S and highlight the necessity to account for diffusion of cations in Cu₂S for electronic applications.

The synthesis of vertically aligned Cu₂S nanowires on Cu foil was carried out as described in the previous section. Arrays of vertical Cu₂S nanowires, approximately 100 nm wide and 2

μm long, were obtained. The resulting samples were transferred to an atomic layer deposition (ALD, Savannah 100, Cambridge Nanotech) chamber for deposition of ZnO thin films. Diethyl zinc (ZnEt_2) and H_2O served as the precursors, and the reaction took place at 100°C .⁹ For imaging by TEM and SEM, thin ZnO films (~ 50 nm) were grown; thicker films (~ 200 nm) were used for the measurements. The electronic measurements were conducted on a probe station (Cascade Microtech, M150 Measurement Platform) connected to a source meter (Keithley 2400) controlled by a computer through a LabView program. The underlying Cu substrate on which Cu_2S was grown served as one contact and a tungsten or gold tip (radius < 2.4 μm) gently touching the ZnO from the top was the other contact, as shown in Figure 3.1. The ZnO-contacting electrode was grounded for all data presented here. Control experiments where the ZnO coating was absent were performed in the same fashion except that the top contact was made directly to the Cu_2S nanowires.

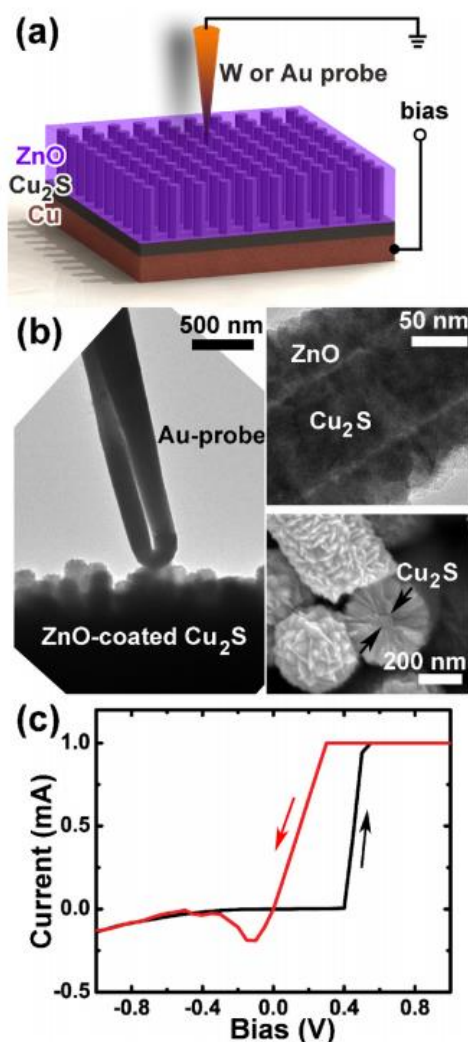


Figure 3.1 (a) Schematic of the ZnO/Cu₂S nanowires and measurement configuration. (b) A TEM image showing the contact between the sample and a probe. The insets show the side view (upper) and the cross section (lower) of the core/shell structure. Thicker ZnO coatings (~ 200 nm) were used in the measurements. (c) A typical I-V curve showing both the NDR and RS features. The plateau in anodic current at 1 mA results from the compliance-limited current of the measurement. Reprinted with permission from ref. ⁸, © 2011 American Institute of Physics.

A typical I-V plot is shown in Figure 3.1c, and a more detailed version with varied scan rates is shown in Figure 3.2. Three important features were observed. First, the forward scan produced an I-V plot characteristic of a p-n diode. The turn-on voltage, however, depended on the rate the bias voltage was scanned, as shown in Figure 3.2. Second, the reverse scan yielded a low-

resistance state, which extended to voltages in the negative range. The I-V curve resulting from the reverse scan was typified by a good linearity in the low voltage region, demonstrating the behaviors of a resistor that does not rectify current. Third, a NDR behavior was observed in the negative voltage range, the precise voltages varying with the voltage scan rates. The NDR effect was mostly suppressed at extremely slow scan rates such as 2 mV/s (Figure 3.2a).

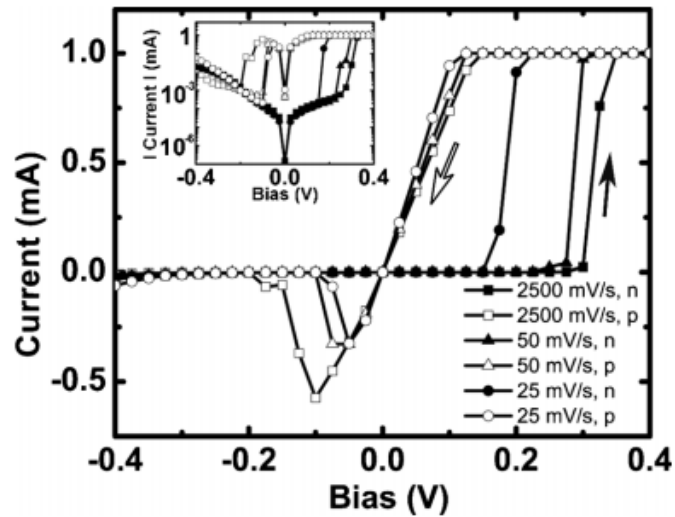


Figure 3.2 I-V scans of a ZnO/Cu₂S device at various scan rates. Reprinted with permission from ref. ⁸, © 2011 American Institute of Physics.

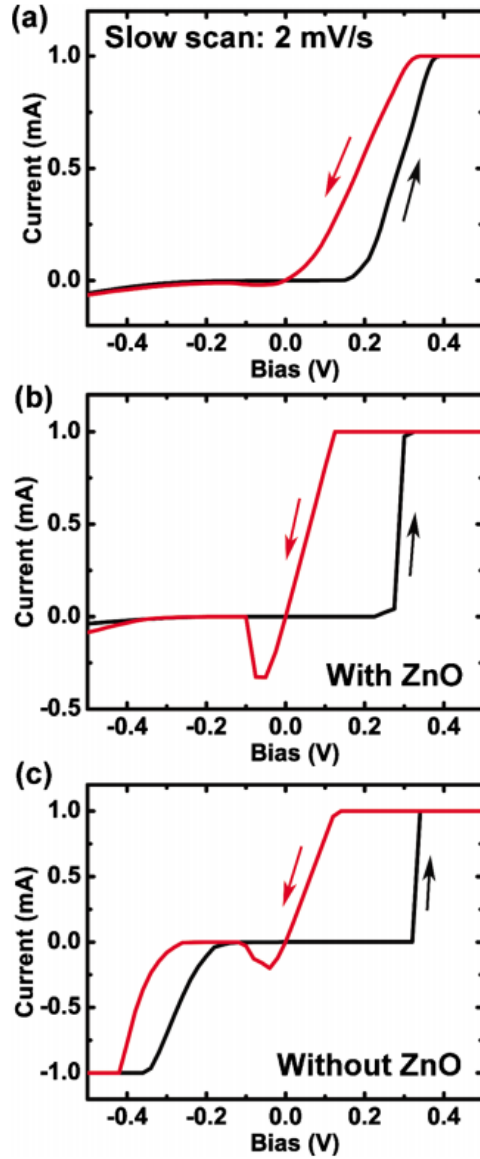


Figure 3.3 (a) The NDR peak diminishes at slow scan rate of 2 mV/s. (b) and (c) Comparison of I-V plots with or without ZnO, respectively. Reprinted with permission from ref. ⁸, © 2011 American Institute of Physics.

RS and NDR phenomena have been reported earlier in a number of semiconductor systems, including TiO_2 ,¹⁰⁻¹¹ NiO ,¹² ZnO/SiO_x ,¹³ Co_3O_4 ,¹⁴ and Cu_2S .¹⁵⁻¹⁶ Compared with those reports, the present result seems to be unique in both the I-V characteristics and the governing mechanism. As described above, the typical I-V curves include two nonlinear behaviors, the rectifying diode

behavior and a RS behavior, both of which are well-defined and reproducible. The introduction of ZnO to form a p-n junction with Cu₂S results in the restricting of the NDR peak to the negative bias range and the RS behavior to the positive bias range. These features and the low operating potentials make it conceivable to use this heterojunction structure for unique electronic device fabrications.

We propose that the origin of the observed NDR and RS lies in the high mobility of Cu⁺.^{4,17} When not externally biased, the Cu₂S/ZnO interface represents that of a semiconductor p-n junction. The initial forward bias scan indeed produces current behavior resembling that of a diode. The forward bias, however, produces an additional effect on the interface, driving Cu⁺ to accumulate in Cu₂S near the Cu₂S/ZnO interface.

This accumulation likely serves to decrease the level of p-type doping in the Cu₂S, which weakens the junction as the forward bias is increased or sustained for long durations. The weakening effect prompts the abrupt turn-on of the forward I-V curve as the diode characteristic is removed. When the forward bias is reduced during backward scan from positive to negative, the weakened p-n junction is not immediately restored and it maintains the low-resistance state even below the original turn-on voltage. The linearity of the I-V curve in the low bias range is the characteristic of this low-resistance state. Once the bias is swept into the negative range and the bias polarity is reversed, the accumulated Cu⁺ is gradually removed from the junction area, allowing the p-n junction to reestablish. Eventually the resistance increases to limit the negative current flow, producing the NDR observed as a downward peak in the negative bias region (Figure 3.1c).

This hypothesis is supported by the scan rate dependence of the I-V plots. As shown in Figure 3.2, when the scan rate is high (2500 mV/s), the diode was turned on at a large bias (0.3

V). This is because at a fast scan rate, the Cu^+ accumulation lags behind the rapidly increasing bias, and hence a larger bias is reached before the turn-on state is achieved. Conversely, with slower scan rates, the turn-on voltages were reduced, the reduction in the turn-on voltage depending on the scan rate in a monotonic fashion. Similarly, the height and the position of the NDR peaks varied with the scan rate. The highest and the most negative NDR peak was observed when a 2500 mV/s scan rate was used (the fastest scan rate tested). This phenomenon is related to the rate at which the accumulated Cu^+ is dissipated. The dissipation of ions leads to the reinstallation of the $\text{Cu}_2\text{S}/\text{ZnO}$ diode, which is the primary reason for the NDR behavior. Consistent with this hypothesis, the NDR peak was not observed at the extremely slow scan rate of 2 mV/s because at such a rate the accumulated Cu^+ has sufficient time to dissipate before reaching the NDR region (Figure 3.3a). Note that at this slow scan rate, the RS behavior is still pronounced. This observation supports the hypothesis that Cu^+ ion behaviors are the primary cause for the NDR and RS. The on/off switching was found to be highly reversible, which we attribute to the reversibility of Cu^+ diffusion within this bias range.

ZnO plays an important role in these observations. As shown in Figure 3.3, the incorporation of ZnO introduces a rectifying diode to the device, which helps suppress the current in the reverse bias (negative) region. The suppressed reverse current makes it possible to distinguish the different features of the I-V curves in the forward and reverse bias regions. Although similar NDR and RS behaviors were observed in the control experiments on bare Cu_2S without ZnO (Figure 3.3c), the nature of the properties is different. When Cu_2S is contacted by a metal directly, the Cu^+ accumulation and dissipation changes the Schottky barrier height, which induces the conductance change. The lack of rectification of the I-V curve, however, can make the NDR difficult to observe. While it is important to have a diode to rectify the current, the exact nature of the diode plays an insignificant role in the phenomenon that drives the behaviors, namely Cu^+ ion

diffusion. In a similar test where ZnO was replaced by CdS, another n-type semiconductor, we found comparable RS and NDR effects.

The modulation of resistance as a response to bias polarity has been the topic of much research lately. The mechanisms often employed to explain the observation usually involves charge trapping/detrapping, ion/defect diffusion, and/or redox reactions. Specifically, the formation and dissolution of conductive metallic filaments has sometimes been adopted to explain the RS phenomena based on Cu₂S materials.¹⁶ The ionic accumulation mechanism we proposed here is distinct from the existing models but is based on similar considerations of the ionic nature of Cu₂S. While further studies are needed to compare and distinguish these models, the result presented here sheds light on the detrimental aspects of the high mobility of Cu⁺ in utilizing Cu₂S for solar energy harvesting. Therefore, it will be important to understand and control the interface Cu₂S forms with n-type semiconductors in such a device.

In conclusion, we observed resistance switching and negative differential resistance in Cu₂S nanowire-based devices. These behaviors were explained using the high ionic mobility of Cu⁺ in Cu₂S. The high reproducibility and low operating potential of the resistance switching could prove useful in efforts to use Cu₂S in solid-state memory storage devices, such as in a memristor. The result also provides insight to Cu₂S-based p-n junctions, providing more evidence of the challenges of using an ion-diffusive semiconductor in energy-conversion applications.

3.1 References

- 1 Burgelman, M.; Pauwels, H. J. Theoretical advantages of p-n⁺-type Cu₂S-ZnO solar-cell. *Electron. Lett.* **1981**, *17*, 224-226.
- 2 Bragagnolo, J. A.; Barnett, A. M.; Phillips, J. E.; Hall, R. B.; Rothwarf, A.; Meakin, J. D. The design and fabrication of thin-film CdS-Cu₂S cells of 9.15-percent conversion efficiency. *IEEE Trans. Electron Dev.* **1980**, *27*, 645-651.
- 3 Partain, L. D.; McLeod, P. S.; Duisman, J. A.; Peterson, T. M.; Sawyer, D. E.; Dean, C. S. Degradation of a Cu₂S/CdS solar-cell in hot, moist air and recovery in hydrogen and air. *J. Appl. Phys.* **1983**, *54*, 6708-6720.

- 4 Liu, X.; Mayer, M. T.; Wang, D. Understanding Ionic Vacancy Diffusion Growth of Cuprous Sulfide Nanowires. *Angew. Chem. Int. Ed.* **2010**, *49*, 3165-3168.
- 5 Sigman, M. B.; Ghezelbash, A.; Hanrath, T.; Saunders, A. E.; Lee, F.; Korgel, B. A. Solventless synthesis of monodisperse Cu₂S nanorods, nanodisks, and nanoplatelets. *J. Am. Chem. Soc.* **2003**, *125*, 16050-16057.
- 6 Wang, S. H.; Yang, S. H. Growth of crystalline Cu₂S nanowire arrays on copper surface: Effect of copper surface structure, reagent gas composition, and reaction temperature. *Chem. Mater.* **2001**, *13*, 4794-4799.
- 7 Wu, Y.; Wadia, C.; Ma, W.; Sadtler, B.; Alivisatos, A. P. Synthesis and photovoltaic application of copper(I) sulfide nanocrystals. *Nano Lett.* **2008**, *8*, 2551-2555.
- 8 Liu, X. H.; Mayer, M. T.; Wang, D. W. Negative differential resistance and resistive switching behaviors in Cu₂S nanowire devices. *Appl. Phys. Lett.* **2010**, *96*, 223103-223105.
- 9 Yamada, A.; Sang, B. S.; Konagai, M. Atomic layer deposition of ZnO transparent conducting oxides. *Appl. Surf. Sci.* **1997**, *112*, 216-222.
- 10 Pickett, M. D.; Strukov, D. B.; Borghetti, J. L.; Yang, J. J.; Snider, G. S.; Stewart, D. R.; Williams, R. S. Switching dynamics in titanium dioxide memristive devices. *J. Appl. Phys.* **2009**, *106*, 074508.
- 11 Yang, J. J.; Pickett, M. D.; Li, X.; Ohlberg, D. A. A.; Stewart, D. R.; Williams, R. S. Memristive switching mechanism for metal/oxide/metal nanodevices. *Nature Nanotechnology* **2008**, *3*, 429-433.
- 12 Seo, S.; Lee, M. J.; Seo, D. H.; Jeoung, E. J.; Suh, D. S.; Joung, Y. S.; Yoo, I. K.; Hwang, I. R.; Kim, S. H.; Byun, I. S.; Kim, J. S.; Choi, J. S.; Park, B. H. Reproducible resistance switching in polycrystalline NiO films. *Appl. Phys. Lett.* **2004**, *85*, 5655-5657.
- 13 Yang, Y.; Qi, J.; Guo, W.; Qin, Z.; Zhang, Y. Electrical bistability and negative differential resistance in single Sb-doped ZnO nanobelts/SiO_x/p-Si heterostructured devices. *Appl. Phys. Lett.* **2010**, *96*, 093107.
- 14 Nagashima, K.; Yanagida, T.; Oka, K.; Taniguchi, M.; Kawai, T.; Kim, J.-S.; Park, B. H. Resistive Switching Multistate Nonvolatile Memory Effects in a Single Cobalt Oxide Nanowire. *Nano Lett.* **2010**, *10*, 1359-1363.
- 15 Sakamoto, T.; Sunamura, H.; Kawaura, H.; Hasegawa, T.; Nakayama, T.; Aono, M. Nanometer-scale switches using copper sulfide. *Appl. Phys. Lett.* **2003**, *82*, 3032-3034.
- 16 Waser, R.; Aono, M. Nanoionics-based resistive switching memories. *Nat. Mater.* **2007**, *6*, 833-840.
- 17 Tsuchiya, T.; Oyama, Y.; Miyoshi, S.; Yamaguchi, S. Nonstoichiometry-Induced Carrier Modification in Gapless Type Atomic Switch Device Using Cu₂S Mixed Conductor. *Appl. Phys. Exp.* **2009**, *2*, 055002.

Chapter 4

Ionic diffusion driven solid-state conversions of Cu₂S nanowires

This chapter is adapted from: Mayer, M. T.; Simpson, Z. I.; Zhou, S.; Wang, D. Ionic-diffusion-driven, low-temperature, solid-state reactions observed on copper sulfide nanowires. *Chem. Mater.* **2011**, *23*, 5045-5051

Although the ionic-electronic phenomena detailed above were indeed interesting discoveries, the ultimate goal was to use the Cu₂S NW arrays in PV or PEC devices. However, our attempts, including making heterojunction devices with n-type materials ZnO or CdS, consistently gave poor performance and unstable behaviors. Ultimately we attributed these difficulties to the diffusive Cu⁺ within Cu₂S as the main culprit. While there are conceivably approaches that could be taken to address and compensate for this problem, such as perhaps modifying the Cu₂S with another metal cation aimed at suppressing ionic diffusion,¹ we did not have a clear idea how such an approach could be incorporated into our desirable room-temperature NW synthesis procedure. Instead, we postulated whether we could use this ionic diffusivity to our advantage, using the as-grown NWs as starting materials for solid-state conversions to other useful compositions whilst maintaining the desired NW morphology.²

Upon combining and heating solid-phase reactants (such as semiconductors and metals), they can react to yield new materials. These diffusion-driven reactions provide an approach to forming materials with controllable binary, ternary, or polynary compositions. A large number of semiconducting, superconducting, ionic conducting, and magnetic materials have been synthesized using this method.³ Recently, solid-state reactions have been used to generate targeted morphologies, including nanowires (NWs) or nanotubes (NTs).⁴⁻⁶ The nature of solid-state reactions, however, dictates that they proceed at intrinsically slow paces as they are driven by relatively slow diffusion processes (as compared to solution or vapor diffusion). As such, high

temperatures (500–2000 °C), high pressures, or combinations of the two are usually necessary, limiting the versatility of such reactions. For example, Gösele et al. demonstrated the Kirkendall effect-driven formation of hollow structures resulting from heating interfaces between metal oxide heterostructures at temperatures of 500–800 °C.⁷⁻⁸ Others have used similar heat-driven solid-state diffusion processes to form unique nanostructures, including Lieber et al.,⁹ Wang et al.,¹⁰ Buhro et al.,¹¹ and others.^{4,12-13} In each case, temperatures exceeding 500 °C were needed to overcome the significant thermal diffusion barriers. Meanwhile, conversion of nanostructures has been well-demonstrated using solution-based (wet) chemistry at significantly lower temperatures, using solvent- or solute-mediated ion exchange as a driving force.⁶ For example, researchers have used chemical reagents to selectively extract chalcogen anions,¹⁴ or metal cations,¹⁵⁻¹⁶ preserving the nanocrystal size and shape in the converted product. However, solvent-free all-solid-state reactions of nanomaterials have been comparatively rare.

Using Cu₂S NWs as the model starting material, we reported a novel phenomenon that enables solvent-free solid-state reactions at ambient pressure at temperatures as low as 105 °C.² Driven by the diffusivity of metal ions in the S sublattice, the reactions are shown to yield either unique heteronanostructures such as rod-in-a-tube (RIT) or segmented NWs or fully converted NWs. This mechanism suggests the promise of using nanomaterial templates for solid-state conversions to desired compositions.

Central to the discovery are Cu₂S NWs formed on Cu following a cation-vacancy-diffusion model described at the start of this chapter,¹⁷ facilitated by the high diffusivity of Cu⁺ within Cu₂S that has hindered its utilization in photovoltaics¹⁸⁻²⁰ but has allowed for its application in memory storage devices²¹⁻²² and solution-phase ion-exchange reactions.^{15-16,23} Here, we further exploit the diffusivity and discover that it can be used to create nanostructures more complex than simple NWs or nanorods. Utilizing the Cu₂S NWs as a template, we were able to generate three distinct

morphologies (i.e., RITs, segmented NWs, and fully converted NWs) at temperatures significantly lower than those normally required for solid-state reactions. We distinguish the results from the well-established but fundamentally different solution-based approaches.¹⁵⁻
¹⁶ Interestingly, the natures of the reactions were dependent on the nanowire–substrate interface (Cu_2S –Cu), across which Cu transport seems to take place.

The synthesis of Cu_2S NW arrays was performed as described previously.¹⁷ NW growth was followed by deposition of either Fe or Zn films. Thin films of Fe were deposited onto as-grown Cu_2S NWs using an AJA International ATC Orion 8 sputtering system. A deposition thickness of approximately 20 nm was used in this study. The deposition rate was approximately 0.3 Å/s in all instances of Fe deposition. Thin films of Zn were deposited by thermal evaporation onto as-grown Cu_2S using a Sharon Vacuum evaporation system. The thicknesses of the Zn coatings were varied between 20 and 120 nm.

As-deposited $\text{Cu}_2\text{S}/\text{Fe}$ NW arrays were heated in a tube furnace at 105 °C for 30 min under a mix gas flow of N_2 (250 sccm) and H_2S (12 sccm). The annealing procedure for Zn-coated Cu_2S was similar to that of Fe-coated NWs, except that the Zn incorporation was found to take place with or without the presence of H_2S . In this case, the temperature was varied in the range 105–200 °C, and reaction times were fixed at 30 min.

4.1 Fe– Cu_2S System

Our interest in the Fe– Cu_2S system was prompted by the potential of pyrite (FeS_2),²⁴ chalcopyrite (CuFeS_2),²⁵ and related materials in electronic, magnetic, and energy-related applications. Controlled syntheses of these materials in NW morphologies, particularly in a vertically aligned form, have not been reported previously. We therefore sought to use

conversion reactions of Cu_2S as an approach toward creating such materials in the desired morphology.

As shown in Figure 4.1, the heating of Fe-coated Cu_2S NWs produced an RIT morphology composed of a rod and a tube, each being a discrete structure. We used sputtered thin films of Fe (approximately 20 nm) on Cu_2S NWs as the starting material, followed by a brief (30 min) heat treatment under a gas flow of 5% H_2S and 95% N_2 (by volume) at 105 °C, to produce the morphology depicted in Figure 4.1c.

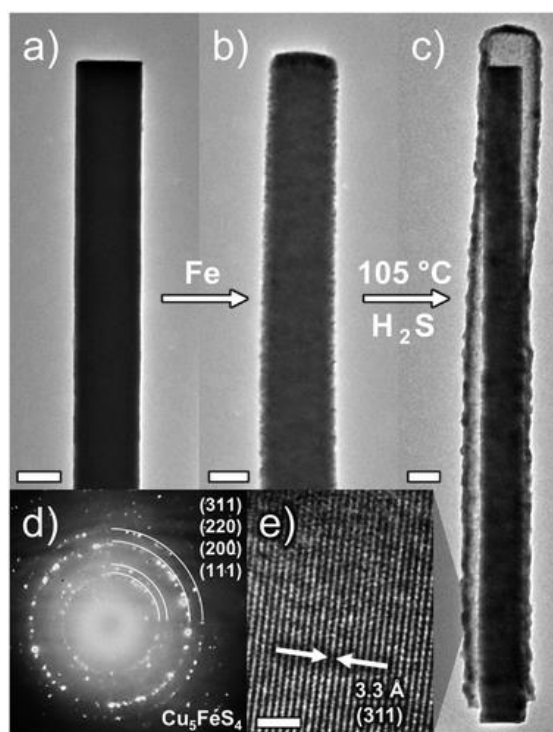


Figure 4.1 Reaction of Fe-coated Cu_2S NWs to produce the rod-in-a-tube (RIT) morphology. TEM images of (a) an as-grown Cu_2S NW, (b) a NW after coating with 20 nm sputtered Fe, and (c) the RIT morphology resulting from heating for 30 min in H_2S (scale bars: 100 nm). (d) Electron diffraction pattern of the tube material, indexed to the bornite Cu_5FeS_4 phase (JCPDS no. 83.2266). (e) High-resolution TEM shows the tube's crystalline quality (scale bar: 2 nm). Reprinted with permission from ref. ², © 2011 American Chemical Society.

TEM examination revealed that the rod and tube in each RIT are clearly separated by a hollow void, distinguishing the RIT morphology from the oft-encountered core/shell morphologies. Low-magnification TEM images showed that the tubes were continuous from their base, where the NWs were physically connected to the Cu substrate from which they grew, to the encapsulated tip (Figure 4.1c). The walls of the tubes varied in thickness in the range 25–50 nm. High-resolution TEM indicated the polycrystalline nature of the tubes, with grain sizes between 5 and 30 nm (Figure 4.1e and Figure 4.2), consistent with the interpretation of the electron diffraction (ED) patterns (Figure 4.1d). Elemental analysis of the tube material using energy dispersive X-ray spectroscopy (EDS) revealed the average ternary composition of 54.5% Cu, 12.4% Fe, and 33.1% S, in good agreement with the ED characterizations, whose patterns were indexed to the Cu_5FeS_4 phase (JCPDS no. 83-2266). Several factors may contribute to the observed stoichiometry deviation, including the inaccuracies of analysis by EDS in the TEM and the possibility of excess Cu and Fe due to incomplete reaction.

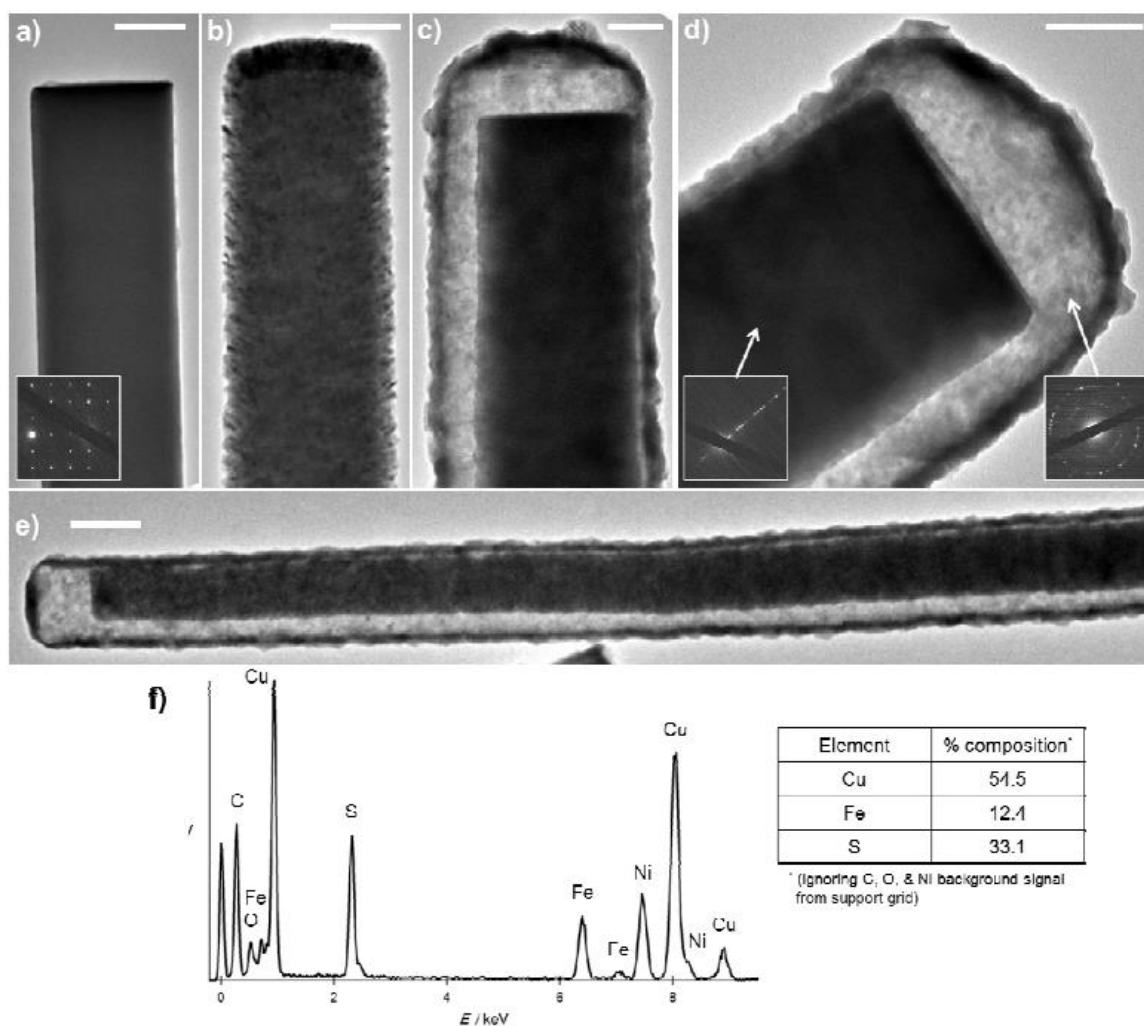


Figure 4.2 Detailed TEM images of the Fe-Cu₂S reaction. (a) As-grown Cu₂S NW, (b) Fe-coated NW, (c)-(e) RIT morphology (scale bars: 100 nm in a-d, 200 nm in e), (f) elemental composition analysis by EDS of the tube material.

We suggest that the reaction proceeds by a mechanism similar to the Kirkendall effect, in which the diffusion of Cu⁺ ions is the key process. As shown in the schematic of Figure 4.3, the sulfidation of Fe, in which H₂S serves as an oxidizer and sulfur source, creates ionic vacancies in the shell which drive the outward diffusion of Cu⁺. EDS examination revealed the presence of some Fe in the internal rods after the reaction was complete, suggesting Fe²⁺ ions also diffuse inward, albeit to a lesser extent. A significant amount of Cu⁺ diffuses out into the shell.

Accumulation of vacancies at the core–shell interface, as well as the continuous sulfidation of the shell, ultimately leads to the separation and expansion to yield the RIT morphology. The separation likely cuts off the routes of Cu^+ diffusion into the shell and further expansion results from the continued supply of sulfur from the gas phase. To support these observations, reports have shown that Cu diffuses faster than Fe in chalcopyrite CuFeS_2 ; within the temperature range of 100–300 °C, the diffusion coefficients for Cu and Fe are on the order of 9.4×10^{-7} and 5.4×10^{-12} cm^2/s , respectively.²⁶ Differing from a typical Kirkendall process, however, the core NW does not seem to be consumed by the process, but rather a continuous supply of Cu from the substrate is provided. This hypothesis is supported by several following observations.

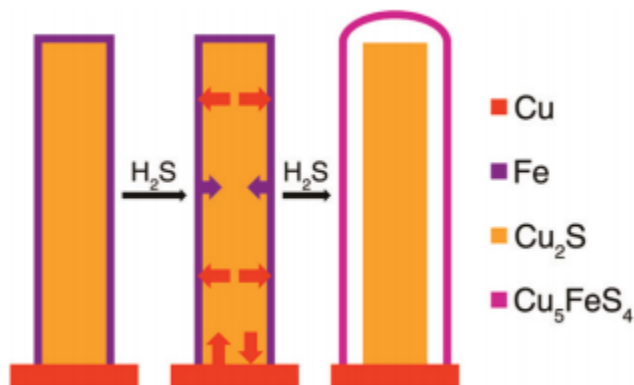


Figure 4.3 Schematic depicting the RIT formation reaction. Reprinted with permission from ref. ², © 2011 American Chemical Society.

First, when the supply of diffusive Cu^+ was disrupted, the RIT morphology became less pronounced or even entirely absent. Cu^+ diffusion disruption was accomplished by three methods: electron beam (e-beam) irradiation, the removal of Cu_2S NWs from the underlying Cu substrate, and the use of an intermediate blocking layer of Al_2O_3 . Our previous studies found that Cu in Cu_2S can be affected by irradiation under a high-energy e-beam which concentrates Cu^+ within the NWs and hence reduces its mobility.¹⁷ In this study, we tried exposing the Fe-coated NWs to TEM e-beam (200 keV in energy) prior to the heat treatment in H_2S and discovered that the RIT

morphology did not form. Meanwhile, nearby unexposed NWs on the same substrate reacted normally to yield the RIT morphology (Figure 4.4a–c). We concluded from this set of experiments that Cu^+ diffusion was disrupted by the e-beam irradiation.

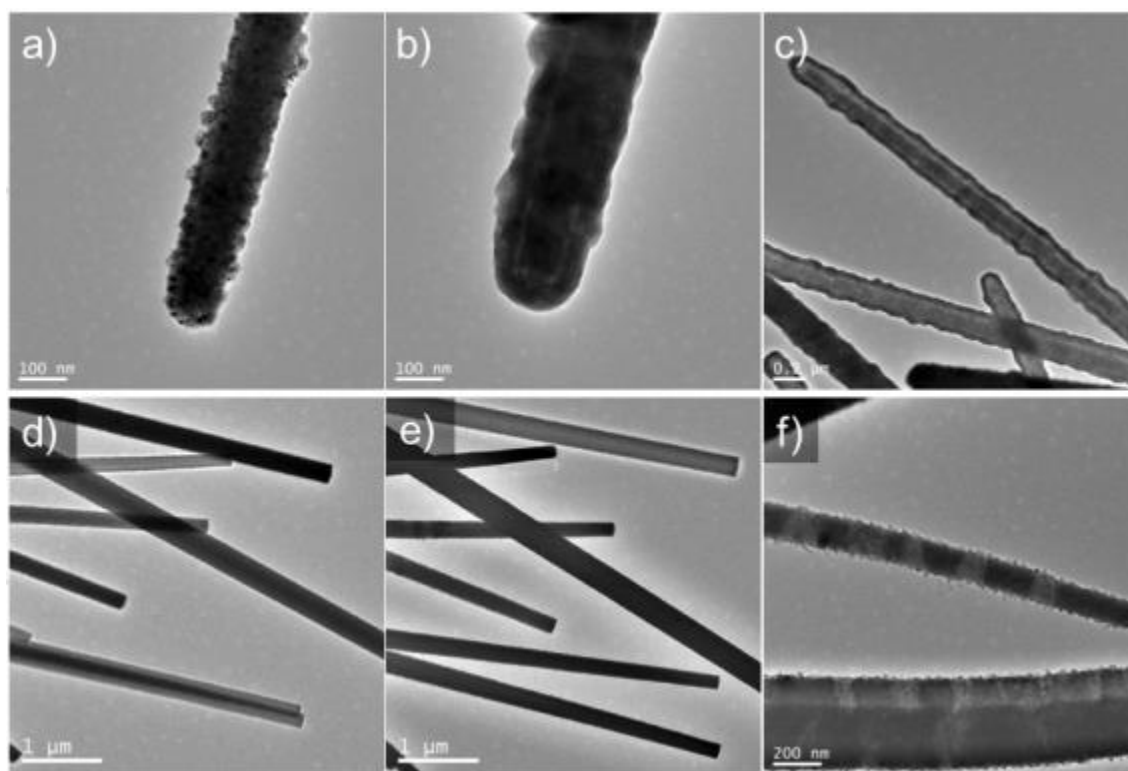


Figure 4.4 The suppression of diffusion-driven reactions by the e-beam effect. (a)-(c): Fe- Cu_2S ; (d)-(f): Zn- Cu_2S . (a) Fe-coated NW imaged before heating, and (b) the same structure imaged after typical thermal treatment. (c) Nearby structures on the same sample preparation, which hadn't been irradiated by e-beam before, show the RIT morphology. (d) Zn-coated NWs before and (e) after typical heat treatment, where e-beam exposure suppressed Zn incorporation, and (f) nearby NW that did exhibit the Zn incorporation.

Similarly, for Cu_2S NWs separated from the Cu substrate before heating, the RIT morphology in the resulting materials was less pronounced, and the structures showed significant Cu out-diffusion from the exposed end (Figure 4.5a). It seems that the Cu substrate serves as a reservoir to receive excess Cu^+ ions or to replace Cu^+ deficiencies in the Cu_2S NWs,¹⁷ and therefore the disconnection of Cu_2S NWs from the substrate disrupts Cu^+ diffusion.

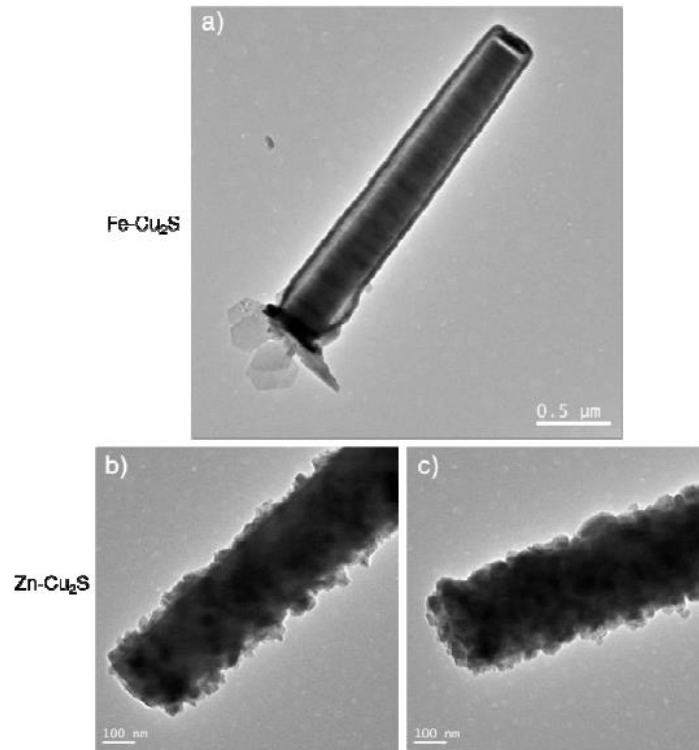


Figure 4.5 Metal-coated Cu₂S NWs heated after being scraped from the Cu substrate. (a) Fe-coated NW result. (b) Zn-Cu₂S before and (c) after typical heat treatment, showing no noticeable incorporation of Zn.

Lastly, an interlayer of Al₂O₃, deposited on the NWs before the Fe layer deposition, was added to disrupt diffusion between the NW and its coating (Figure 4.6). The resulting tubes exhibited a relative concentration of Cu notably lower than that from tubes of typical RITs, along with a diminished expansion and separation from the core NW. Again we concluded that Cu⁺ diffusion is important to the RIT formation.

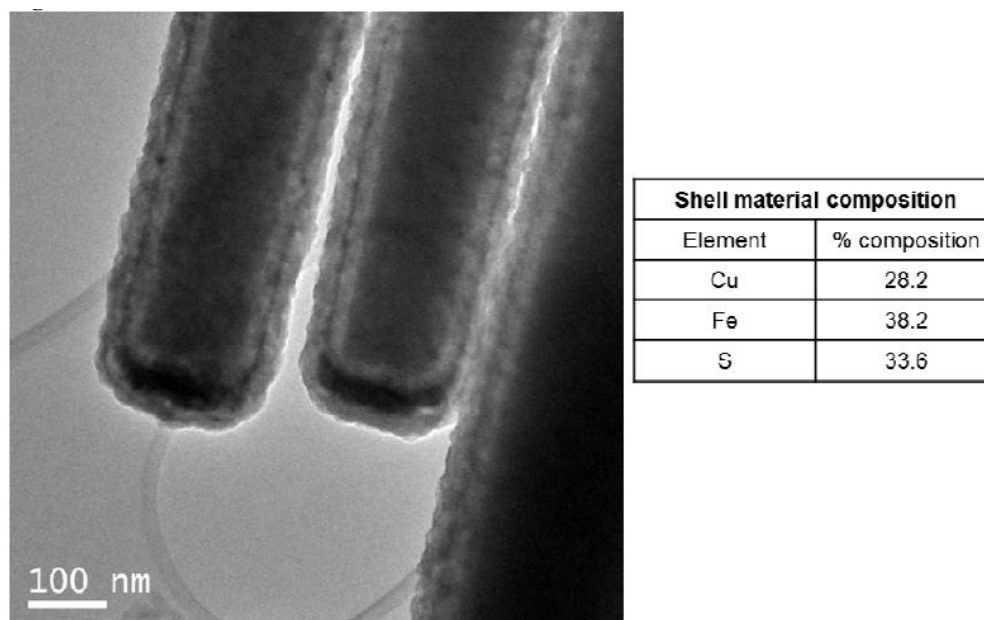


Figure 4.6 The result of heating Fe-coated NWs with the presence of an ALD-deposited Al_2O_3 layer beneath the Fe. The composition reflects a significantly inhibited out-diffusion of Cu.

Statistical studies of the diameters of the starting Cu_2S NWs and the resulting rods and tubes were performed, and it was found that the diameters of the encapsulated rods were not significantly different from those of the original NWs (Figure 4.7). This suggests that the sublattice of the Cu_2S NW is stable during the reaction. Because the inward diffusing Fe is insufficient to replenish the vacancies left by the outward diffusing Cu^+ (per elemental analysis), to maintain electroneutrality it seems cations must be drawn from the underlying Cu substrate.

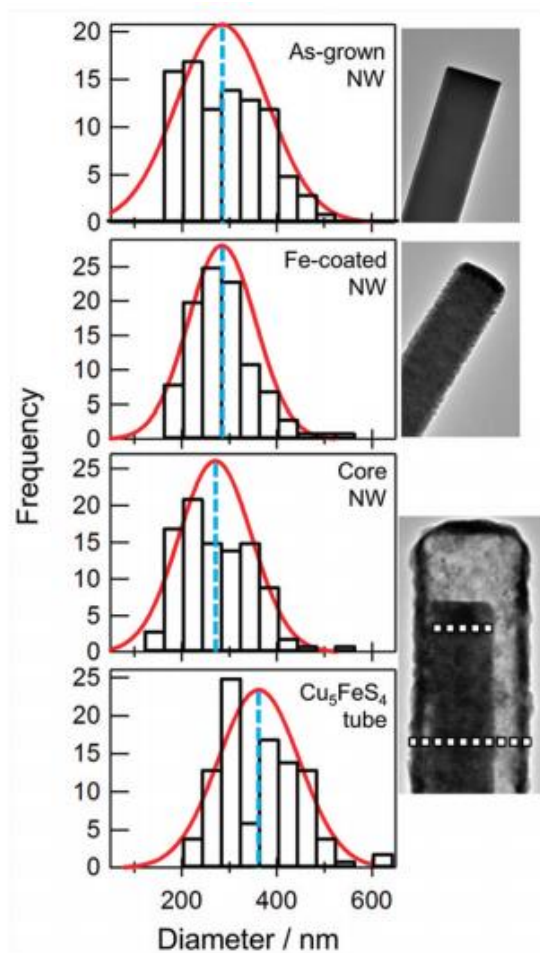


Figure 4.7 Statistical diameter measurements of the RIT formation process. Shown are 100 measurements each of as-grown, as-coated, core NW, and tube morphologies, with a Gaussian fit (red curve) and average (blue line) for each. Reprinted with permission from ref. ², © 2011 American Chemical Society.

Lastly, no RITs were observed on other NWs (Si or ZnO NWs) coated by Fe, supporting the unique reactivity of Cu_2S NWs. From this we infer that the RIT formation is not simply the result of the sulfidation of Fe. All together, the observations suggest that a continuous supply of Cu from the substrate is critical to the RIT formation, differing the structures from the common zero-dimensional analogues known as “rattle” or “yolk-shell” nanostructures, or nanotubes formed from core/shell nanowires, both of which generally form via a normal Kirkendall process in which the core material is consumed and diminished during the reaction process.⁷

Although the solid-state formation of hollow inorganic structures derived from the reaction of core/shell starting materials by the Kirkendall effect has been previously reported,^{7,13,27-28} the temperature of the present reaction makes this approach unique. This low-temperature reaction is likely enabled by the high diffusivity of Cu^+ in Cu_2S and other materials. The process temperature (105 °C) coincides with the Cu_2S phase transition from monoclinic to hexagonal (low- to high-chalcocite), with the hexagonal phase known to exhibit greater Cu mobility.²⁹⁻³¹ Indeed, TEM and ED observations suggest that a phase transition may play a role in activating this reaction (Figure 4.2), although the nature of the transition is difficult to observe in situ. We also found that H_2S also plays a critical role in the transformation, as control experiments where the Fe-coated Cu_2S NWs were heated at 105 °C without H_2S produced no significant morphology changes. While more research is needed to fully understand the role of H_2S , it is believed to serve at least two purposes. First, it reacts with Fe to create ionic vacancies in the Fe-shell to drive Cu^+ outward diffusion. Second, continuous reaction between H_2S and the Cu-incorporated Fe-shell leads to the shell expansion and its subsequent disconnection from the NW template. The decomposition of H_2S likely drives further oxidation of multivalent Fe ions to maintain electroneutrality once the Cu^+ diffusion pathway is broken. Afterward, the shell continues to expand until a thermodynamically stable phase of the Cu–Fe–S system is formed (bornite).

Notwithstanding the fact that ionic exchange reactions at similarly low temperatures in solutions have been reported,¹⁵⁻¹⁶ where the exchange is driven by ionic solubility effects, reports of low-temperature, solid-state, diffusion-driven reactions in solvent-free systems are rare.³²⁻³⁴ Thus, the present results are new and interesting, demonstrating the potential of using Cu_2S NWs as both physical templates and chemical sources to generate high-quality, closed-end, hollow tubes.

4.2 Zn–Cu₂S System

To further explore the solid-state reactions enabled by Cu⁺ diffusion at low-temperatures, we next examined a system where inward ion diffusion was more significant. For this experiment, we used Cu₂S NWs coated with Zn since Zn²⁺ is of similar size to Cu⁺ and has been observed to exhibit appreciable diffusivity within a sulfide sublattice.³⁵⁻³⁶ The Zn–Cu₂S system is also interesting because the reactions could yield new synthetic routes to complex chalcogenides for energy conversion applications, such as the promising solar absorber Cu₂ZnSnS₄ (CZTS).³⁷⁻³⁸ The result was found to be distinctly different from the Fe–Cu₂S system.

As shown in Figure 4.8, a segmented morphology was obtained when Zn-coated Cu₂S NWs were heated at 105 °C for 30 min in H₂S. The dark segments in the bright-field TEM images (Figure 4.8a,b) were identified as Cu₂S, and the gray segments as ZnS, from an EDS line scan (Figure 4.8d). When imaged in bright-field TEM mode, the ZnS segments appeared bright and more obvious due to their high crystallinity (Figure 4.8c). An electron diffraction pattern obtained from a ZnS segment could be indexed to the wurtzite phase (Figure 4.8e, inset; Figure 4.9). The images and the EDS data showed that the interfaces between the ZnS and Cu₂S segments were abrupt. Interestingly, statistical analysis found that the average diameters of the ZnS segments matched well with the original Cu₂S NW diameters, whereas those of the Cu₂S segments had increased measurably (Figure 4.10). We understand the reaction mechanism as follows.

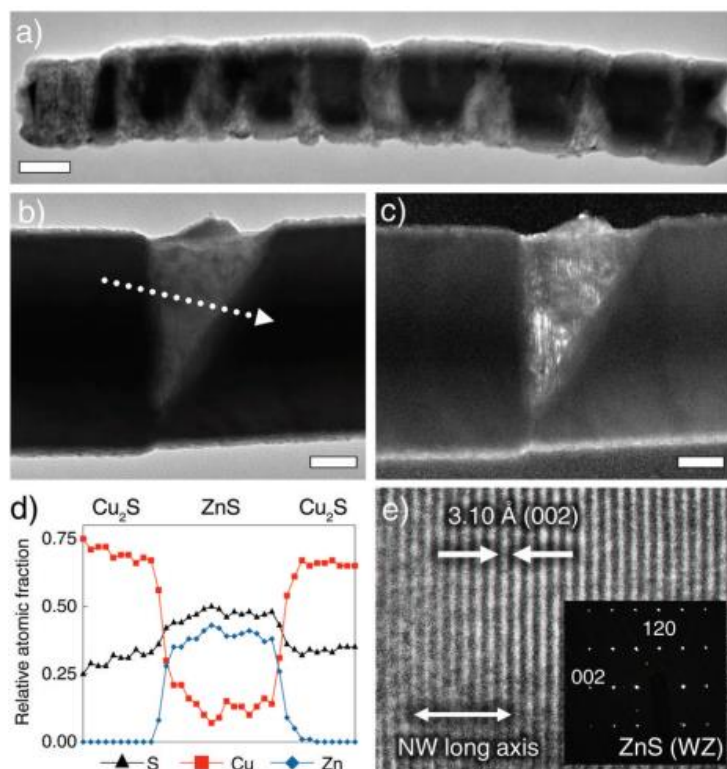


Figure 4.8 Solid-state reaction of Zn-coated Cu₂S NWs. (a) TEM image showing the segmented incorporation of Zn into the NWs (scale bar: 100 nm). Detailed bright-field (b) and dark-field (c) images show the abrupt interfaces between segments and the high degree of crystallinity in the ZnS regions (scale bars: 50 nm). (d) EDS line scan (path shown as dotted arrow in b) showing the Cu₂S and ZnS compositions and abrupt nature of the transition. Note that the analysis of composition by EDS is not strictly quantitative, especially for light elements such as S. (e) A high-resolution image of the ZnS region shows lattice-resolved spacing along the NW long axis attributable to the wurtzite phase, as confirmed by the ED pattern (inset). Reprinted with permission from ref. ², © 2011 American Chemical Society.

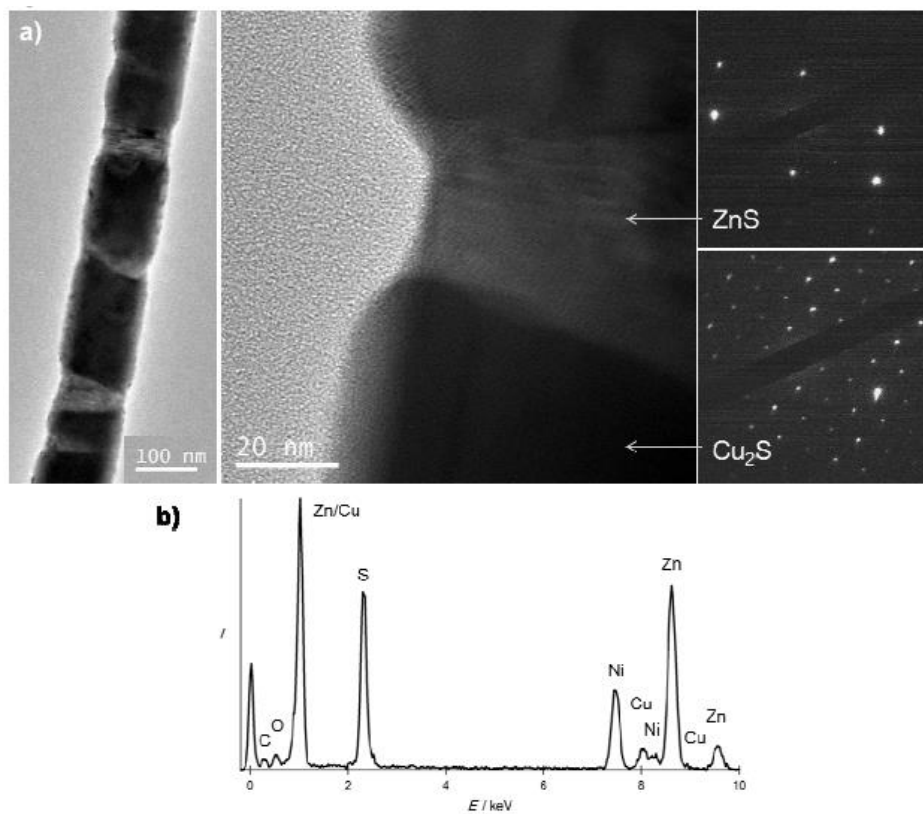


Figure 4.9 (a) TEM images with electron diffraction patterns of the different regions in a Zn-Cu₂S NW product. (b) EDS spectrum of the Zn-rich segment.

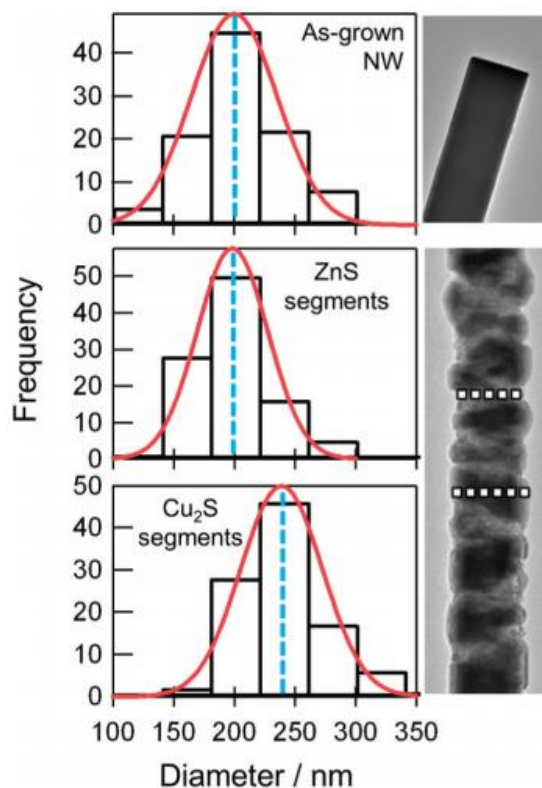


Figure 4.10 Statistical diameter measurements of the segmented incorporation process for ZnS/Cu₂S heterostructures. Shown are 100 measurements each of as-grown NWs, dark Cu₂S segments, and incorporated ZnS segments, with a Gaussian fit (red curve) and average (dotted blue line) for each. Reprinted with permission from ref. ², © 2011 American Chemical Society.

H₂S can cause oxidation of the deposited Zn to produce Zn²⁺ ions, which are mobile and can diffuse into the sulfide sublattice. In a mechanism analogous to phase segregation, this diffusion process drives Cu⁺ out in a given segment to concentrate in the adjacent areas, driven by the formation of stable ZnS. The concentrated Cu⁺ subsequently reacts with H₂S to form new Cu₂S, increasing the diameters of the Cu-rich segments. The proposed mechanism, schematically depicted in Figure 4.11, is supported by the following observations.

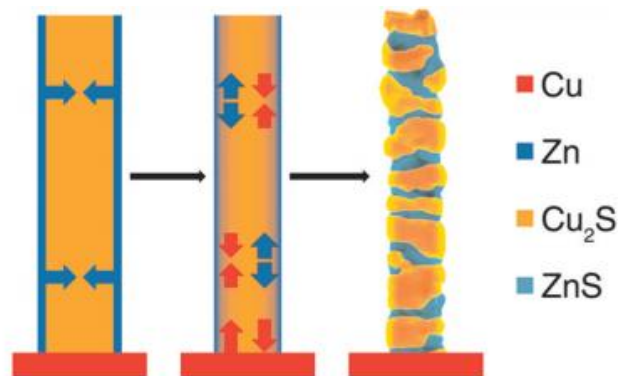


Figure 4.11 Schematic representation depicting the ionic diffusion toward the formation of segmented ZnS/Cu₂S heterostructured NWs. Zn inward diffusion prompts Cu diffusion to either the NW surface or back into the Cu substrate. Reprinted with permission from ref. ², © 2011 American Chemical Society.

Just as in the Fe–Cu₂S system, significantly less pronounced conversion was observed when the Cu⁺ diffusion was disturbed by e-beam irradiation or the removal of the underlying Cu substrate (Figure 4.4d–f; Figure 4.5b and c). Distinct from the Fe–Cu₂S system, however, the presence of H₂S was not found to play an essential role in the conversion process, although its presence did lead to smoother NW surfaces (Figure 4.12). This phenomenon can be explained by the diffusion of ions. Because the reaction with H₂S is not a prerequisite for the Zn²⁺ and Cu⁺ diffusion, the segregation can take place with or without H₂S present. In the absence of H₂S, the excess Cu concentrates on the surface of the Cu-rich segments to yield rough morphologies. When H₂S is present, reactions between Cu and H₂S can result in smooth surfaces and increased diameters of the Cu-rich segments. The fact that H₂S is not critical for the reactions with Zn further suggests that Zn can be oxidized by Cu⁺. Indeed, the reaction $\text{Zn} + \text{Cu}_2\text{S} \rightarrow \text{Cu} + \text{ZnS}$ is exothermic ($\Delta_r H^\circ = -126.5 \text{ kJ/mol}$).

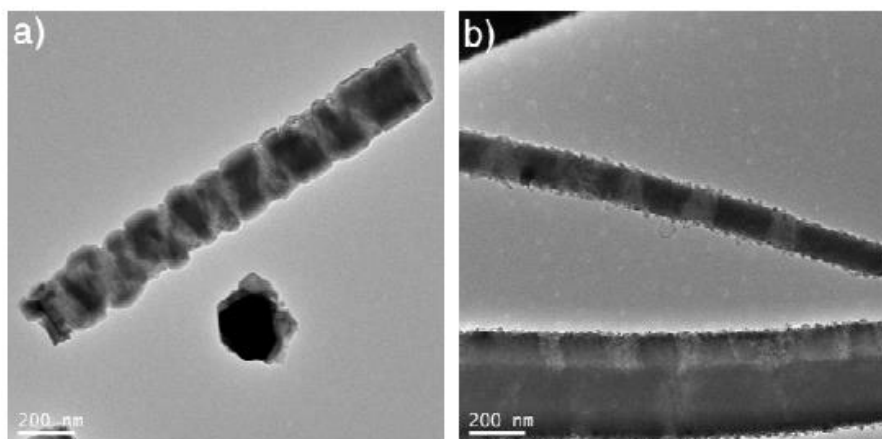


Figure 4.12 Segmented NWs resulting from heating Zn-Cu₂S NWs either (a) with or (b) without the presence of H₂S gas.

The segments did not seem to follow any strict arrangement patterns, although they were often relatively uniform in size along a given NW. In addition, we observed increased Zn incorporation when a thicker Zn film was initially deposited on the NWs. As such, the segmented NWs described above reflect a partial conversion which results from an insufficient supply of Zn. To test this interpretation, we increased the thickness of Zn as high as 90 nm and found that Cu₂S NWs could be entirely converted to ZnS. Figure 4.13 shows bright- and dark-field TEM images after reaction, in which the NW body has become predominantly ZnS in composition. While some Cu still remains, likely in the form of Cu₂S or Cu in the body or on the surface, the amount is far less than sufficient to account for the original Cu content in Cu₂S NW template. The only conceivable route through which the majority of the Cu “disappears” is to diffuse back to the Cu substrate. Such a hypothesis is possible because the attached Cu substrate may act as a reservoir for the outward diffusing cations. The dark-field image seems to show strain within the NW lattice, presumably due to the lattice mismatch between ZnS and Cu₂S. The particles on the surface are primarily excess Zn.

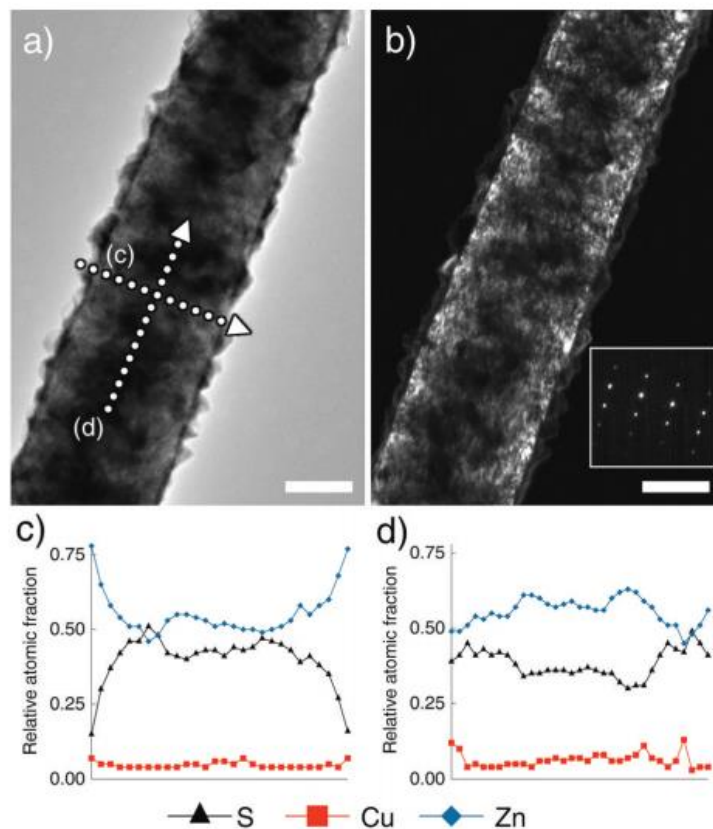


Figure 4.13 Full conversion from Cu_2S to ZnS NWs. (a) A bright-field TEM image shows the texture of excess Zn on the NW surface, while (b) a dark-field image reveals the intact crystallinity of the NW: (inset) ED pattern that can be indexed to wurtzite ZnS; scale bars: 100 nm. (c) Radial and (d) axial EDS line scans verify the lack of Cu and the presence of ZnS and excess Zn (paths labeled in a). Reprinted with permission from ref. ², © 2011 American Chemical Society.

The Zn– Cu_2S reaction resulted in morphologies very different from the RIT structures produced by the Fe– Cu_2S system, demonstrating the versatility of the solid-state process and how it depends on the species involved. The resulting segmented NWs suggest a straightforward reaction process for achieving compositionally modulated NWs which could be shown to demonstrate unique opto- or thermo-electronic properties. In addition, the full conversion from Cu_2S to ZnS NWs suggests a method for achieving, through solid-state conversion reactions, NWs of various targeted compositions.

4.3 Materials Considerations

In both systems studied here, the solid-state reactions relied on two key characteristics of the Cu₂S NW arrays: (i) significant ion diffusivity at low temperatures and (ii) an interface between Cu₂S and its Cu substrate across which mass transfer occurs. While Cu₂S is known to be an ion-diffusive material, it is possible that other chemical systems, even some not conventionally known to exhibit high ionic diffusivities, could behave similarly in solid-state reactions. In support of this, consider the variety of compounds on which solution-based low-temperature exchange reactivity has been demonstrated, which includes a large number of metal chalcogenides and oxides.^{6,15-16,39-40} Similar to the results of those studies, the increased reactivity exhibited by nanoscale materials may allow solid-state reactions via mechanisms similar to what we present here.

The diffusivity of Cu⁺ in the S sublattice renders the Cu₂S system highly unique, and the reactivities of the Fe–Cu₂S and Zn–Cu₂S systems provide additional evidence to support our previously proposed cation-vacancy-diffusion model for the Cu₂S NW growth. The existence of ionic diffusion pathways between the NWs and the substrate from which they are grown is equally unique. We show here that these channels may be utilized to provide additional Cu⁺ (in the case of Fe–Cu₂S reactions) or to store excess Cu⁺ (in the case of Zn–Cu₂S reactions). More interestingly, due to differences in diffusion characteristics, distinctly different morphologies (i.e., RIT and segmented NWs) can be obtained. Notably, the RIT morphology is observed for the first time. These structures could prove useful in various applications; the high surface area and inner voids of the RITs may be beneficial in catalysis or sensing applications, and the segmented heterostructures may exhibit interesting optoelectronic and thermoelectric properties. More generally, we envision that the high diffusivity of Cu⁺ in a S sublattice can be further exploited for a number of important applications, including converting Cu₂S NWs into other useful

compositions (such as CTZS and FeS₂ for solar energy harvesting), or for storing ions with small radii as a means of energy storage (e.g. rechargeable batteries). The low temperatures at which these solid-state reactions can occur distinguishes this system from others, possibly opening up a new pathway for nanomaterials synthesis by conversion reactions.

4.4 Outlook for Cu₂S-based photovoltaics

In the previous three chapters, we noted that the high ionic diffusivity in Cu₂S has interesting and beneficial implications, but can also prove to be a culprit in the instability that has long plagued Cu₂S as a photovoltaic material. The studies presented here serve to reinforce the presumption that Cu diffusion in Cu₂S can occur at low temperatures and influence its electronic properties. This must be taken into account in efforts to use Cu₂S in electronic applications. It may prove worthwhile to explore methods of arresting or inhibiting this diffusion, and success toward this goal could lead to a renewed interest in Cu₂S, a material which has the desired abundance and band gap characteristics for use in photovoltaic devices. Meanwhile, several related chalcogenide materials have emerged as promising candidates in solar cells, including CuInGaS₂,⁴¹⁻⁴² CuSCN,⁴³ and CZTS,^{38,44} showing that sulfide-based materials remain interesting, and Cu₂S may yet provide an interesting approach if suitable conversion reactions can be designed.

4.5 References

- 1 Okada, K.; Hattori, A.; Kameshima, Y.; Yasumori, A.; Das, R. N. Effect of monovalent cation additives on the gamma-Al₂O₃-to-alpha-Al₂O₃ phase transition. *J. Am. Ceram. Soc.* **2000**, *83*, 1233-1236.
- 2 Mayer, M. T.; Simpson, Z. I.; Zhou, S.; Wang, D. Ionic-Diffusion-Driven, Low-Temperature, Solid-State Reactions Observed on Copper Sulfide Nanowires. *Chem. Mater.* **2011**, *23*, 5045-5051.
- 3 West, A. R.: *Solid State Chemistry and its Applications*; John Wiley & Sons: New York, 1987.
- 4 Fan, H.-M.; Yi, J.-B.; Yang, Y.; Kho, K.-W.; Tan, H.-R.; Shen, Z.-X.; Ding, J.; Sun, X.-W.; Olivo, M. C.; Feng, Y.-P. Single-Crystalline MFe₂O₄ Nanotubes/Nanorings

- Synthesized by Thermal Transformation Process for Biological Applications. *ACS Nano* **2009**, *3*, 2798-2808.
- 5 Liu, B.; Bando, Y.; Jiang, X.; Li, C.; Fang, X.; Zeng, H.; Terao, T.; Tang, C.; Mitome, M.; Golberg, D. Self-assembled ZnS nanowire arrays: synthesis, in situ Cu doping and field emission. *Nanotechnology* **2010**, *21*.
- 6 Vasquez, Y.; Henkes, A. E.; Bauer, J. C.; Schaak, R. E. Nanocrystal conversion chemistry: A unified and materials-general strategy for the template-based synthesis of nanocrystalline solids. *J. Sol. St. Chem.* **2008**, *181*, 1509-1523.
- 7 Fan, H. J.; Goesele, U.; Zacharias, M. Formation of nanotubes and hollow nanoparticles based on Kirkendall and diffusion processes: A review. *Small* **2007**, *3*, 1660-1671.
- 8 Fan, H. J.; Knez, M.; Scholz, R.; Nielsch, K.; Pippel, E.; Hesse, D.; Zacharias, M.; Goesele, U. Monocrystalline spinel nanotube fabrication based on the Kirkendall effect. *Nat. Mater.* **2006**, *5*, 627-631.
- 9 Wu, Y.; Xiang, J.; Yang, C.; Lu, W.; Lieber, C. M. Single-crystal metallic nanowires and metal/semiconductor nanowire heterostructures. *Nature* **2004**, *430*, 61-65.
- 10 Zhou, J.; Liu, J.; Wang, X.; Song, J.; Tummala, R.; Xu, N. S.; Wang, Z. L. Vertically aligned Zn₂SiO₄ nanotube/ZnO nanowire heterojunction arrays. *Small* **2007**, *3*, 622-626.
- 11 Trentler, T. J.; Iyer, R. S.; Sastry, S. M. L.; Buhro, W. E. Preparation of nanocrystalline molybdenum disilicide (MoSi₂) by a chlorine-transfer reaction. *Chem. Mater.* **2001**, *13*, 3962-3968.
- 12 Li, Y. J.; Lu, M. Y.; Wang, C. W.; Li, K. M.; Chen, L. J. ZnGa₂O₄ nanotubes with sharp cathodoluminescence peak. *Appl. Phys. Lett.* **2006**, *88*.
- 13 Raidongia, K.; Rao, C. N. R. Study of the transformations of elemental nanowires to nanotubes of metal oxides and chalcogenides through the Kirkendall effect. *J. Phys. Chem. C* **2008**, *112*, 13366-13371.
- 14 Sines, I. T.; Schaak, R. E. Phase-Selective Chemical Extraction of Selenium and Sulfur from Nanoscale Metal Chalcogenides: A General Strategy for Synthesis, Purification, and Phase Targeting. *J. Am. Chem. Soc.* **2011**, *133*, 1294-1297.
- 15 Luther, J. M.; Zheng, H.; Sadtler, B.; Alivisatos, A. P. Synthesis of PbS Nanorods and Other Ionic Nanocrystals of Complex Morphology by Sequential Cation Exchange Reactions. *J. Am. Chem. Soc.* **2009**, *131*, 16851-16857.
- 16 Sadtler, B.; Demchenko, D. O.; Zheng, H.; Hughes, S. M.; Merkle, M. G.; Dahmen, U.; Wang, L.-W.; Alivisatos, A. P. Selective Facet Reactivity during Cation Exchange in Cadmium Sulfide Nanorods. *J. Am. Chem. Soc.* **2009**, *131*, 5285-5293.
- 17 Liu, X.; Mayer, M. T.; Wang, D. Understanding Ionic Vacancy Diffusion Growth of Cuprous Sulfide Nanowires. *Angew. Chem. Int. Ed.* **2010**, *49*, 3165-3168.
- 18 Cassaignon, S.; Pauporte, T.; Guillemoles, J. F.; Vedel, J. Copper Diffusion in Copper Sulfide: a Systematic Study. *Ionics* **1998**, *4*, 364-371.
- 19 Larson, R. S. A physical and mathematical model for the atmospheric sulfidation of copper by hydrogen sulfide. *J. Electrochem. Soc.* **2002**, *149*, B40-B46.
- 20 Moitra, K.; Deb, S. Degradation of the performance of Cu₂S/CdS solar-cells due to a 2-way solid-state diffusion process. *Solar Cells* **1983**, *9*, 215-228.
- 21 Riha, S. C.; Johnson, D. C.; Prieto, A. L. Cu₂Se Nanoparticles with Tunable Electronic Properties Due to a Controlled Solid-State Phase Transition Driven by Copper Oxidation and Cationic Conduction. *J. Am. Chem. Soc.* **2011**, *133*, 1383-1390.
- 22 Sakamoto, T.; Sunamura, H.; Kawaura, H.; Hasegawa, T.; Nakayama, T.; Aono, M. Nanometer-scale switches using copper sulfide. *Appl. Phys. Lett.* **2003**, *82*, 3032-3034.

- 23 Tsuchiya, T.; Oyama, Y.; Miyoshi, S.; Yamaguchi, S. Nonstoichiometry-Induced Carrier Modification in Gapless Type Atomic Switch Device Using Cu₂S Mixed Conductor. *Appl. Phys. Exp.* **2009**, *2*, 055002.
- 24 Wadia, C.; Wu, Y.; Gul, S.; Volkman, S. K.; Guo, J.; Alivisatos, A. P. Surfactant-Assisted Hydrothermal Synthesis of Single phase Pyrite FeS₂ Nanocrystals. *Chem. Mater.* **2009**, *21*, 2568-2570.
- 25 Barkat, L.; Hamdadou, N.; Morsli, M.; Khelil, A.; Bernede, J. C. Growth and characterization of CuFeS₂ thin films. *J. Cryst. Growth* **2006**, *297*, 426-431.
- 26 Chen, J. H.; Harvey, W. W. Cation self-diffusion in chalcopyrite and pyrite. *Metall. Trans. B* **1975**, *6B*, 331-9.
- 27 Lee, Y.-I.; Goo, Y.-S.; Chang, C.-H.; Lee, K.-J.; Myung, N. V.; Choa, Y.-H. Tunable Synthesis of Cuprous and Cupric Oxide Nanotubes from Electrodeposited Copper Nanowires. *J. Nanosci. Nanotech.* **2011**, *11*, 1455-1458.
- 28 Li, Q. G.; Penner, R. M. Photoconductive cadmium sulfide hemicylindrical shell nanowire ensembles. *Nano Lett.* **2005**, *5*, 1720-1725.
- 29 Evans, H. T. copper coordination in low chalcocite and djurleite and other copper-rich sulfides. *Am. Mineral.* **1981**, *66*, 807-818.
- 30 Hirahara, E. The electrical conductivity and isothermal hall effect in cuprous sulfide, semi-conductor. *J. Phys. Soc. Jap.* **1951**, *6*, 428-437.
- 31 Leon, M.; Terao, N.; Rueda, F. Phase-transitions in cuprous sulfide evaporated thin-films. *J. Mat. Sci.* **1984**, *19*, 113-120.
- 32 Mokari, T.; Aharoni, A.; Popov, I.; Banin, U. Diffusion of gold into InAs nanocrystals. *Angew. Chem. Int. Ed.* **2006**, *45*, 8001-8005.
- 33 Wang, Q.; Li, J.-X.; Li, G.-D.; Cao, X.-J.; Wang, K.-J.; Chen, J.-S. Formation of CuS nanotube arrays from CuCl Nanorods through a gas-solid reaction route. *J. Cryst. Growth* **2007**, *299*, 386-392.
- 34 Zhang, B.; Jung, Y.; Chung, H.-S.; Van Vugt, L.; Agarwal, R. Nanowire Transformation by Size-Dependent Cation Exchange Reactions. *Nano Lett.* **2010**, *10*, 149-155.
- 35 Burton, L. C.; Uppal, P. N.; Dwight, D. W. Cross diffusion of Cd and Zn into Cu₂S formed on Zn_xCd_{1-x}S thin-films. *J. Appl. Phys.* **1982**, *53*, 1538-1542.
- 36 Cherniak, D. J. Diffusion in Carbonates, Fluorite, Sulfide Minerals, and Diamond. In *Diffusion in Minerals and Melts*; Zhang, Y. X., Cherniak, D. J., Eds., 2010; Vol. 72; pp 871-897.
- 37 Katagiri, H.; Jimbo, K.; Maw, W. S.; Oishi, K.; Yamazaki, M.; Araki, H.; Takeuchi, A. Development of CZTS-based thin film solar cells. *Thin Solid Films* **2009**, *517*, 2455-2460.
- 38 Todorov, T. K.; Reuter, K. B.; Mitzi, D. B. High-Efficiency Solar Cell with Earth-Abundant Liquid-Processed Absorber. *Adv. Mater.* **2010**, *22*, E156-+.
- 39 Camargo, P. H. C.; Lee, Y. H.; Jeong, U.; Zou, Z.; Xia, Y. Cation exchange: A simple and versatile route to inorganic colloidal spheres with the same size but different compositions and properties. *Langmuir* **2007**, *23*, 2985-2992.
- 40 Jeong, U.; Camargo, P. H. C.; Lee, Y. H.; Xia, Y. Chemical transformation: a powerful route to metal chalcogenide nanowires. *J. Mat. Chem.* **2006**, *16*, 3893-3897.
- 41 Contreras, M. A.; Egaas, B.; Ramanathan, K.; Hiltner, J.; Swartzlander, A.; Hasoon, F.; Noufi, R. Progress toward 20% efficiency in Cu(In,Ca)Se₂ polycrystalline thin-film solar cells. *Prog. Photovolt.* **1999**, *7*, 311-316.
- 42 Kapur, V. K.; Bansal, A.; Le, P.; Asensio, O. I. Non-vacuum processing of CuIn_{1-x}Ga_xSe₂ solar cells on rigid and flexible substrates using nanoparticle precursor inks. *Thin Solid Films* **2003**, *431*, 53-57.

- 43 Levy-Clement, C.; Tena-Zaera, R.; Ryan, M. A.; Katty, A.; Hodes, G. CdSe-Sensitized p-CuSCN/nanowire n-ZnO heterojunctions. *Adv. Mater.* **2005**, *17*, 1512-1515.
- 44 Xin, X. K.; He, M.; Han, W.; Jung, J. H.; Lin, Z. Q. Low-Cost Copper Zinc Tin Sulfide Counter Electrodes for High-Efficiency Dye-Sensitized Solar Cells. *Angew. Chem. Int. Ed.* **2011**, *50*, 11739-11742.

Chapter 5

Photoelectrochemical water splitting

As introduced in Section 1.3, photoelectrochemical (PEC) methods of sunlight harvesting seek to convert the energy from solar photons into energy stored in chemical bonds. In particular, the most widely desired PEC reaction is the splitting of water to yield O₂ and H₂. Molecular hydrogen (H₂) has great promise for use as an energy carrier, given that its energy density per unit mass is high and the energy can be released (by combustion or by electrochemical reaction in a fuel cell) without harmful emissions common to other fuels such as gasoline. A chemical energy carrier like H₂ offers a potential solution to the storage and transport problems associated with solar energy.

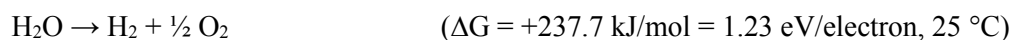
Photoelectrochemical reactions to drive the synthesis of desired chemical species can be called “artificial photosynthesis”. While there are a variety of approaches to artificial photosynthesis,¹⁻⁵ methods based on semiconductor materials have shown great promise, for reasons introduced in Section 1.2 and 1.3. The search for suitable photoactive semiconductors to drive PEC water splitting has been a long-term effort, complicated by the requirements for several key properties:

- a) energy band structure suitable to drive electrolysis reactions
- b) chemical stability in aqueous solutions of a wide pH range
- c) stability against photo-corrosion
- d) material abundance, low-cost synthesis

Requirement (a) derives from the fact that complete water electrolysis comprises two redox reactions at different energies, so a PEC device needs to generate sufficient photovoltage to

account for the energy difference. This will be discussed in detail throughout this chapter. Requirement (b) is necessary since the basis of a PEC cell is the direct contact between a semiconductor and a liquid, and electrolysis of water is most efficient when performed at non-neutral pH conditions; (c) states that the materials must be stable under illumination. Requirement (d) has a particular significance for our research, for regardless of the scientific advances made on a given material system, its global impact will be dependent on whether it can be produced in sufficient volumes, and at competitively low costs, to make a significant dent in our massive energy demands.

Turning our attention to the specifics of the desired reaction, we look at the process of water electrolysis as driven by illuminated semiconductor electrodes. To split water, this general reaction applies:



This endothermic reaction as written is a two electron process. The Gibbs free energy of the reaction defines the thermodynamic minimum energy needed to drive the reaction (1.23 eV), which correlates with photons of wavelength ~ 1000 nm. This suggests that a large portion of the solar spectrum photons should be capable of driving water splitting, but in reality there are several factors that increase the actual energetic demand of the reaction to approximately 1.6–2.4 eV,⁶⁻⁷ including overpotentials resulting from concentration and kinetic factors. Adding the fact that the photovoltage produced on a semiconductor can never reach as high as the band gap potential,⁸ we can see that PEC water splitting on a single material would require a band gap significantly larger than that identified as optimal for photovoltaic applications (~ 1.3 eV, see Section 1.3). Indeed, this is a major reason that the approach of simply coupling a solar cell to an electrolyzer is not as desirable as direct PEC water splitting. The fact that most PV systems are

designed for optimal *efficiency*, as defined by the total power output of the cell, means that commercially-available solar cells typically produce voltages insufficient to drive electrolysis.⁹ Therefore, multiple PV cells in tandem would be required, which would be undesirable. Coupling PEC and PV cells with complimentary spectral responses in tandem, however, has shown promise.¹⁰⁻¹³ This is related to the dual-absorber approach which will be discussed in Chapter 7.¹⁴

It is worthwhile to begin the discussion with the fundamentally simpler system, a single-semiconductor device aimed at PEC water splitting. The goal is to use solar photon absorption to generate a potential difference of sufficient energy to drive both reactions of electrolysis:



where e^- is an electron and h^+ is a hole, a positively-charged conceptual analogue to an electron commonly used in describing semiconductor processes. Electrons and holes will be referred to as charge carriers or charges. To further the discussion begun in Section 1.2, light absorption by a semiconductor entails a photon (of energy equal to or greater than the band gap energy) transferring its energy to a valence band electron, resulting in the promotion of the electron into the conduction band. Left behind in the valence band is a hole (a lack of an electron within the valence band) which carries a positive charge. For PEC purposes, holes are considered oxidizing equivalents while electrons are reducing equivalents. The electron-hole pair generated by photon absorption creates these red-ox equivalents of different energies that define the photoelectrochemical driving force. The reducing or oxidizing potential of the charge carriers is defined by their chemical potential; an electron with a greater chemical potential (more negative on the electrochemical scale) has greater reducing power, while a hole with a lower potential (more positive) has greater oxidizing power. This concept in combination with the energetics of

the electrolysis reactions above define the desired band energetics for a PEC semiconductor, as described next.

To drive unassisted (no externally-applied voltage) water splitting, the semiconductor needs to generate photoexcited electrons and holes of sufficient energy difference, on the order of 1.6–2.4 eV as described previously, and separate them to produce a photovoltage. The absolute positions of the band energies are crucial, as well. An ideal semiconductor would therefore have band positions *straddling* the reduction and oxidation potential energies of water splitting, as shown in Figure 5.1.

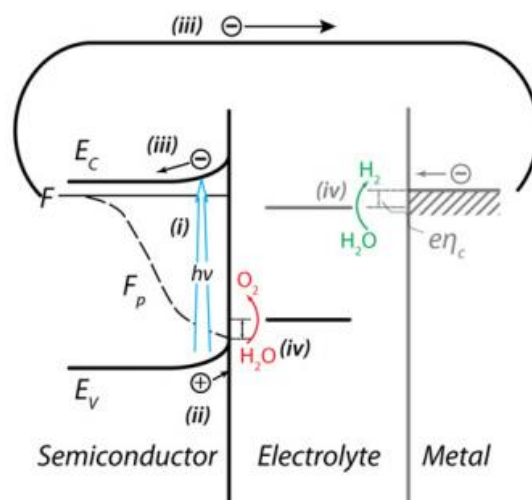


Figure 5.1 Band schematic of idealized n-type semiconductor for water splitting under illumination. The vertical dimension is a chemical potential scale. Processes depicted are (i) light absorption, (ii) interfacial charge transfer, (iii) charge transport, and (iv) chemical reactions at the surface. Reprinted with permission from ref. 15, © 2011 Elsevier.

The figure depicts an n-type semiconductor, meaning the minority carriers are holes (shown as positive charges) and the electrode acts as a photoanode. Under illumination, photogenerated holes in the valence band (E_v) have the power to oxidize water and generate O_2 , while conduction band (E_c) electrons travel through an external circuit to the cathode (commonly a metal with high water reduction activity such as Pt) to reduce water and generate H_2 . The potential difference (i.e.

the electrochemical driving force) of the photogenerated charges is defined by their difference in Fermi energy (F : bulk Fermi energy, \sim majority carrier Fermi energy; F_p : Fermi energy of holes, the minority carrier).

Semiconductor *photoanodes* as depicted in Figure 5.1 represent much of the research performed to date on water splitting electrodes, and will be the focus of this chapter. Nevertheless, research on photocathodes remains important,¹⁶ and a promising device construction features a back-to-back configuration of anode and cathode working in tandem to split water.⁶ Indeed, one of the intriguing aspects of PEC research is the fact that anodes and cathodes can be studied separately, which is important because of the significant differences between the two reactions of interest. We have chosen to study photoanodes primarily because the water oxidation reaction is comparatively more difficult and it seems to be the limiting process for PEC water splitting at present. There are several electrocatalytic materials (notably Pt) which can drive water reduction to H_2 with little overpotential; such materials for O_2 evolution have not been discovered. Whereas H_2 evolution requires two electrons per molecule of gas produced, the oxidation of water is a more complex process involving four electrons and two water molecules per O_2 molecule.

One may ask, given that the generation of H_2 is the ultimate goal, why the oxidation of water is given so much attention. Conceivably, other oxidation reactions could be substituted to balance the overall reaction, including oxidation of sacrificial electron donors (hole acceptors; commonly used to probe the intrinsic performance limits of photoelectrode devices) or some natural waste product which would be desirable to oxidize (e.g., urea from wastewater).¹⁷ Oxidation of water remains desirable, however, since it does not require the addition of sacrificial reagents (the supply of which would further complicate the scalability of H_2 -generating systems) and does not produce undesired byproducts (e.g. CO_2 upon oxidation of urea). Therefore electrolysis of water

offers the cleanest and simplest system, with the input being water and sunlight and the output being only H₂ and O₂ (depending on the configuration, additional electrolyte may also be necessary).

With the goal of developing a semiconductor photoanode that is highly active for water oxidation, we must start by considering the requirements we have identified thus far, including abundance, stability, and band energy characteristics. Upon examining the band energetics of several candidates, such as those depicted in Figure 5.2, we can narrow the search. Appealing as photoanodes are the transition metal oxides which have rather deep valence bands and larger band gaps, and are subsequently more stable in water than the more narrow-band gap options. Indeed, several candidates have been observed with band edges that straddle the reactions of electrolysis, namely ZnO and TiO₂ in Figure 5.2. As such they should be able to drive complete water splitting upon illumination, and this was demonstrated in the seminal work on TiO₂ by Fujishima and Honda.¹⁸

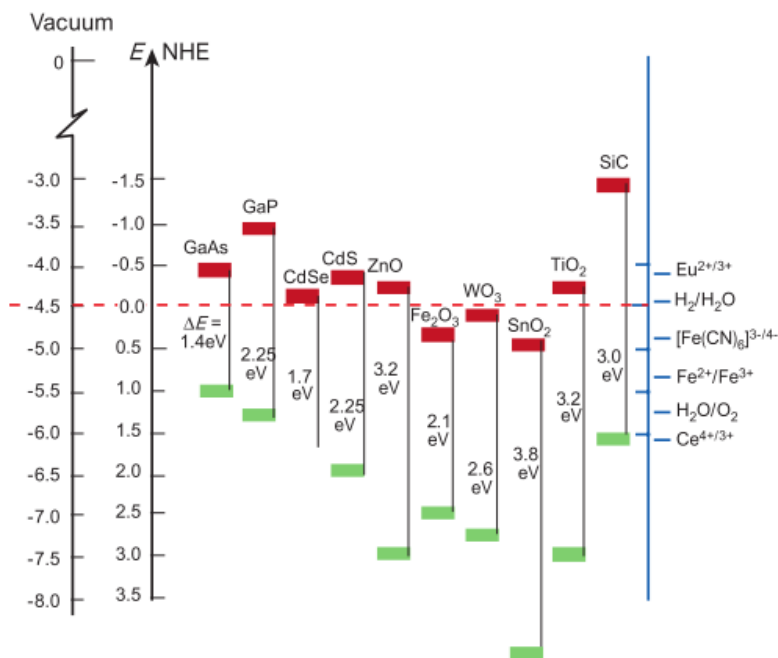


Figure 5.2 Band positions of several semiconductors. In red are the lower edges of the conduction bands, in green are the upper edges of the valence bands, and also shown are the band gap energies separating the edges. The dotted line represents the normal hydrogen electrode. Reprinted by permission from Macmillan Publishers Ltd: ref. 19 © 2001.

However, recalling the band gap dependence of photon absorption explained in Section 1.2, semiconductors with band gaps this large can only absorb a small fraction of the solar spectrum ($\lambda < 400$ nm for TiO_2), and can therefore only produce tiny photocurrents and thus small rates of H_2 production. Conversely, metal oxides with smaller band gaps, while offering broader spectral absorption, have conduction band edges which are too positive to drive the water reduction reaction (see Fe_2O_3 , WO_3). In this case, an externally applied voltage is necessary to promote the electrons to energies high enough for H_2 production.

A key aspect of semiconductor photoelectrochemistry, which must be introduced into the discussion at this time, is the significance of the semiconductor–liquid junction. In PEC devices, it is the equilibrium between chemical potentials of the solid and the electrolyte which result in an electric field at the surface. As shown in Figure 5.3 for an n-type semiconductor, contact between

the two phases induces charge transfer to make the chemical potential (Fermi energy, E_f) uniform across the system. Thus, the n-type semiconductor gives electrons to the redox system in solution until this equilibrium is satisfied. The result is the depletion of negative charges (majority carriers) near the surface of the semiconductor, resulting in an apparent upward bending of the valence and conduction bands at a depth defined as W (depletion width) and a height defined by the original difference in chemical potentials (E_f vs. $-qE(A/A^{\cdot})$), as shown in Figure 5.3b.

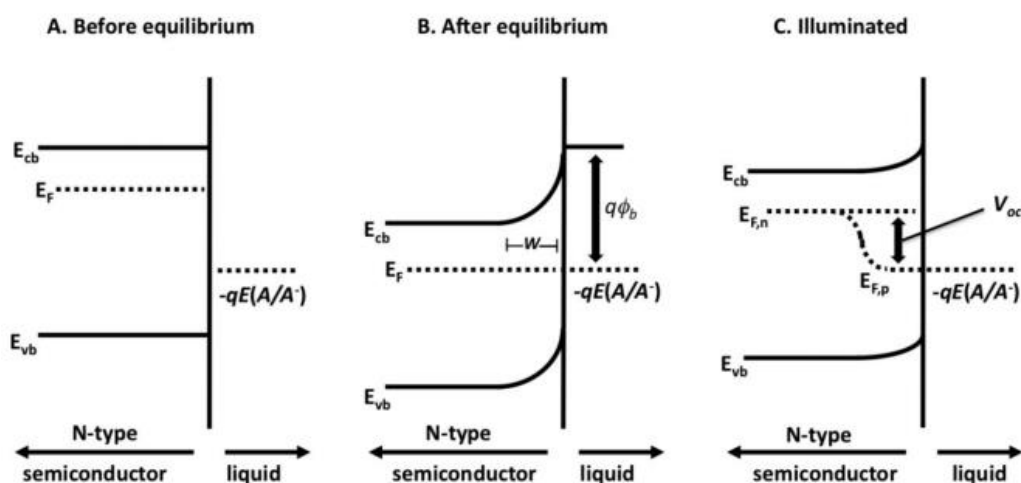


Figure 5.3 Energy band diagram of an n-type semiconductor and solution redox couple (A/A^{\cdot}). Adapted with permission from ref. 6, © 2010 American Chemical Society.

The importance of this band bending is that it represents an electric field which drives the separation of photoexcited electrons and holes. Photogenerated conduction band electrons tend to move “downhill” to lower electronic potentials, and as such will be swept away from the depletion region into the bulk of the material, as shown in Figure 5.1. Conversely, valence band holes will “float” upwards as electrons fall into their empty state. Holes are thereby driven toward the solid–liquid junction where they can partake in the oxidation of solution species. The degree of this charge separation represents the photovoltage generated in the semiconductor that can be used to drive useful work, i.e. the reduction and oxidation of water. If the photovoltage is insufficient to drive both, additional voltage must be applied before current can flow.

There are many more details of the semiconductor–electrolyte contact, some of which will be discussed in the following sections, and others which can be found in several useful reviews.^{6,19} The aim of our recent research, however, has been to show that the performance of a PEC system does not have to be limited by its depletion region-induced photovoltage (typically restricted by the intrinsic energetics of the solid–liquid system). Using unique yet rational approaches we can design PEC electrodes in which photovoltage can be generated more deeply within the semiconductor, to augment or supplement the surface voltage. In other words, we sought methods of getting larger photovoltages out of smaller band gap materials, thereby liberating us from the dilemma between band gap and voltage output. Chapter 6 and Chapter 7 will describe two different approaches we have demonstrated.

Our transition metal oxide of choice was Fe_2O_3 , a material that satisfies the requirements of abundance, stability, and good spectral response, but suffers from deficiencies in its energy band structure and subsequent PEC performance.

5.1 Hematite Fe_2O_3 as a promising candidate material

The hematite phase of iron (III) oxide (α Fe_2O_3) has attracted significant attention as a candidate photoanode material. Iron oxides are abundant (Fe is fourth and O is first when ranked by elemental abundance in Earth’s crust) and readily formed (Fe is easily oxidized), and possess little toxicity to humans and the environment. Hematite is the most common form of iron oxide and also the most interesting for PEC applications. With a reported band gap in the range 2.0–2.2 eV, hematite features an absorption onset at wavelengths about 600 nm and therefore exhibits an orange-red color. Importantly, this band gap is of the appropriate magnitude to promise photovoltages sufficient for PEC water splitting, while still absorbing a large fraction of solar photons. Integration of the solar spectrum for a band gap of 2.1 eV yields a theoretical maximum achievable photocurrent of 12 mA/cm².

Detailed discussions about the crystalline, magnetic, and optoelectronic properties along with summaries of historical PEC efforts on hematite can be found in recent literature.²⁰⁻²⁴ Essentially, the material is interesting since it can absorb light across much of the visible spectrum, it is quite stable in water (including alkaline solutions), and it can drive the photo-oxidation of water with high Faradaic efficiency. The key challenges which make it an interesting research subject include:²³

- a) moderately low absorption coefficients at long wavelengths
- b) short minority carrier (hole) diffusion length
- c) low intrinsic majority carrier conductivity
- d) large overpotential for water oxidation
- e) flat band potential too positive for water reduction

Each of these limitations has received significant attention within the last decade. The dilemma of large absorption depths and short hole diffusion lengths has been addressed by fabricating hematite nanostructures aimed at decoupling the directions of light absorption and charge transport.^{15,21,23,25-27} The conductivity can be improved by substitutional doping,²⁷⁻³⁰ and surface catalyst treatments can decrease the water oxidation overpotential.^{25,31-32} These approaches indicate significant progress toward improving hematite's suitability as a water splitting photoelectrode, but none of them address the fundamental limitation that precludes the material from effecting complete water splitting—that the flat band potential (and the conduction band) are too low in energy to yield electrons capable of reducing water. This cannot be solved by any manner of doping, nanostructuring, or catalyst treatments. It is a thermodynamic limitation of the material that requires different approaches. While several ideas have been proposed, including coupling hematite anodes with PV cells,¹⁰ dye-sensitized solar cells,¹³ or photocathodes for additional photovoltage,³³ successful efforts have been rare. Our approaches described in Chapter

6 and Chapter 7 aim to address this deficiency, and have done so by designing unique structures to provide additional photovoltage on a single device.^{14,34}

5.2 Atomic layer deposition of Fe₂O₃ thin films

Our ability to create high-quality thin films of hematite has been a key enabling factor in developing advanced devices. Using the technology of *atomic layer deposition* (ALD), Fe₂O₃ films of well-controlled nanometer-scale thicknesses can be grown on planar substrates or as conformal coatings on high surface area nanostructures.^{14,35} Furthermore, the elemental composition can be tuned to provide dopants to adjust its properties.³⁴

The general principle of ALD is the self-limited surface reaction of elemental precursors to form atomically-thin layers on a substrate. For compounds containing two or more elemental constituents, this is achieved by alternating exposures of the different precursors. In the case of Fe₂O₃, metal-organic complexes of Fe are typically used as the Fe precursor, while H₂O, O₂, or O₃ can serve as the O precursor. Using a procedure adapted from Bachmann et al.,³⁶ we developed an Fe₂O₃ growth recipe employing iron(III) *tert*-butoxide, Fe₂(O^tBu)₆, and H₂O as precursors. Depositions were performed using a Savannah 100 ALD system (Cambridge Nanotech), an instrument which comprises a reaction chamber that is pumped to vacuum, precursor cylinders attached to the chamber via individual high-speed pulse valves, and heating elements for temperature control of all components. The system is equipped an input of high-purity N₂ as carrier gas and a vacuum pump capable of producing base pressures of < 0.4 Torr within the growth chamber (at 20 cm³min⁻¹ carrier gas flow).

In a typical deposition, a cleaned substrate is loaded into the growth chamber, which is subsequently evacuated to about 0.36 Torr and heated to the desired deposition temperature (typically 180 °C). The evacuated precursor cylinder containing the Fe₂(O^tBu)₆ is also heated, to

temperatures in the range 110–150 °C. Lower temperatures risk insufficient precursor vapor pressure for successful pulsing, while temperatures much higher risk thermal decomposition of the precursor. The $\text{Fe}_2(\text{O}^t\text{Bu})_6$ and H_2O are then sequentially pulsed into the chamber where they can react with the substrate surface. A deposition cycle typically consists of a pulse (vacuum valve closed, precursor pulse valve opened), exposure (precursor valve closed), and purge (vacuum valve opened) steps for each precursor. A typical Fe_2O_3 sequence is as follows:

Fe pulse (3 sec), exposure (15 sec), purge (15 sec),

H_2O pulse (0.015 sec), exposure (15 sec), purge (15 sec)

The sequence is repeated to create films of desired thickness. A typical thickness of 20 nm can be produced by 400 ALD cycles, a 0.5 Å/cycle deposition rate. After deposition, we found a thermal treatment at 500 °C (in air or O_2) to be necessary to activate the Fe_2O_3 , improving the crystallinity and resulting in films with good photoactivity. This deposition has been successfully demonstrated on a variety of substrate materials, including Al-doped ZnO, TiSi_2 , F-doped SnO_2 , Sn-doped InO_2 , Si, C nanotubes, and glass.

5.3 Improved photocurrents from Fe_2O_3 on nanostructure scaffolds

The ALD growth of Fe_2O_3 films was first demonstrated by our group on TiSi_2 nanonet arrays.³⁵ These nanostructured substrates, synthesized by chemical vapor deposition (CVD), had previously shown promise with TiO_2 as the active material.³⁷ In the Fe_2O_3 case, the improvement for nanonet-based devices over typical planar devices was significant. Fe_2O_3 - TiSi_2 devices exhibited nearly quadrupled photocurrents, as well as quantum efficiencies (IPCE; internal photon-to-electron conversion efficiency) approaching 50%. This result stands among the highest IPCE values reported and arose from a combination of factors. The nanonets provided a conductive backbone through which electron transport could occur, thereby alleviating Fe_2O_3

from majority carrier transport, for which it was known to have poor conductivities. The vertical arrangements of the nanonets also contributed to improving the Fe₂O₃ absorption characteristics, helping to orthogonalize light absorption and charge transport directions which allowed higher quantum efficiencies. Finally, the nanostructured surface provided a much higher actual surface area per projected area, leading to more active sites and larger photocurrents.

In a similar approach, Fe₂O₃ was deposited onto Al-doped ZnO (AZO) nanotubes, a material known to exhibit transparency along with good conductivity.³⁸ As before, the resulting devices featured enhanced photocurrent and IPCE values. Furthermore, the IPCE in the long-wavelength region near the Fe₂O₃ absorption edge ($500 < \lambda < 600$ nm) showed the greatest enhancement over planar devices, affirming the power of nanostructuring Fe₂O₃ to improve its PEC behavior. These results partially influenced our decision to use nanowire arrays in the study detailed in Chapter 7.

These studies resulted in well-established Fe₂O₃ growth conditions by ALD and demonstrated that the deposition could be applied successfully to a wide variety of substrates. Nonetheless, the approaches still failed to address the key limitation of hematite. The following two chapters describe our attempts to do so.

5.4 References

- 1 Barber, J. Photosynthetic energy conversion: natural and artificial. *Chem. Soc. Rev.* **2009**, *38*, 185-196.
- 2 Tachibana, Y.; Vayssieres, L.; Durrant, J. R. Artificial photosynthesis for solar water-splitting. *Nat. Photon.* **2012**, *6*, 511-518.
- 3 Dubois, M. R.; Dubois, D. L. Development of Molecular Electrocatalysts for CO₂ Reduction and H₂ Production/Oxidation. *Acc. Chem. Res.* **2009**, *42*, 1974-1982.
- 4 Gust, D.; Moore, T. A.; Moore, A. L. Solar Fuels via Artificial Photosynthesis. *Acc. Chem. Res.* **2009**, *42*, 1890-1898.
- 5 Hammarstrom, L.; Hammes-Schiffer, S. Artificial Photosynthesis and Solar Fuels. *Acc. Chem. Res.* **2009**, *42*, 1859-1860.
- 6 Walter, M. G.; Warren, E. L.; McKone, J. R.; Boettcher, S. W.; Mi, Q.; Santori, E. A.; Lewis, N. S. Solar water splitting cells. *Chem. Rev.* **2010**, *110*, 6446-6473.
- 7 Bolton, J. R.; Strickler, S. J.; Connolly, J. S. Limiting and realizable efficiencies of solar photolysis of water. *Nature* **1985**, *316*, 495-500.

- 8 Bolton, J. R. Solar photoproduction of hydrogen: a review. *Solar Energy* **1996**, *57*, 37-50.
- 9 Green, M. A.; Emery, K.; Hishikawa, Y.; Warta, W. Solar cell efficiency tables (version 37). *Prog. Photovolt.* **2011**, *19*, 84-92.
- 10 Brilliet, J.; Cornuz, M.; Formal, F. L.; Yum, J.-H.; Grätzel, M.; Sivula, K. Examining architectures of photoanode–photovoltaic tandem cells for solar water splitting. *J. Mater. Res.* **2010**, *25*, 17-24.
- 11 Khaselev, O.; Bansal, A.; Turner, J. High-efficiency integrated multijunction photovoltaic/electrolysis systems for hydrogen production. *Int. J. Hyd. Energy* **2001**, *26*, 127-132.
- 12 Khaselev, O.; Turner, J. A Monolithic Photovoltaic-Photoelectrochemical Device for Hydrogen Production via Water Splitting. *Science* **1998**, *280*, 425-427.
- 13 Brilliet, J.; Yum, J.-H.; Cornuz, M.; Hisatomi, T.; Solarska, R.; Augustynski, J.; Graetzel, M.; Sivula, K. Highly efficient water splitting by a dual-absorber tandem cell. *Nat. Photon.* **2012**, *6*, 824-828.
- 14 Mayer, M. T.; Du, C.; Wang, D. Hematite/Si Nanowire Dual-Absorber System for Photoelectrochemical Water Splitting at Low Applied Potentials. *J. Am. Chem. Soc.* **2012**, *134*, 12406-12409.
- 15 Lin, Y.; Yuan, G.; Liu, R.; Zhou, S.; Sheehan, S. W.; Wang, D. Semiconductor nanostructure-based photoelectrochemical water splitting: A brief review. *Chem. Phys. Lett.* **2011**, *507*, 209-215.
- 16 Boettcher, S. W.; Spurgeon, J. M.; Putnam, M. C.; Warren, E. L.; Turner-Evans, D. B.; Kelzenberg, M. D.; Maiolo, J. R.; Atwater, H. A.; Lewis, N. S. Energy-conversion properties of vapor-liquid-solid-grown silicon wire-array photocathodes. *Science* **2010**, *327*, 185-7.
- 17 Wang, G.; Ling, Y.; Lu, X.; Wang, H.; Qian, F.; Tong, Y.; Li, Y. Solar driven hydrogen releasing from urea and human urine. *Energy Environ. Sci.* **2012**, *5*, 8215-8219.
- 18 Fujishima, A.; Honda, K. Electrochemical Photolysis of Water at a Semiconductor Electrode. *Nature* **1972**, *238*, 37-38.
- 19 Grätzel, M. Photoelectrochemical cells. *Nature* **2001**, *414*, 338-44.
- 20 Sivula, K.; Le Formal, F.; Grätzel, M. Solar water splitting: progress using hematite (α -Fe₂O₃) photoelectrodes. *ChemSusChem* **2011**, *4*, 432-449.
- 21 Wheeler, D. A.; Wang, G.; Ling, Y.; Li, Y.; Zhang, J. Z. Nanostructured hematite: synthesis, characterization, charge carrier dynamics, and photoelectrochemical properties. *Energy Environ. Sci.* **2012**, *5*, 6682.
- 22 Hamann, T. W. Splitting water with rust: hematite photoelectrochemistry. *Dalton Trans.* **2012**, *41*, 7830-7834.
- 23 Sivula, K. Nanostructured α -Fe₂O₃ Photoanodes. In *Photoelectrochemical Hydrogen Production*; van de Krol, R., Grätzel, M., Eds.; Springer US, 2012; Vol. 102; pp 121-156.
- 24 Lindgren, T.; Vayssieres, L.; Wang, H.; Lindquist, S. E. Photo-oxidation of water at hematite electrodes. In *Chemical Physics of Nanostructured Semiconductors*; Kokorin, A. I., Bahnemann, D. W., Eds.; VSP International Science Publishers: The Netherlands, 2003, doi; pp 83-103.
- 25 Tilley, S. D.; Cornuz, M.; Sivula, K.; Grätzel, M. Light-Induced Water Splitting with Hematite: Improved Nanostructure and Iridium Oxide Catalysis. *Angew. Chem. Int. Ed.* **2010**, *49*, 6405-6408.
- 26 Sivula, K.; Zboril, R.; Le Formal, F.; Robert, R.; Weidenkaff, A.; Tucek, J.; Frydrych, J.; Grätzel, M. Photoelectrochemical water splitting with mesoporous hematite prepared by a solution-based colloidal approach. *J. Am. Chem. Soc.* **2010**, *132*, 7436-44.

- 27 Cesar, I.; Sivula, K.; Kay, A.; Zboril, R.; Grätzel, M. Influence of Feature Size, Film Thickness, and Silicon Doping on the Performance of Nanostructured Hematite Photoanodes for Solar Water Splitting. *J. Phys. Chem. C* **2009**, *113*, 772-782.
- 28 Goodenough, J. B. Metallic oxides. *Prog. Sol. St. Chem.* **1971**, *5*, 145-399.
- 29 Kennedy, J. H. α -Fe₂O₃ Photoanodes Doped with Silicon. *J. Electrochem. Soc.* **1980**, *127*, 2307-2307.
- 30 Liao, P.; Toroker, M. C.; Carter, E. a. Electron transport in pure and doped hematite. *Nano Lett.* **2011**, *11*, 1775-81.
- 31 Zhong, D. K.; Cornuz, M.; Sivula, K.; Graetzel, M.; Gamelin, D. R. Photo-assisted electrodeposition of cobalt-phosphate (Co-Pi) catalyst on hematite photoanodes for solar water oxidation. *Energy Environ. Sci.* **2011**, *4*, 1759-1764.
- 32 Barroso, M.; Cowan, A. J.; Pendlebury, S. R.; Gratzel, M.; Klug, D. R.; Durrant, J. R. The Role of Cobalt Phosphate in Enhancing the Photocatalytic Activity of alpha-Fe₂O₃ toward Water Oxidation. *J. Am. Chem. Soc.* **2011**, *133*, 14868-14871.
- 33 Ingler, W. B.; Khan, S. U. M. A Self-Driven p/n-Fe₂O₃ Tandem Photoelectrochemical Cell for Water Splitting. *Electrochem. Sol. St. Lett.* **2006**, *9*, G144-G146.
- 34 Lin, Y.; Xu, Y.; Mayer, M. T.; Simpson, Z. I.; McMahon, G.; Zhou, S.; Wang, D. Growth of p-type hematite by atomic layer deposition and its utilization for improved solar water splitting. *J. Am. Chem. Soc.* **2012**, *134*, 5508-5511.
- 35 Lin, Y. J.; Zhou, S.; Sheehan, S. W.; Wang, D. W. Nanonet-Based Hematite Heteronanostructures for Efficient Solar Water Splitting. *J. Am. Chem. Soc.* **2011**, *133*, 2398-2401.
- 36 Bachmann, J.; Jing; Knez, M.; Barth, S.; Shen, H.; Mathur, S.; Gösele, U.; Nielsch, K. Ordered Iron Oxide Nanotube Arrays of Controlled Geometry and Tunable Magnetism by Atomic Layer Deposition. *J. Am. Chem. Soc.* **2007**, *129*, 9554-9555.
- 37 Lin, Y.; Zhou, S.; Liu, X.; Sheehan, S.; Wang, D. TiO₂/TiSi₂ heterostructures for high-efficiency photoelectrochemical H₂O splitting. *J. Am. Chem. Soc.* **2009**, *131*, 2772-3.
- 38 Lin, Y. J.; Yuan, G. B.; Sheehan, S.; Zhou, S.; Wang, D. W. Hematite-based solar water splitting: challenges and opportunities. *Energy Environ. Sci.* **2011**, *4*, 4862-4869.

Chapter 6

Creating n–p homojunction Fe₂O₃ for additional photovoltage

This chapter is adapted from: Lin, Y.; Xu, Y.; Mayer, M. T.; Simpson, Z. I.; McMahon, G.; Zhou, S.; Wang, D. Growth of p-type hematite by atomic layer deposition and its utilization for improved solar water splitting. *J. Am. Chem. Soc.* **2012**, *134*, 5508-5511.

As explained previously, there is a fundamental challenge of using hematite for PEC water splitting: the significant mismatch between the band edge positions and the water reduction and oxidation potentials. This mismatch has two important implications. First, with a conduction band edge more positive than the potential at which H₂O is reduced to generate H₂, complete water splitting cannot be achieved without the application of external bias. Second, while the valence band is sufficiently positive to accomplish the oxidation of water, its position is excessively positive which leads to efficiency loss in the form of potential drop. A depiction of these relative energies is shown in Figure 6.1.

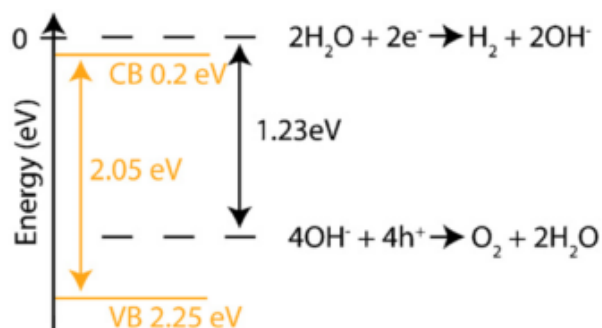


Figure 6.1 Energy diagram showing the potentials for aqueous hydrogen and oxygen evolution reactions, and the relative positions of hematite's conduction band (CB) and valence band (VB) versus the normal hydrogen electrode (NHE). Reprinted from ref ¹, © 2012, with permission from Elsevier.

In principle, the energy mismatch problem can be solved by forming junctions within the semiconductors, thereby enhancing the photovoltage of the cell.²⁻⁵ For instance, Turner et al. achieved high solar water splitting efficiency on GaAs and GaInP₂ junction devices;⁴ Nocera et

al. achieved complete water splitting on devices featuring triple junctions of amorphous Si.⁵ These demonstrations were important but each relied on combinations of expensive or rare materials and demanding synthetic procedures. The ability to apply a similar approach to a low-cost and abundant metal oxide such as Fe₂O₃ would be a significant step toward a practicable water-splitting device.

Energy band diagrams for simple planar systems with and without a junction with the semiconductor are shown in Figure 6.2. Under illumination (as shown), photovoltage (V_{ph}) can be produced as a result of charge separation at either the solid junction or the solid–liquid junction. In a vacuum, where no solid–liquid junction is present and thus no surface band-bending is produced, one would expect a V_{ph} entirely defined by the solid junction (Figure 6.2a). With proper design, it should be possible to create a solid n–p junction capable of producing a built-in V_{ph} that exceeds the voltage possible with a simple solid–liquid junction, thereby improving Fe₂O₃ toward the goal of complete water splitting.

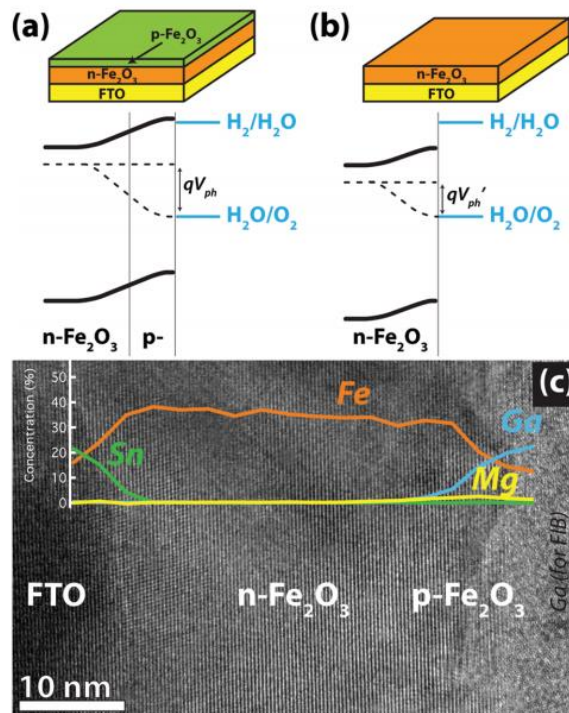


Figure 6.2 Energy band diagrams (under illumination) and microstructures of hematite with a p-type coating. (a) n–p junction hematite produced by surface deposition of a thin Mg-doped layer. (b) Typical intrinsic n-type hematite film. (c) Cross-section TEM image overlaid with elemental composition data from EDS. Reprinted with permission from ref. ⁶, © 2012 American Chemical Society.

P-type hematite has been studied previously,⁷⁻⁸ but the synthesis of high quality n–p junctions in hematite had not been accomplished. We first developed an ALD procedure to grow Mg-doped Fe₂O₃, since ALD would allow us to introduce dopant-level quantities of Mg and to grow the material with high quality interfaces. Using bis(ethylcyclopentadienyl) magnesium as the Mg precursor, inserted into the Fe₂O₃ recipe at a ratio of one Mg pulse per five Fe₂O₃ cycles, films of p-type hematite were grown. The resulting incorporation level was found to be about 3% elemental composition. The Mg incorporation did not introduce changes to the crystal structure, optical absorption, or morphology of the ALD-grown films, but indeed produced the desired p-type characteristics in the material.

A series of experiments confirmed this effect. A *cathodic* photocurrent was observed when measuring Mg-doped hematite in water (Figure 6.3a) which was more pronounced with the addition of an electron scavenger to the solution (H₂O₂). PEC photocurrents are typically dominated by minority carrier transfer to solution, so cathodic (reducing) current corresponds as expected with minority carrier electrons in p-Fe₂O₃. Conversely, normal as-grown hematite shows no cathodic photocurrent response, only anodic (Figure 6.4a, orange). In measurement of the dependence of capacitance on the applied potential, plotted in accordance with the Mott–Schottky relationship (for an n-type semiconductor),

$$\frac{1}{C_{sc}^2} = \frac{2}{e\epsilon\epsilon_0 N} \left(E - E_{FB} - \frac{kT}{e} \right),$$

(C_{sc} is the capacitance of the space-charge region in the semiconductor, e is the electron charge, ϵ is the semiconductor dielectric constant, ϵ_0 the permittivity of free space, N the hole density in the semiconductor, E the applied potential, and E_{FB} the flat band potential)

the expected characteristic negative slope for a p-type semiconductor was observed (Figure 6.3a). Extrapolation of the linear region of the plot to $1/C^2 \rightarrow 0$ yielded an estimated flat band potential of 1.24 V vs. RHE (reversible hydrogen electrode), a potential significantly more positive than that of un-doped hematite (0.67 V vs. RHE).⁹ This represents a considerable shift of the Fe₂O₃ Fermi level toward the valence band edge, further confirming the p-type doping effect.

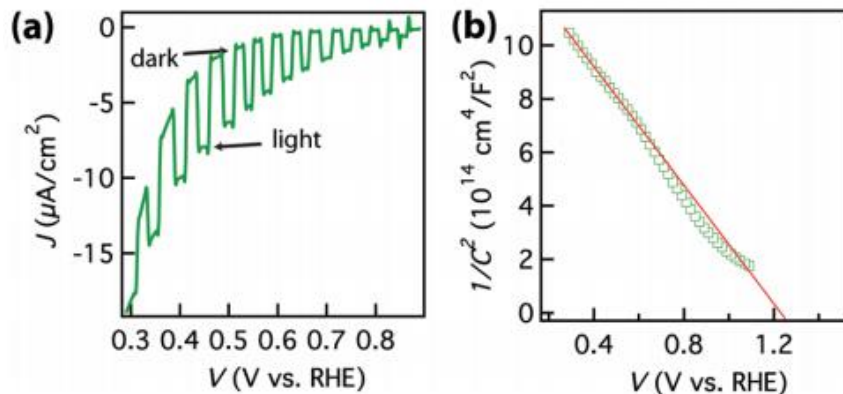


Figure 6.3 Electrochemical characterization of p-Fe₂O₃. (a) Cathodic photocurrent was measured when illuminated in water. (b) Mott-Schottky plot in dark. Reprinted with permission from ref. ⁶, © 2012 American Chemical Society.

We then sought to produce n-p junction devices by simply growing thin films (5 nm) of Mg-doped hematite onto thicker films of un-doped hematite (20 nm), which is inherently n-type due to naturally-occurring oxygen vacancies. Microscopic study showed that the films were polycrystalline in nature and that there was no observable boundary at the n-p junction (Figure 6.2c). Comparison of the PEC performance with and without this p-type layer revealed a significant difference in the potential of photocurrent onset (Figure 6.4a). Whereas un-doped hematite typically exhibits anodic photocurrent only at potentials positive of 1.0 V vs. RHE, the n-p junction devices showed photocurrent at potentials as low as 0.8 V, representing a cathodic shift of 200 mV. The incident photon to charge conversion efficiencies (IPCE) under 1 V applied potential verified the enhanced photoresponse at low bias (Figure 6.4b). This reduced potential for photocurrent onset is significant because it is comparable to what has been achieved through the use of water oxidation catalysts,¹⁰⁻¹¹ but the enhancement comes via an entirely different mechanism.

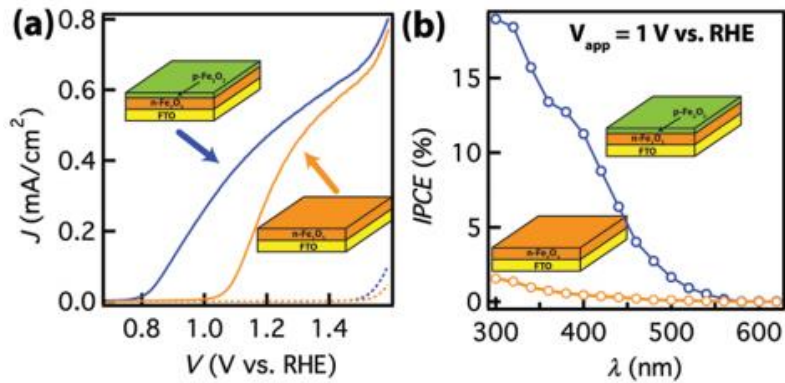


Figure 6.4 PEC characterization of n-Fe₂O₃ with and without p-Fe₂O₃ overlayer. Reprinted with permission from ref. ⁶, © 2012 American Chemical Society.

The concept we demonstrated is that an n–p junction within Fe₂O₃ leads to photocurrent at lower potentials, meaning the device is itself producing a larger photovoltage. To verify the existence of this junction, we used electrochemical impedance spectroscopy (EIS) to probe the expected capacitance of the solid junction. Figure 6.5a shows a Nyquist EIS plot for the two device types. In n-Fe₂O₃, a single semicircle was observed, a feature attributable to the capacitance of the depletion region of the Fe₂O₃ surface as a result of contact with the electrolyte. Contrastingly, two semicircles appeared when the p-Fe₂O₃ overlayer was present, one at the lower frequency range similar to that for n-Fe₂O₃ and a second at higher frequency which we attribute to the n–p junction.

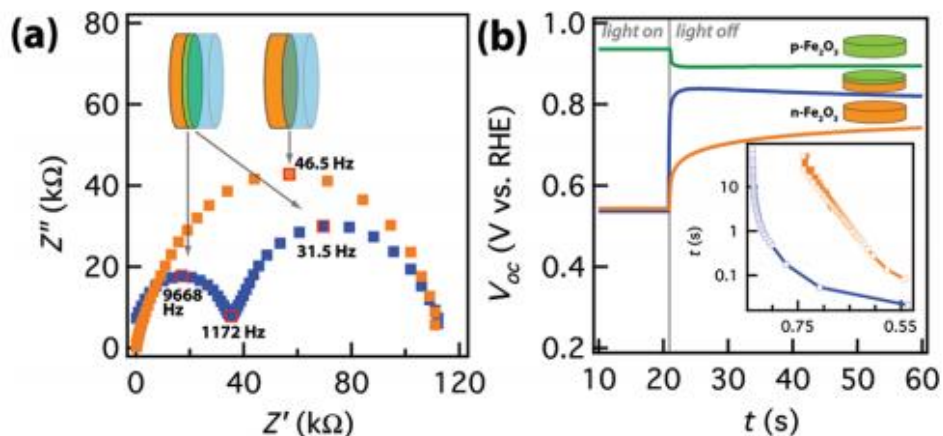


Figure 6.5 Study of the n–p junction within Fe_2O_3 . (a) Nyquist EIS plot of n- Fe_2O_3 (orange) and n–p- Fe_2O_3 (blue). (b) Photovoltage decay measured at open circuit for three device configurations. Reprinted with permission from ref. ⁶, © 2012 American Chemical Society.

Next, the open circuit voltage response to illumination was examined. As expected, p- Fe_2O_3 showed a positive voltage shift under illumination, verifying the p-type behavior (Figure 6.5b, green). Turning our attention to the n- and n–p devices, we see similar photovoltages but different decay behavior upon turning off the illumination. When illuminated, the electric field produced by the n–p junction facilitates charge separation, but also should provide a probable site for photogenerated charges to recombine when illumination is ceased. This concept explains the accelerated decay of V_{oc} for the junction device (Figure 6.5b, blue). The inset of Figure 6.5b replots the data as lifetime vs. potential, which helps to visualize the order-of-magnitude faster decay exhibited by the junction device. Taken together, these electrochemical observations support the claim that a solid n–p junction was formed and that it acts to improve charge separation and produce enhanced photovoltage.

The use of internal fields formed by buried junctions within semiconductors, achieved through doping control, has been a standard approach for the design of electronic devices and solar cells. However, this concept has not been previously demonstrated for metal oxide

semiconductors such as Fe_2O_3 . The main hurdle to this has been the need for great synthetic control, for the development of an internal field requires good spatial and compositional control of the dopant atoms. Defects or inhomogeneities in the junctions can diminish the desired effect. We showed that the ALD technique has the potential to address this problem, using atomic-layer control of dopant incorporation. Junctions within Fe_2O_3 were shown to induce up to a 200 mV cathodic shift in the photocurrent turn-on voltage, representing an improvement toward achieving low- or no-bias water splitting. This approach can undoubtedly work for other metal oxides or desirable materials synthesized by ALD.

6.1 References

- 1 Katz, M. J.; Riha, S. C.; Jeong, N. C.; Martinson, A. B. F.; Farha, O. K.; Hupp, J. T. Toward solar fuels: Water splitting with sunlight and “rust”? *Coord. Chem. Rev.* **2012**, *256*, 2521-2529.
- 2 Boettcher, S. W.; Warren, E. L.; Putnam, M. C.; Santori, E. A.; Turner-Evans, D.; Kelzenberg, M. D.; Walter, M. G.; McKone, J. R.; Brunschwig, B. S.; Atwater, H. A.; Lewis, N. S. Photoelectrochemical hydrogen evolution using Si microwire arrays. *J. Am. Chem. Soc.* **2011**, *133*, 1216-1219.
- 3 Hwang, Y. J.; Boukai, A.; Yang, P. High density n-Si/n-TiO₂ core/shell nanowire arrays with enhanced photoactivity. *Nano Lett.* **2009**, *9*, 410-5.
- 4 Khaselev, O.; Turner, J. A. Monolithic Photovoltaic-Photoelectrochemical Device for Hydrogen Production via Water Splitting. *Science* **1998**, *280*, 425-427.
- 5 Reece, S. Y.; Hamel, J. a.; Sung, K.; Jarvi, T. D.; Esswein, a. J.; Pijpers, J. J. H.; Nocera, D. G. Wireless Solar Water Splitting Using Silicon-Based Semiconductors and Earth-Abundant Catalysts. *Science* **2011**, *645*.
- 6 Lin, Y.; Xu, Y.; Mayer, M. T.; Simpson, Z. I.; McMahon, G.; Zhou, S.; Wang, D. Growth of p-type hematite by atomic layer deposition and its utilization for improved solar water splitting. *J. Am. Chem. Soc.* **2012**, *134*, 5508-5511.
- 7 Leygraf, C.; Hendewerk, M.; Somorjai, G. The preparation and selected properties of Mg-doped p-type iron oxide as a photocathode for the photoelectrolysis of water using visible light. *J. Sol. St. Chem.* **1983**, *48*, 357-367.
- 8 Ingler, W. B.; Baltrus, J. P.; Khan, S. U. M. Photoresponse of p-type zinc-doped iron(III) oxide thin films. *J. Am. Chem. Soc.* **2004**, *126*, 10238-9.
- 9 Lin, Y. J.; Zhou, S.; Sheehan, S. W.; Wang, D. W. Nanonet-Based Hematite Heteronanostructures for Efficient Solar Water Splitting. *J. Am. Chem. Soc.* **2011**, *133*, 2398-2401.
- 10 Tilley, S. D.; Cornuz, M.; Sivula, K.; Grätzel, M. Light-Induced Water Splitting with Hematite: Improved Nanostructure and Iridium Oxide Catalysis. *Angew. Chem. Int. Ed.* **2010**, *49*, 6405-6408.

- 11 Zhong, D. K.; Cornuz, M.; Sivula, K.; Graetzel, M.; Gamelin, D. R. Photo-assisted electrodeposition of cobalt-phosphate (Co-Pi) catalyst on hematite photoanodes for solar water oxidation. *Energy Environ. Sci.* **2011**, *4*, 1759-1764.

Chapter 7

The Si/Fe₂O₃ dual-absorber photoanode

This chapter is adapted from: Mayer, M. T.; Du, C.; Wang, D. Hematite/Si nanowire dual-absorber system for photoelectrochemical water splitting at low applied potentials. *J. Am. Chem. Soc.* **2012**, *134*, 12406.

As introduced in Chapter 5, a semiconductor's photovoltage output is directly dependent on its band gap magnitude. At the same time, an overly-large band gap will limit photon absorption to the short-wavelength region of the solar spectrum. Fe₂O₃ was chosen as a candidate photoanode largely because its band gap of ~2.1 eV presents a good balance between these requirements. However, even with absorption of wavelengths up to 600 nm, hematite devices still waste over half of the solar energy available. This is obvious when comparing the solar spectrum of Figure 1.1 to the hematite IPCE response shown in Figure 6.4.

We therefore wondered whether an approach could be devised which made use of those longer-wavelength photons and translated their energy into additional photovoltage. Tandem approaches where photoanodes are coupled to either dye-sensitized or photovoltaic solar cells have been proposed,¹⁻² but these are difficult to make efficient in stacked configurations since the wavelength responses need to be complimentary and the Fe₂O₃ photoanode device must be prepared such that it is highly transparent to the photons used in the solar cell. Additionally, external wiring components and different electrolyte systems further complicate such designs. By a much simpler approach, we discovered that Fe₂O₃ could be directly deposited onto a smaller-band gap material, Si, which could itself absorb otherwise-wasted photons and contribute to photovoltage enhancement on a single photoelectrode device.³ The resulting device exhibited a photocurrent turn-on potential as low as 0.6 V vs. RHE (Figure 7.1), an improvement even greater than that observed by the n-p junction approach.

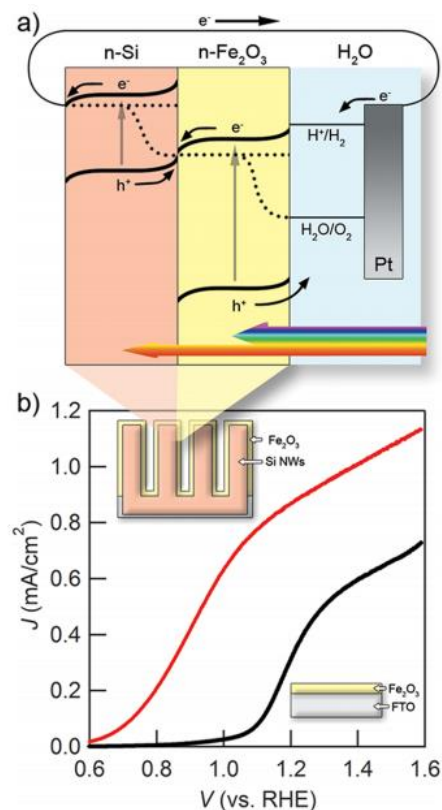


Figure 7.1 (a) Energy band schematic under illumination for the Fe₂O₃/Si NW dual-absorber system. (b) J-V plots under simulated solar illumination for Fe₂O₃/Si NW (red) and Fe₂O₃/FTO (black) devices. Reprinted with permission from ref. ³, © 2012 American Chemical Society.

As illustrated in Figure 7.1a, the key concept is to employ two semiconductors which absorb in complimentary regions of the solar spectrum. Fe₂O₃, which is transparent to photons of wavelength greater than 600 nm, absorbs in the UV and visible region, producing photogenerated holes for water oxidation and electrons for transfer to (normally) the external circuit. The second material, Si, with a band gap of ~1.1 eV, can absorb wavelengths up to 1100 nm, representing a significant portion of photons in the yellow-red-infrared region. It, too, produces photogenerated electrons and holes upon absorption. Interestingly, and rather unique to this system, is that because of the closeness in energies of the Fe₂O₃ conduction band and the Si valence band, charge transfer occurs between them in what is essentially an electron-hole recombination event

at the heterojunction. The overall effect is that Si leads to a further increased potential of the electron transferred to the external circuit, which represents an enhanced photovoltage and thereby decreases the demand for applied bias.

Figure 7.1b compares the performance of an Fe₂O₃-coated Si nanowire (NW) array sample to a typical Fe₂O₃ planar film device on a transparent conductive substrate (F-doped SnO₂, FTO). In both cases, approximately 20 nm of Fe₂O₃ was deposited by ALD onto the desired substrate. For Si, we used chemically-etched NW arrays.⁴ As expected, when Si is present the potential of the photocurrent onset is significantly shifted in the cathodic direction. With an onset of about 0.6 V vs. RHE, the Fe₂O₃/Si represents one of the lowest turn-on potentials yet seen for a single Fe₂O₃-based photoelectrode. Also, the photocurrent was significantly higher than the planar device, likely a result of the improved light absorption characteristics on vertically-aligned nanowires, as well as the overall increased active surface area.

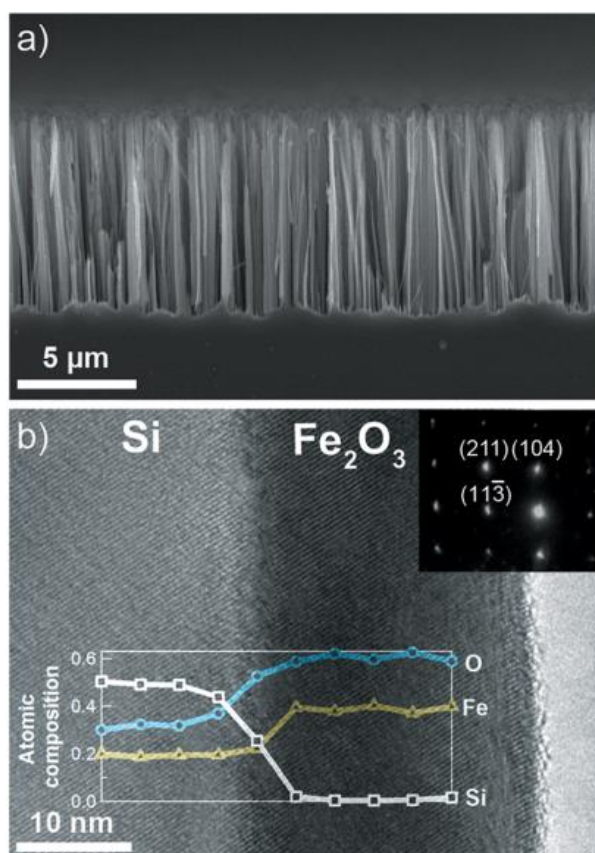


Figure 7.2 Microstructure of Fe₂O₃/Si photoelectrodes. (a) SEM image showing the vertical arrangement of chemically-etched Si NWs. (b) TEM image showing the crystalline quality of Fe₂O₃ grown on Si by ALD. Insets: electron diffraction pattern (top right) and EDS spatial elemental composition (overlaid). Reprinted with permission from ref. ³, © 2012 American Chemical Society.

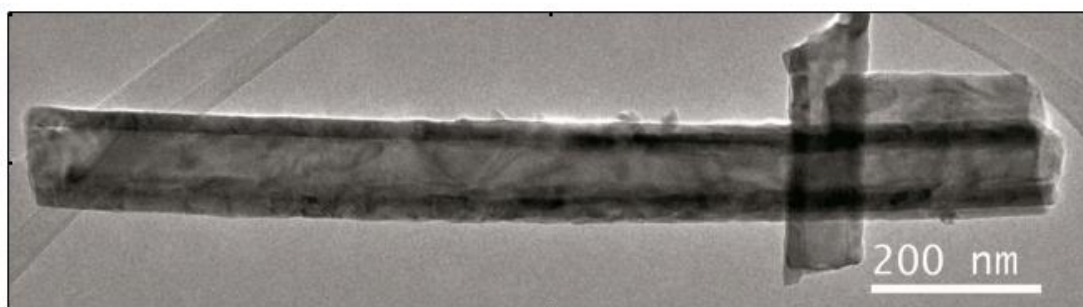


Figure 7.3 Low-magnification TEM of a typical Fe₂O₃-coated Si NW.

The quality of the deposited Fe₂O₃ on Si was confirmed by microscopy and diffraction studies (Figure 7.2, Figure 7.3). Although n-type doping by Si has been previously demonstrated

as a way to enhance the conductivity of hematite,⁵ we detected no appreciable Si concentration in the hematite layer of our heterojunction devices, suggesting that negligible interfacial diffusion took place during the mild post-deposition annealing treatment (500 °C). Importantly, a sustained photocurrent without decay was measured for up to 3 hours of photoanodic current (Figure 7.4), confirming the device stability and ruling out the possibility that the anodic current was due to the oxidation of Si.

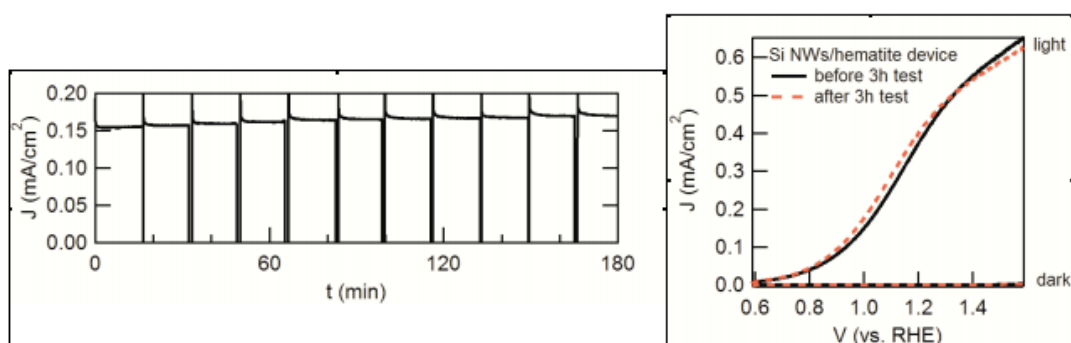


Figure 7.4 Long-duration $\text{Fe}_2\text{O}_3/\text{Si}$ NW photoanode testing. Left: Anodic current levels over 3 h of 1.0 V_{RHE} applied bias. Every ~15 min the illumination was blocked for a moment to examine the dark currents, which remained near zero for the duration of the test. Right: J-V curves in light and dark both before (black lines) and after (red dotted lines) the 3 h test.

In this type of dual-absorber system in which two photons must be absorbed for every one electron provided to the external circuit, the overall photocurrent is limited by the lowest-performing component, which in the present case is likely to be the hematite. Therefore, the performance is sensitive to the light absorption in hematite, which explains the lower currents observed on similar devices prepared on planar Si substrates (Figure 7.8a). Nonetheless, the important feature, the low onset potential, is largely preserved in the planar geometry, supporting the proposed dual-absorber mechanism.

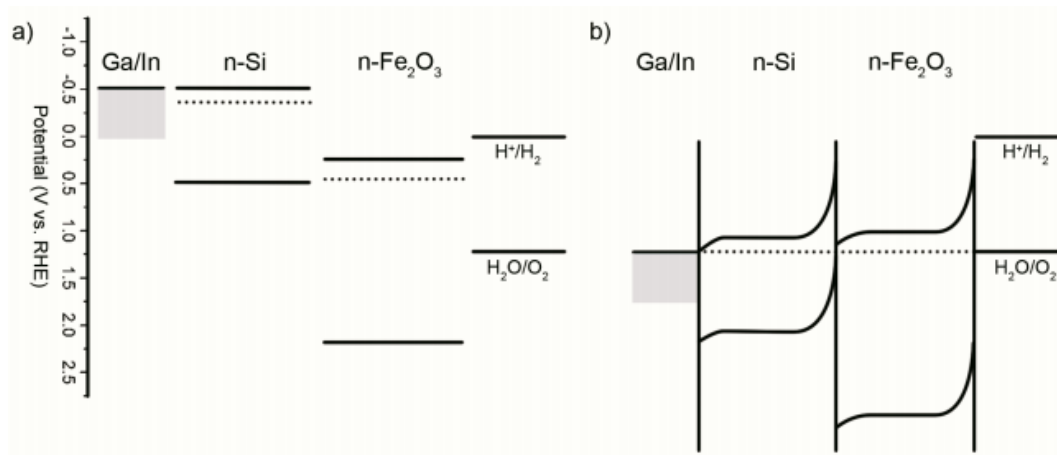


Figure 7.5 Energy band diagrams for the Fe₂O₃/Si system. (a) Intrinsic energy levels of each component before contact equilibrium, determined theoretically⁶ and experimentally.⁷⁻⁸ (b) Equilibrium in dark, assuming equilibration to the H₂O/O₂ couple in solution and pinned band edges at each interface. Ga/In is used to make ohmic contact to n-type Si.

In examining the sample variation, we found that Fe₂O₃/Si NW devices routinely gave onset potentials around 0.6 V vs. RHE, while Fe₂O₃/FTO typically gave onsets of about 1.0 V. There were sample-to-sample variations in curve shape and peak photocurrent magnitude, but it should be noted that the Fe₂O₃/Si NW devices exhibited a lesser degree of variation than the FTO-based ones (Figure 7.6a).

The proposed band schematics of Figure 7.1a (also shown for pre-equilibrium and dark conditions in Figure 7.5) predict that the magnitude of the cathodic shift should correspond with the amount of photovoltage produced by the Si NWs. In turn, this is dependent on the amount of band bending in the Si as a result of equilibration between Si and Fe₂O₃. We tested this prediction by varying the Si doping level or doping type. When the Fermi level of Si is made to be closer to the Si valence band edge (such as for p-type Si), the offset in flat-band potential between Si and Fe₂O₃ is smaller and a smaller photovoltage would be expected to result. This was confirmed as shown in Figure 7.6b (pink line), where the p-Si substrate gives the poorest onset potential. However, an appreciable band-bending depth is necessary for effective charge separation in Si,

and since highly-doped Si can support only narrow depletion regions,⁶ it is not the highest n-doped Si which gave the best onsets. In an apparent balance between depletion depth and flat-band potential offset, it was the rather low-doped n-Si which gave the best onset potentials, as shown in red in Figure 7.6 and in the original Figure 7.1.

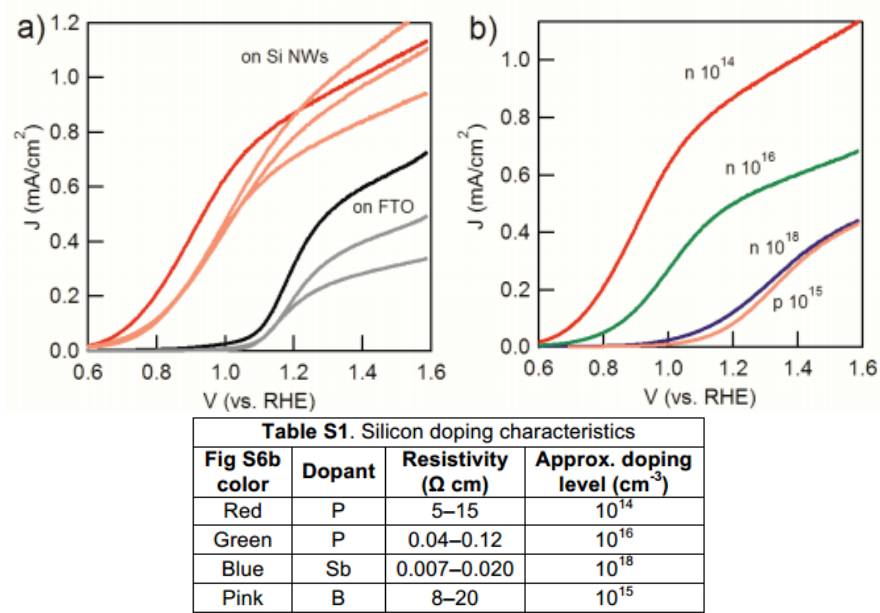


Figure 7.6 (a) Representative J-V plots for replicate $\text{Fe}_2\text{O}_3/\text{Si}$ NW and $\text{Fe}_2\text{O}_3/\text{FTO}$ devices. Variation between samples was observed, but was less pronounced on the $\text{Fe}_2\text{O}_3/\text{Si}$ devices. (b) $\text{Fe}_2\text{O}_3/\text{Si}$ NW devices employing Si of different doping characteristics (details in table).

For the dual-absorber system to function properly, the two photon absorption processes must take place simultaneously. To demonstrate this, we devised a set of experiments proving the dual-absorber nature using monochromatic light for excitation. First, short-wavelength photons ($\lambda = 365$ nm) from a UV lamp were used to illuminate the $\text{Fe}_2\text{O}_3/\text{Si}$ NW device at relatively low power (3 mW cm^{-2}). These photons have sufficient energy to excite hematite and are at of a wavelength at which hematite absorbs strongly (Figure 6.4), so most of them can be expected to be absorbed within the hematite layer. The resulting J-V curve and representative band diagram, shown in Figure 7.7a, show behavior expected when Fe_2O_3 alone is excited. Photogenerated holes can

transfer to solution as normal, but photogenerated electrons encounter a barrier at the Si interface which likely inhibits their passage. The appearance of photocurrent above potentials of about 1.0 V vs. RHE signifies that those electrons can ultimately be collected, likely due to tunneling through the barrier as enabled by the thinning of the barrier width in response to anodic bias. Notably, the onset potential resembles that of a Fe₂O₃-only device (Fe₂O₃/FTO, Figure 7.1b).

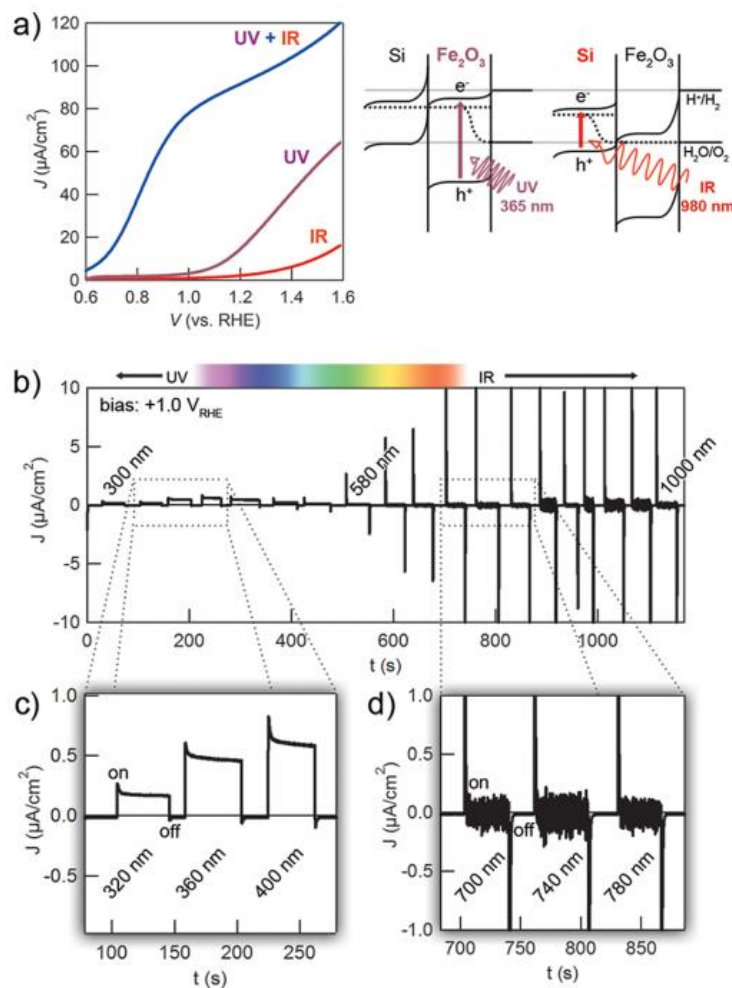


Figure 7.7 (a) J-V curves for a typical Fe₂O₃/Si NW electrode under different and combined monochromatic illumination, and representative illuminated band energy diagrams (right). (b) Spectral photocurrent response to monochromatic light of wavelength 300–1000 nm while biased at +1.0 V_{RHE}. (c) and (d) are magnified views of regions in (b). Reprinted with permission from ref. ³, © 2012 American Chemical Society.

In contrast, when a low-energy light source (IR laser, $\lambda = 980$ nm) was used as the illumination source, the photons should pass through the larger-band gap Fe_2O_3 to be solely absorbed by Si. Despite using a laser with relatively high power (2000 mW cm^{-2}), no significant photocurrent was observed until large anodic bias was applied (Figure 7.7a, red). This occurred because photoexcited holes in the Si encounter a large barrier to entering the Fe_2O_3 valence band and the Fe_2O_3 is too thick to allow tunneling. Therefore, anodic currents cannot be produced unless a large supplemental voltage is applied.

Finally, upon combining the two sources for simultaneous illumination of $\text{Fe}_2\text{O}_3/\text{Si}$, the full development of the photovoltage was realized. As shown in the J-V curve (Figure 7.7a, blue), the combination illumination produced a curve shape similar to that observed from full-spectrum illumination (Figure 7.1b), although featuring a smaller plateau photocurrent resulting from the bottleneck of low-power UV illumination. Under dual excitation, the proposed band diagram of Figure 7.1a is realized, with photogenerated charges in both materials and a favorable recombination at the heterojunction. In a synergistic effect, the dual illumination J-V curve yields photocurrent levels much greater than simply the sum of the UV- and IR-illumination curves. In contrast, the $\text{Fe}_2\text{O}_3/\text{FTO}$ device responded only to UV light, as expected for a single larger-band gap absorber (Figure 7.8c). The dual-absorber finding contrasts this result from studies in which Si is claimed as the lone active photoanode material, with Fe_2O_3 serving in a passivating⁹ or catalytic¹⁰ role.

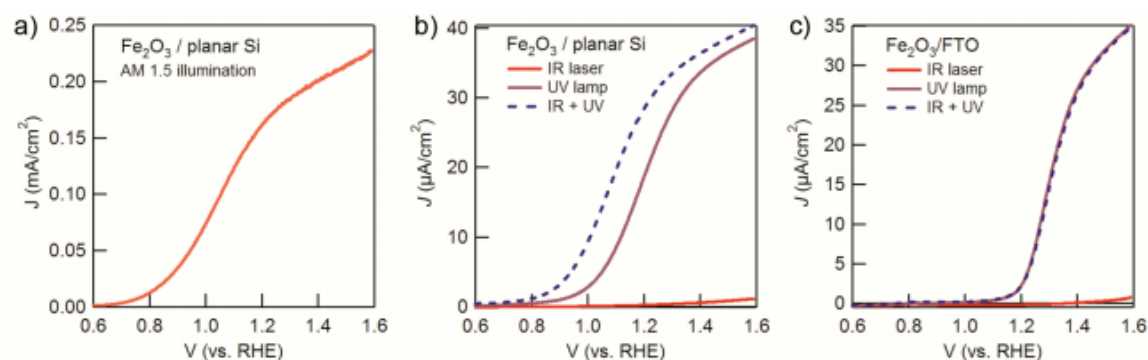


Figure 7.8 Fe₂O₃ device variations. (a) Fe₂O₃ on planar Si (100) substrate. (b) Fe₂O₃/planar Si device under monochromatic illumination. (c) Fe₂O₃/FTO device under monochromatic illumination.

As further evidence of the response to photon energy variation, we measured the wavelength-dependent photocurrent using monochromatic light ranging from $300 \text{ nm} < \lambda < 1000 \text{ nm}$. The illumination was achieved by passing simulated solar light through a monochromator. The photocurrent response (Figure 7.7) reaffirmed the behavior expected from the previous monochromatic analysis. In the short- λ range (300–580 nm) where the primary absorber is hematite, appreciable anodic photocurrent was observed. Since the photocurrent was nonzero, the photoexcited electrons from the hematite conduction band can be injected into Si to produce a stable photocurrent at this potential. In contrast, no total current flow was observed in the long- λ region (580–1000 nm). Notably different from the behavior under short- λ illumination was the apparent noise level, which in the long- λ region was significantly higher. We believe that this “noisy” current is due to the random collection of photogenerated electrons and holes by the external circuit, both from Si. This occurs because hole transfer through hematite into water is forbidden and thus photogeneration and recombination are balanced and yield a noisy baseline current.

A notable feature was the obvious transient phenomenon that appeared in the form of current spikes when the light was alternated between on and off. To explain the nature of these transient

spikes, consider that the anodic photocurrent of an electrode is a measure of how fast *electrons* are collected. An anodic spike in the current–time plot thus indicates a surge of electrons which has previously been explained by the charging and discharging effect of trap states.¹¹⁻¹² For the Fe₂O₃/Si NW system, these transient spikes could originate from trap states originating either at the hematite–electrolyte interface¹³ at the hematite–Si interface. A control experiment on hematite/FTO under similar conditions (Figure 7.9) helped us conclude that while the transient behaviors under UV and blue illumination may be explained by the nature of the hematite–electrolyte junction, the transients appearing in the red and near-IR region can only be explained by charging and discharging of the hematite–Si interface. That is, when the light is switched on, rapid charge separation takes place within the Si, electrons being collected to produce an anodic photocurrent and holes moving to the Si–hematite interface where they accumulate at the barrier. When these trapped holes recombine with photogenerated electrons in the hematite conduction band, which takes place under dual-illumination conditions as in Figure 7.1, a steady-state photocurrent is measured. In the absence of effective excitation within hematite, however, the initial photocurrent due to charges within Si quickly decays to zero net current, resulting in a transient spike. When the light is switched off, relaxation (recombination) of the initially trapped holes requires electron back-transfer into Si, leading to the cathodic photocurrent spike. These features can be clearly observed in Figure 7.7d.

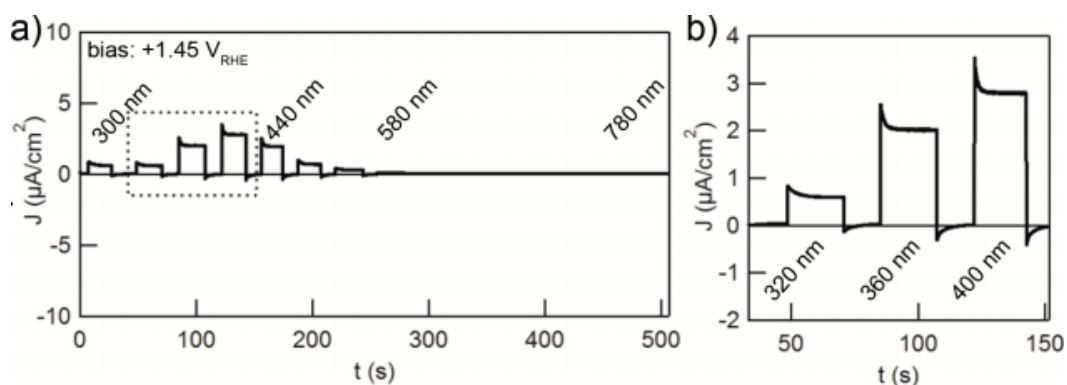


Figure 7.9 Spectral photocurrent response of Fe₂O₃/FTO device, showing (a) activity only for wavelengths up to ~600 nm, and (b) detail showing the transient photocurrent behavior and photocurrent magnitude.

A detailed and quantitative understanding of these behaviors, such as from impedance-based electrochemical methods, will require more effort but should yield useful information. Furthermore, since a dual-absorber device relies on balancing of charge generation rates to operate at maximum efficiency, there is plenty of room to optimize the Fe₂O₃/Si system. The Si geometry and the Fe₂O₃ thickness, when properly designed, may produce photocurrents significantly higher than what we have reported. Furthermore, this approach should be compatible with the other efforts to enhance hematite, including doping for conductivity enhancement and application of water oxidation catalysts.

In conclusion, we demonstrated that high-quality hematite deposited on Si NWs can yield a dual-absorber device producing photovoltages in excess of those possible on Fe₂O₃-only devices. Charge flow is enabled only by simultaneous excitation of both absorbers and takes place by means of a favorable recombination process at the Fe₂O₃-Si junction. The result is a significant cathodic shift of the photocurrent onset potential to near-record values for Fe₂O₃-based devices, achieved without the use of catalysts, surface treatments, or hematite doping. The dual-absorber approach takes inspiration from natural photosynthesis, wherein two photon absorption processes act to promote electrons to greater reduction potentials. A significantly broadened spectrum of

response is a result of using semiconductors with complimentary absorption characteristics, allowing both high- and low-energy photons to contribute to the photovoltage.

These results provide a promising direction for improving hematite by directly coupling it with small-band-gap materials to realize greater photovoltages on a single device. The device preparation depends on the growth of high-quality films made possible by the ALD technique. Notably, the fact that the active materials are composed of three of the four most abundant elements in Earth's crust (O, Si, and Fe) offers promise that widespread solar energy harvesting by PEC water splitting remains an achievable goal.

7.1 References

- 1 Brillet, J.; Cornuz, M.; Formal, F. L.; Yum, J.-H.; Grätzel, M.; Sivula, K. Examining architectures of photoanode–photovoltaic tandem cells for solar water splitting. *J. Mater. Res.* **2010**, *25*, 17-24.
- 2 Brillet, J.; Yum, J.-H.; Cornuz, M.; Hisatomi, T.; Solarska, R.; Augustynski, J.; Graetzel, M.; Sivula, K. Highly efficient water splitting by a dual-absorber tandem cell. *Nat. Photon.* **2012**, *6*, 824-828.
- 3 Mayer, M. T.; Du, C.; Wang, D. Hematite/Si Nanowire Dual-Absorber System for Photoelectrochemical Water Splitting at Low Applied Potentials. *J. Am. Chem. Soc.* **2012**, *134*, 12406-12409.
- 4 Yuan, G.; Zhao, H.; Liu, X.; Hasanali, Z. S.; Zou, Y.; Levine, A.; Wang, D. Synthesis and Photoelectrochemical Study of Vertically Aligned Silicon Nanowire Arrays. *Angew. Chem. Int. Ed.* **2009**, *48*, 9680-9684.
- 5 Cesar, I.; Sivula, K.; Kay, A.; Zboril, R.; Grätzel, M. Influence of Feature Size, Film Thickness, and Silicon Doping on the Performance of Nanostructured Hematite Photoanodes for Solar Water Splitting. *J. Phys. Chem. C* **2009**, *113*, 772-782.
- 6 Sze, S. M.; Ng, K. K.: *Physics of Semiconductor Devices*; Third ed.; John Wiley & Sons: Hoboken, NJ, 2007.
- 7 Weber, M. F.; Dignam, M. J. Efficiency of splitting water with semiconducting photoelectrodes. *J. Electrochem. Soc.* **1984**, *131*, 1258-1265.
- 8 Hwang, Y. J.; Boukai, A.; Yang, P. High density n-Si/n-TiO₂ core/shell nanowire arrays with enhanced photoactivity. *Nano Lett.* **2009**, *9*, 410-5.
- 9 Morisaki, H.; Ono, H.; Dohkoshi, H.; Yazawa, K. Iron-Oxide Coated n-Si as a Heterostructure Photoanode for the Photoelectrolysis of Water. *Jap. J. Appl. Phys.* **1980**, *19*, L148-L150.
- 10 Jun, K.; Lee, Y. S.; Buonassisi, T.; Jacobson, J. M. High photocurrent in silicon photoanodes catalyzed by iron oxide thin films for water oxidation. *Angew Chem Int Ed* **2012**, *51*, 423-7.

- 11 Duffy, N. W.; Peter, L. M.; Rajapakse, R. M. G.; Wijayantha, K. G. U. A novel charge extraction method for the study of electron transport and interfacial transfer in dye sensitised nanocrystalline solar cells. *Electrochem. Comm.* **2000**, *2*, 658-662.
- 12 Jennings, J. R.; Ghicov, A.; Peter, L. M.; Schmuki, P.; Walker, A. B. Dye-sensitized solar cells based on oriented TiO₂ nanotube arrays: Transport, trapping, and transfer of electrons. *J. Am. Chem. Soc.* **2008**, *130*, 13364-13372.
- 13 Klahr, B.; Gimenez, S.; Fabregat-Santiago, F.; Bisquert, J.; Hamann, T. W. Photoelectrochemical and Impedance Spectroscopic Investigation of Water Oxidation with “Co–Pi”-Coated Hematite Electrodes. *J. Am. Chem. Soc.* **2012**, *134*, 16693-16700.

Chapter 8

Outlook for PEC water splitting

In the previous chapters two different approaches to enhancing the PEC performance of Fe_2O_3 -based photoanodes were described. The first took inspiration from traditional p–n junction solar cells and applied the homo-junction concept to a metal oxide semiconductor. The second took inspiration from natural photosynthesis, using a two-photon process to generate larger photovoltage and enhanced driving force for chemical reactions. Both approaches represent progress toward addressing the challenges of energetic limitations of Fe_2O_3 for splitting water.

The beauty of these types of PEC photoelectrodes is that it should be theoretically possible to combine a variety of approaches, including those discussed above as well as others introduced at the start of the chapter, for further enhanced performance. For instance, it is conceivable that an n–p junction Fe_2O_3 layer could be deposited onto Si nanowire arrays to realize an even greater overall photovoltage. Furthermore, doping of Fe_2O_3 , surface catalyst treatments, and even nano-patterning for optimized light absorption could be appended in an approach aimed at tackling each of hematite's limitations simultaneously. The challenge lies in developing them all to be compatible with each other as well as preserving cheap and simple methods of preparation while using abundant elements.

At this relatively early stage, however, it remains important to continue to devise new approaches and study them individually. Our approaches at photovoltage enhancement can hopefully inspire future research efforts aimed at tackling the energetic shortcomings of photoactive materials for PEC applications. Our further efforts will be focused on taking advantage of our specialty of growing high-quality and conformal films of materials, by ALD in particular, to address some of the other challenges, including passivating the Fe_2O_3 surface

against unfavorable side-reactions or depositing films of water-reduction catalyst to improve the photoanode activity.